Cryogenic Scanning Laser Microscopy: Investigation of large BSCCO mesas and development of a polarizing microscope

Dissertation
der Mathematisch-Naturwissenschaftlichen Fakultät
der Eberhard Karls Universität Tübingen
zur Erlangung des Grades eines
Doktors der Naturwissenschaften
(Dr. rer. nat.)

vorgelegt von
Stefan Alexander Guénon
aus Reutlingen

Tübingen
2011

Tag der mündlichen Qualifikation:	20. Juli 2011
Dekan:	Prof. Dr. Wolfgang Rosenstiel
1. Berichterstatter:	Prof. Dr. Reinhold Kleiner
2. Berichterstatter:	Prof. Dr. Dieter Kölle
3. Berichterstatter:	Prof. Dr. Paul Müller

Contents

Zusammenfassung

Diese Arbeit besteht aus zwei Teilen.
Teil 1, "Large BSCCO Mesas: A Low-Temperature Scanning Laser Microscopy Study":
Im Jahre 2007 konnten L. Ozyuzer und seine Kollegen zum ersten Mal die Emission von kohärenter Terahertz-Strahlung aus $Bi_2Sr_2CaCu_2O_8$-Einkristallen nachweisen [69]. Die Emitter waren Mesas, die Stapel aus intrinsischen Josephson-Kontakten bilden, mit beträchtlichen lateralen Abmessungen (ca. $300\,\mu\text{m} \times 50 - 100\,\mu\text{m}$) und einer Höhe von ungefähr $1\,\mu$m.
Unter Verwendung der Tieftemperatur-Raster-Laser-Mikroskopie (TTRLM) wurden im Rahmen dieser wissenschaftlichen Arbeit ähnliche Proben untersucht.
Bei der TTRLM erzeugt ein auf einen Punkt (x,y) in der Probenoberfläche fokussierter Laserstrahl eine lokalisierte Erwärmung. Gleichzeitig wird die Spannungsantwort der Probe auf einen konstanten Strom mit Hilfe einer Vier- oder Zweipunktmessung überwacht. Die Amplitudenmodulation des Laserstrahls hat zur Folge, dass die Temperatur der lokalisierten Erwärmung ebenfalls moduliert wird. Dies führt zu einer von der Lasersondenposition abhängigen Spannungsantwort $\Delta V(x, y)$, die mit Hilfe von Lock-in-Technik ausgelesen werden kann. Durch Rastern der Lasersonde über die Probe und Aufzeichnen der Spannungsantwort $\Delta V(x, y)$ lassen sich so genannte Spannungsbilder aufnehmen. Abhängig von der untersuchten Probe können diese Spannungsbilder verschiedenste, physikalische Eigenschaften abbilden.
Es wurden zwei wissenschaftliche Zielsetzungen verfolgt: Erstens sollten die Plasmawellen, die die THz-Strahlung erzeugen, mittels TTRLM abgebildet werden, und zweitens sollte der Selbstheizeffekt, von dem man ausgehen kann, dass er in Stapeln dieser Größe beträchtlich ist, untersucht werden.
Tatsächlich war es möglich in einer Probe Stehwellenmuster abzubilden, wenn diese an elektrischen Arbeitspunkten mit schwach aufgeprägtem

Strom betrieben wurde, die genau in dem Arbeitsbereich lagen, in dem L. Ozyuzer THz-Strahlung detektiert hatte. Wird ein stärkerer Strom aufgeprägt, so biegt die Strom-Spannungs-Kurve auf Grund des Selbstheizeffektes nach oben ab verläuft dann fast senkrecht. In diesem Arbeitsbereich zeigte sich in den TTRLM-Spannungsbildern ein Muster, das eindeutig als elektro-thermische Domäne (Hot Spot) identifiziert werden konnte. Neben diesem Hot Spot waren in bestimmten Stromintervallen Stehwellenmuster zu sehen. Um die Frage zu klären, ob diese Stehwellenmuster mit THz-Strahlung korrelieren, wurde ein Interferometer mit einem Bolometer als Detektor realisiert. Auf diese Weise war es möglich THz-Strahlung im besagten elektrischen Arbeitsbereich (hot spot bias regime) nachzuweisen und ihre Frequenz zu bestimmen. Desweiteren wurde für unterschiedliche Basistemperaturen bestätigt, dass die Frequenz der emittierten Strahlung und die angelegte Spannung durch die Josephson Relation bestimmt sind.
Teil 2, "A Cryogenic Scanning Polarizing Microscope for Magneto-Optical Imaging":
Ursprünglich sollte das vorhandene Tieftemperatur-Raster-Laser-Mikroskop um die Möglichkeit zur Polarisationsmikroskopie erweitert werden. Die Idee war, TTRLM-Spannungsbilder mit magneto-optischen Bildern zu kombinieren. Aber es stellte sich bald heraus, dass ein komplett neuer Versuchsaufbau erforderlich ist.
Ein Raster-Polarisationsmikroskop hat eindeutige Vorteile gegenüber einem konventionellen Polarisationsmikroskop: Es können ohne großen Aufwand hohe Beleuchtungsintensitäten erreicht werden, die Auflösung verbessert sich durch das konfokale Design um den Faktor 1.4 und die serielle Signalverarbeitung erleichtert die Verbesserung des Signal-Rausch-Verhältnis. Desweiteren ist es für gewöhnlich nicht notwendig, die Bilder mit einem Differenzbildverfahren nachzubearbeiten, um den Kontrast nichtmagnetischen Ursprungs zu entfernen. In dieser Arbeit wurde ein Tieftemperatur-Raster-Polarisationsmikroskop entwickelt und implementiert. Tests und erste Ergebnisse werden vorgestellt und es wird ein Ausblick gegeben, wie dieses Projekt fortgesetzt werden kann.

Abstract

This thesis is divided into two parts. Concerning the first part:
Motivated by the discovery of coherent Terahertz emission from large sized $Bi_2Sr_2CaCu_2O_8$ stacks of intrinsic Josephson Junctions by Ozyuzer et al. [69], low-temperature laser scanning microscopy (LTSLM) was used to investigate similar samples.
In LTSLM a focused laser beam at position (x,y) is heating the sample in its vicinity. Simultaneously the electrical resistance of the sample is monitored by 4- or 2-wire sensing. By blanking the laser beam and using lock-in technique the response, i.e., the beam induced voltage change $\Delta V(x, y)$ to the heat distribution at the location (x,y) can be detected. Scanning the laser beam and mapping the response $\Delta V(x, y)$ leads to the so-called voltage image of the sample. Depending on the sample under investigation this voltage image is a map of all kinds of physical properties. This experimental technique was used with two objectives. First, the plasma wave causing the THz emission should be imaged, and second, the phenomenon of self-heating, which is considerable for large mesas, should be investigated. Indeed, it was possible to map a standing wave pattern at bias points with low currents, where Ozyuzer et al. have detected THz radiation. At high currents, where the back bending in the current-voltage relation indicates strong self heating, a feature appears in the LTSLM voltage images, which was clearly identified as an electro-thermal domain (hot spot) created by the temperature dependence of the c-axis resistivity in the $Bi_2Sr_2CaCu_2O_8$ -mesa. In this bias interval a standing wave pattern appears beside this feature at certain bias points. In order to investigate wether this standing wave pattern is associated with THz emission, a simple interferometer with a bolometer as detector was realized. With the help of this set-up it was possible to detect THz radiation from mesas at high bias currents (hot spot bias regime) and to determine its frequency. It could be confirmed that the frequency of the emitted radiation and the bias voltage is determined by the Josephson relation for a wide range of different base temperatures. This way other mechanisms, causing THz

radiation, rather than the Josephson effect can be excluded.
Concerning the second part:
Originally it was planned to extend the low-temperature scanning laser microscope with the facility of polarizing microscopy. The idea was to combine the LTSLM voltage imaging with the possibility of magnto-optical imaging. But it soon turned out that a new design would be necessary. A laser scanning polarizing microscope has certain advantages in comparison with a conventional polarizing microscope: Very high illumination intensities can be reached easily, the resolution can be improved by the factor 1.4 if a confocal optical design is used, and the serial signal processing facilitates the optimization of the signal-to-noise ratio. In addition, it is usually not necessary to remove the contrast of non-magnetic origin by subtracting an image of the uniform magnetized sample from the image of interest. In this thesis a design for a cryogenic scanning polarizing microscope (CSPM) is discussed in detail, tests and first results of the system are presented, and an outlook is given how two proceed with this project.

Part I.

Large BSCCO Mesas: A Low-Temperature Scanning Laser Microscopy Study

1. Introduction

Electromagnetic radiation with a frequency between 300 GHz and 30 THz is typically referred to as THz radiation. There is a growing demand for THz sources in a variety of areas of research and technology (e.g. biological and medical science, non-destructive evaluation, homeland security, and quality control of food and agricultural products). Although progress has been made, solid-state devices emitting in a frequency range of 0.5 THz to approximately 1.5 THz are still missing [99]. This so-called THz gap has two reasons: First, the thermal activation prevents population inversion in semiconductor lasers with small band-gaps. Therefore, conventional semiconductor lasers cannot operate at a frequency below 2 THz. Second, the charge-carrier mobility restrics the emitting frequency of semiconducting devices to below approximately 500 GHz.

Electronic devices based on superconductors might be a solution. According to the Josephson relation, a Josephson Junction (JJ) is an ideal voltage-to-frequency converter. Therefore, the idea of using a JJ as a source for coherent electromagnetic radiation is straight forward. Unfortunately, the output power of single Josephson Junction is very small, typically in the pW range.

One way to overcome this shortcoming is to design devices consisting of multiple junctions. Usually, the oscillations in the individual junctions of such a device would be incoherent due to the spread in junction parameter and fluctuations. Hence, a coupling mechanism is needed that enforces coherent, or in other words, phase-locked oscillations. The most prominent coupling mechanism is the high-frequency electromagnetic coupling: By embedding the JJs in microstriplines or coplanar striplines, the Josephson oscillations in the individual junctions are phase-locked via the alternating current transmitted by the striplines. Using 1D arrays of JJs in a microstripline, it was possible to deliver a power of 160 μW at 240 GHz [8] or even 400 μW at 410 GHz to a load on the same chip [48].

Because the quasiparticle current causes significant damping, an emitter based on the Josephson effect can only operate efficiently at frequencies

that correspond to voltages below the gap voltage. For instance, the operation frequency of a JJ-emitter based on the low T_c superconductor Niobium cannot exceed $\sim 750\,\mathrm{GHz}$. In principal, higher frequencies (theoretically up to 12 THz) can be achieved using high T_c superconductors, which have a larger superconducting gap voltage. Unfortunately, the fabrication of high-quality JJs in high T_c superconductors is very challenging.

In the high-temperature superconductor $Bi_2Sr_2CaCu_2O_8$ (BSCCO), the order parameter in the CuO_2 layers is weakly coupled in the c-direction and a single crystal made of BSCCO forms naturally a stack of coupled intrinsic Josephson Junctions (IJJs) [51]. This way, the obstacle of fabricating high-quality junctions in high T_c superconductors can be overcome. Many attempts have been made to utilize BSCCO as an emitter, but it turned out that phase-locking between the oscillations in the layers was hard to achieve. Only recently it was discovered that relatively large mesas (about $300\,\mu$m long, 50 to $100\,\mu$m wide, and $1\,\mu$m thick) defined in a single crystal of BSCCO were able to emit coherent electromagnetic radiation of significant power (a few μW) in the THz range [69]. It is assumed that the mesa forms an electromagnetic cavity and the Josephson oscillations in the individual junctions are synchronized by the alternating electromagnetic field stored in the cavity resonance. The dynamics of a stack of coupled IJJs is very complex. Therefore, the precise mechanism is in dispute.

We used the experimental technique of low-temperature scanning laser microscopy (LTSLM) in order to investigate similar $Bi_2Sr_2CaCu_2O_8$ mesas. This technique is comparable to low-temperature scanning electron microscopy (LTSEM) [35]. The sample is mounted in vacuum on the cold finger of a He-continuous-flow cryostat. A laser beam (alternatively an electron beam) is focused on the sample surface, locally heating the sample in the vicinity of the laser spot (electron probe) at the position (x,y). Simultaneously, the electrical resistance of the sample is monitored by 4- or 2-wire sensing. By blanking the laser (electron) beam and using lock-in technique, the response, i.e., the beam induced voltage change $\Delta V(x, y)$ of this global electrical measurement to the heat distribution at the location (x, y) can be detected. Scanning the laser (electron) beam and mapping the response $\Delta V(x, y)$ leads to the so-called voltage image of the sample. Depending on the sample under investigation, this voltage image can be a map of all kinds of physical properties (e.g. critical current or

critical temperature distributions in superconducting thin films [35] or microwave amplitude in microstrip lines [47]). The spatial resolution of the images depends on the size of the heat distribution and is usually about 2-3 μm. The study presented here was started with two objectives: The first objective was to image the standing wave pattern in the bias regime where Ozyuzer et al. had discovered THz emission. The second objective was to investigate the temperature, respectively, the current distribution in mesas of such a considerable size. Strong joule heating is generated by the relatively high input power for high-bias currents. Therefore an inhomogeneous temperature and current distribution in the mesa can be expected. This temperature distribution might influence the emission of THz radiation. In the course of this study, it turned out that the capability of detecting electromagnetic radiation in the THz frequency range would be very helpful to confirm the results. Therefore, the author of this thesis suggested to build an interferometer similar to [24, 66] with the difference that a bolometer would be used instead of a pyroelectric detector or a Golay cell. This set-up was realized at the National Institute of Material Science in Japan.
This part of the thesis is organized in the following way: In the chapter "Fundamentals" a short summary of the physics in Josephson junctions is provided before the complexity of stacks of strongly coupled intrinsic Josephson Junctions in $Bi_2Sr_2CaCu_2O_8$ is regarded. The chapter "Experimental methods" starts with a few words concerning sample preparation. Then the LTSLM technique is described in detail with the focus on the individual response mechanism resulting in a voltage image. Finally, the working principle of the interferometer set-up is described. The first section of the chapter "Results & Discussion" is devoted to the imaging at the low bias regime where Ozyuzer et al. had discovered THz emission. In the second part, the phenomenon of self-heating in a $Bi_2Sr_2CaCu_2O_8$ stack is discussed. In the last section, emission measurements are presented.

2. Theory & Fundamentals

2.1. The Josephson effect

If a superconductor is cooled down below a certain critical temperature T_c more and more charge carriers condensate into a macroscopic quantum state by forming Cooper pairs. This macroscopic quantum state can be described by one wave function

$$\Psi(\vec{r}, t) = \sqrt{n_s} e^{i\phi} \tag{2.1}$$

where n_s is the Cooper pair density. By using the equation for the quantum mechanical probability flux [80, p. 131] (taking into account that a Cooper pair carries a charge of $-2e$), the supercurrent density can be calculated:

$$\vec{j}_s = \frac{n_s}{2\, m_e}(\hbar \nabla \phi - 2e\vec{A}) \tag{2.2}$$

Here m_e is the electron mass and $\vec{A}$ is the magnetic vector potential.
There are many ways to establish a weak link between two superconducting electrodes (e.g. point contacts, micro bridges, or tunnel junctions [11, p. 54]). They all have in common that, although the Cooper pair density is suppressed significantly, the wave functions of both electrodes still overlap. This leads to the fundamental Josephson effect, which is explained in the following.

ϕ_1 and ϕ_2 are the phases in electrode 1 and electrode 2. The gauge invariant phase difference γ is defined as:

$$\gamma = \phi_2 - \phi_1 - \frac{2e}{\hbar} \int_1^2 \vec{A} d\vec{s} \tag{2.3}$$

Consider the weak link in figure 2.1. Because the electric current is preserved along the superconductor, a suppression of the charge-carrier density leads to a shift in the superconducting phase ϕ according to equation

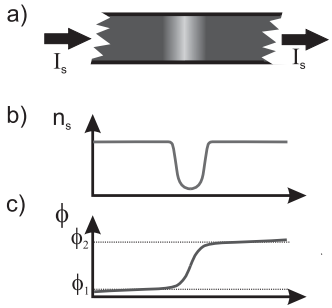

Figure 2.1.: a) Scheme of a superconducting weak link; b) suppression of the cooper pair (charge carrier) density; c) shift in the superconducting phase

2.2. Hence, it is plausible that the supercurrent across the weak link I_s is a function of γ. Because the wave function is invariant under a phase shift of 2π, I_s is periodic in γ, too.

$$I_s(\gamma) = \sum_{n=0}^{\infty} I_{cn} \sin(n\gamma) + \sum_{n=0}^{\infty} \tilde{I}_{cn} \cos(n\gamma) \tag{2.4}$$

The system is invariant under time reversal. Therefore, the cosine terms vanish. Usually, this series converges very fast and only the first term dominates.

$$I_s = I_c \sin(\gamma) \tag{2.5}$$

This equation, which is referred to as the first Josephson equation, implies that the electrical current over a superconducting weak link is determined by the critical current I_c and the gauge invariant phase difference γ between the electrodes.
Taking the derivative with respect to time of equation 2.3 leads to:

$$\dot{\gamma} = \underbrace{\dot{\phi}_2 - \dot{\phi}_1}_{\frac{2e}{\hbar} U_{21}} - \frac{2e}{\hbar} \underbrace{\int_1^2 \dot{\vec{A}}\, d\vec{s}}_{-U_{ind}} = \underbrace{\frac{2e}{\hbar}}_{\frac{2\pi}{\Phi_0}} U \tag{2.6}$$

Applying the Schrödinger equation to the wave function 2.1 confirms that the derivative of the phase in an electrode with respect to time is proportional to the electrical potential. Therefore, the first part is proportional to the voltage between the electrodes. The second part is proportional to the voltage induced by a magnetic field corresponding to the vector

potential $\vec{A}$.
Equation 2.6 is called the second Josephson equation. It has the following consequences: If the current across a superconducting weak link is increased above I_c, the superconducting state is no longer able to support the current. For that reason the charge carriers that are not part of the condensate (the so-called quasiparticles) carry the current. This causes a voltage drop across the weak link. By integrating the second Josephson relation over time and considering the first Josephson relation, it is easy to see that this voltage drop causes an alternating super current with the amplitude I_c. This is referred to as the AC-Josephson effect.
To conclude: A superconducting weak link, which in the following is called a Josephson Junction, is an ideal voltage-to-frequency converter with Josephson frequency $f_J = \frac{U}{\Phi_0} = 483.6[\frac{GHz}{mV}]U$, where $\Phi_0 = h/2e = 2.07 \cdot 10^{-15}$Wb is the flux quantum.

2.2. The RCSJ model

The two Josephson equations are not sufficient to describe the dynamics of a Josephson Junction (JJ). In a real JJ the Josephson current I_S is superimposed by a quasiparticle tunneling current I_R and by a displacement current I_C between electrodes. In the **r**esistively and **c**apacitively **s**hunted **j**unction model, these currents are super positioned linearly (c.f. figure 2.2, [63, 91]). In most cases the quasiparticle tunneling current can be modeled by ohmic behavior: $I_R = U/R$
Even a small capacitance of the junction cannot be ignored because of the high frequency of the Josephson current: $I_C = C\frac{d}{dt}U$
By taking the two Josephson equations into account, the total current can be expressed with the gauge invariant phase difference γ:

$$I = I_c \sin\gamma + \frac{1}{R}\frac{\Phi_0}{2\pi}\dot{\gamma} + C\frac{\Phi_0}{2\pi}\ddot{\gamma} \tag{2.7}$$

Defining the normalized current $i = \frac{I}{I_c}$, the characteristic frequency $f_c = \frac{I_c R}{\Phi_0}$, the McCumber parameter $\beta_c = 2\pi RCf_c$, and the normalized time $\tau = 2\pi f_c t$ equation 2.7 can be simplified to:

$$i = \sin\gamma + \frac{d}{d\tau}\gamma + \beta_c\frac{d^2\gamma}{d\tau^2} \tag{2.8}$$

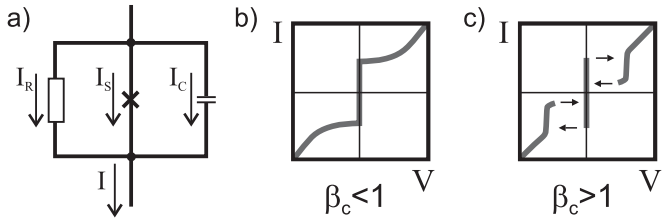

Figure 2.2.: a) Circuit diagram of a Josephson junction according to the RCSJ-model; b) IV-curve of an overdamped Josephson Junction; c) IV-curve of an underdamped Josephson Junction.

It is easy to see that equation 2.8 is equivalent to the equation of motion of a particle in a tilted washboard potential $U(\gamma) = \cos(\gamma) - i\gamma$ of mass β_c. The prefactor in the damping term is one. This means that the mass of the particle is expressed in the units of [1/(damping parameter)]. Therefore, β_c is the ratio of inertia and damping.
The parameter i is a measure of how strong the washboard potential is tilted. If $i < 1$ (this means $I < I_c$), the particle will be trapped in one of the minima of the potential. If i is increased above 1, the particle can escape and starts moving, or in the case of a Josephson Junction, an alternating Josephson current is generated. If i is reduced below 1 again, the behavior of the system depends on the damping. In the case of strong damping (overdamped) or $\beta_c < 1$, the particle will be retrapped immediately. Refer to figure 2.2 b) for the current-voltage dependence of a corresponding Josephson junction. In the case of weak damping (underdamped) or $\beta_c > 1$, the inertia keeps the particle moving until the particle is retrapped. This leads to a bistable or hysteretic behavior, cf. figure 2.2 c).
To consider the response to perturbations with small amplitudes, one can linearize the $\sin\gamma$ term and use the following Ansatz $\dot{\gamma} = \frac{2\pi}{\Phi_0}\hat{V}e^{i\omega t}$. Equation 2.7 then becomes (for zero external driving current I):

$$0 = -i \underbrace{\frac{2\pi I_c}{\Phi_0}}_{\frac{1}{L_J}} \frac{1}{\omega} + \frac{1}{R} + i\,C\omega \tag{2.9}$$

This is the differential equation of an oscillating circuit, where the Josephson Junction represents an inductance with the effective inductivity $L_J = \frac{\Phi_0}{2\pi I_c}$. The resonance frequency (the so-called plasma frequency) is $f_{pl} = \frac{1}{2\pi\sqrt{L_J C}} = \frac{f_c}{\sqrt{\beta_c}}$ and the quality factor is $Q = R\sqrt{\frac{C}{L_J}} = \sqrt{\beta_c}$.

2.3. Linewidth of a Josephson oscillator

Most of the following derivation, which is summarized here, can be found in [58].
The spectral density of a variable X(t) in a stationary process is defined as

$$S_X(\omega)\delta(\omega - \omega') \equiv \frac{1}{2}\left\langle X_\omega X^*_{\omega'} + X_{\omega'} X_\omega \right\rangle \tag{2.10}$$

where $X(\omega)$ is the Fourier transform of $X(t)$

$$X(t) = \int_{-\infty}^{\infty} X(\omega) e^{i\omega t} d\omega, \quad X(\omega) = \frac{1}{2\pi}\int_{-\infty}^{\infty} X(t) e^{-i\omega t} dt \tag{2.11}$$

and the brackets $< \cdots >$ denote the statistical averaging.
According to definition 2.10, the mean square value of X in a small interval is

$$\left\langle X^2 \right\rangle d\omega = S_X(\omega)d\omega + S_X(-\omega)d\omega = 2S_X(\omega)d\omega \tag{2.12}$$

First, a Josephson Junction in the RCSJ model under an ideal, i.e., noise free-bias $\bar{I}(t)$, is considered [19]: Both the Josephson junction and the capacitor are free of noise. If the voltage over the sample is considerably smaller than $\frac{k_B T}{e}$, then the only noise sources are the thermal excitations in the resistor causing a current noise I_F with a spectral density, which is frequency independent (white noise) and proportional to the temperature:[1]

$$S_I(\omega) = \frac{1}{\pi} G_N \, k_B \, T \tag{2.13}$$

[1] By considering frequency instead of angular velocity and taking equation 2.12 into account, this expression can be rearranged into the better known $(\bar{i})^2 = 4k_b T \, G_N$.

where G_N denotes the conductivity of the resistor and k_B the Boltzmann-factor (Johnson-Nyquist formula).
Adding current noise to the RSCJ model results in

$$\bar{I} = \underbrace{I_c \sin(\gamma(t))}_{\to 0} + \frac{1}{R_d}(\bar{V} + \widetilde{V}) + C\frac{d}{dt}(\bar{V} + \widetilde{V}) + I_F \tag{2.14}$$

where R_d is the differential (dynamic) resistivity, C the capacitance of the junction and $\bar{I}$, $\bar{V}$ are the statistically averaged (noise-free) values. In the high frequency limit, i.e., the Josephson frequency is much larger than the plasma frequency (which is the case for an underdamped junction), the supercurrent term can be neglected and the preceding equation 2.14 results in

$$C\frac{d\widetilde{V}}{dt} + \frac{1}{R_d}\widetilde{V} = \widetilde{I}, \quad \widetilde{I} = -I_F \tag{2.15}$$

Using the Fourier transform of $\widetilde{V}$ and $\widetilde{I}$, one obtains

$$S_V(\omega) = R_d^2 S_I(0)/(1 + \omega^2\tau_d^2), \quad \tau_d \equiv R_d C \tag{2.16}$$

Hence,

$$S_V(0) = R_d^2 S_I(0) \tag{2.17}$$

According to the Josephson relation, the voltage fluctuations characterized by the spectral density $S_V(\omega)$ are influencing the Josephson oscillations. Hence, the question is: What is the spectral density of an oscillation with phase noise?
It can be shown [92, 90], that in the case of a nearly constant spectral density $S_V(\omega)$ in the range of $0 \leq \omega \lesssim \Gamma$ (i.e., according to equation 2.16 $\Gamma \ll \frac{1}{\tau_d}$), the spectral density of the Josephson oscillations becomes Lorentzian-shaped

$$S_{sin\left(\frac{2\pi}{\phi_0}(\bar{V}+\widetilde{V})t\right)}(\omega) = \frac{1}{4\pi}\frac{\Gamma}{(\omega - \omega_J)^2 + \Gamma^2} \tag{2.18}$$

with a halfwidth of

$$\Gamma = \pi\left(\frac{2e}{\hbar}\right)^2 S_V(0) \tag{2.19}$$

For the other case, in the limit of low-frequency noise where the components of $S_V(\omega)$ can be ignored above a certain cut off frequency (i.e., according to equation 2.16 $\Gamma \gg \frac{1}{\tau_d}$), the line shape is Gaussian

$$S_{sin\left(\frac{2\pi}{\phi_0}(\bar{V}+\tilde{V})t\right)}(\omega) = \frac{1}{4}\sigma(\omega-\omega_J,\Gamma) \tag{2.20}$$

where

$$\Gamma = \frac{2e}{\hbar}\left[2\int_0^\infty S_V(\omega)d\omega\right]^{1/2}, \quad \sigma(X,\delta) = \frac{1}{\sqrt{2\pi}\delta}\exp\left(\frac{-X^2}{2\delta^2}\right) \tag{2.21}$$

In the first case, using equation 2.18 and equation 2.13 one obtains

$$\Gamma = R_d^2\left(\frac{2e}{\hbar}\right)^2 G_N\, k_B\, T \tag{2.22}$$

which can be simplified assuming $R_d = 1/G_N \equiv R_N$

$$\Gamma = \left(\frac{2e}{\hbar}\right) R_N\, k_B\, T \tag{2.23}$$

Note that the angular velocity is used in equation 2.23 and the line width Γ has to be doubled to calculate the FWHM. Hence, the frequency line width of the Josephson oscillation is

$$\Delta\nu = \underbrace{\frac{k_B}{\pi}\left(\frac{2e}{\hbar}\right)^2}_{\approx 40\,\frac{\mathrm{MHz}}{\Omega\,\mathrm{K}}} R_N\, T \tag{2.24}$$

For a tunnel junction, the voltage usually exceeds $k_B\,T/e$ and shot noise is of major importance. Using a microscopic theory [58] leads to a more complicated expression for the spectral density of the current noise

$$S_I(0) = \frac{eI_N(\bar{V})}{2\,\pi}\coth\left(\frac{e\bar{V}}{2k_B\,T}\right) \tag{2.25}$$

and for the line width of the Josephson oscillation

$$\Delta\nu = \left(\frac{2e}{\hbar}\right)^2 \frac{eI_N(\bar{V})}{2\,\pi}\coth\left(\frac{e\bar{V}}{2k_B\,T}\right) R_d^2 \tag{2.26}$$

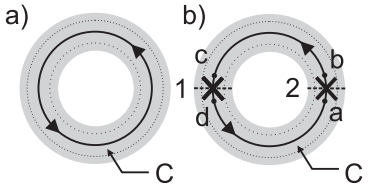

Figure 2.3.: a) Diagram of a superconducting ring; b) Diagram of a superconducting ring divided by two Josephson Junctions.

2.4. Fluxoid quantization/quantum interference

Considering a superconducting ring (figure 2.3 a)), because the macroscopic wave function in the ring has to be single-valued the path integral along the curve C over the gradient of the phase has to be multiples of 2π:

$$2\pi n = \oint \nabla\phi \, d\vec{s} \tag{2.27}$$

If the path C is chosen to run inside the superconductor where the current density vanishes due to Meissner screening, it follows from equation 2.2 and equation 2.27:

$$2\pi n = \oint_C \nabla\phi \, d\vec{s} = \frac{2\pi}{\Phi_0} \oint_C \vec{A} \, d\vec{s} = \frac{2\pi}{\Phi_0} \int \mu_0 \vec{H} \, d\vec{f} = 2\pi \frac{\Phi}{\Phi_0} \tag{2.28}$$

Hence, fluxoids are quantized in units of the flux quantum Φ_0.
Now the ring shall be divided by two Josephson Junctions (refer to figure 2.3). By choosing the same path as before and with the help of equation 2.27, equation 2.2, and equation 2.3, one gets:

$$\begin{aligned} 2\pi n = \oint_C \nabla\phi \, d\vec{s} = \frac{2\pi}{\Phi_0} \int_b^c \vec{A} \, d\vec{s} + \phi(d) - \phi(c) \\ + \frac{2\pi}{\Phi_0} \int_d^a \vec{A} \, d\vec{s} + \phi(a) - \phi(b) = \frac{2\pi}{\Phi_0} \oint_C \vec{A} \, d\vec{s} - \gamma_1 + \gamma_2 \\ \Rightarrow \gamma_2 - \gamma_1 = \frac{2\pi\Phi}{\Phi_0} \bmod 2\pi \end{aligned} \tag{2.29}$$

Here $\phi(x)$ is the phase at the point x and γ_m is the gauge invariant phase difference at the junction m.
Equation 2.29 implies that γ_1 and γ_2 cannot simultaneously have the value $\frac{\pi}{2}$, as would be required to give the largest supercurrent over the

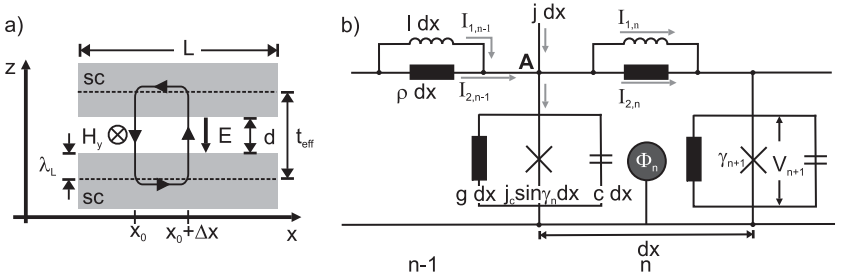

Figure 2.4.: a) Diagram of a long Josephson Junction; b) Lumped circuit model of a long Josephson Junction.

ring, unless the flux Φ is an integral multiple of Φ_0. The modulation of the maximum supercurrent due to quantum interference of the superconducting wave function is the basis for the dc-SQUID magnetometer.

2.5. The sine-Gordon equation

In laterally extended planar Josephson Junctions, the quantum interference of the superconducting wave function described in the preceding section has to be considered. Therefore, the RCSJ model is insufficient. In the following, two different derivations of the sine-Gordon equation are presented, which describes the dynamics of extended Josephson Junctions. In the first derivation, a spatial dependence of the gauge invariant phase difference is introduced and then the quantum interference is worked in. While in the second approach, the Josephson Junction is discretized and replaced by an equivalent electric circuit.

2.5.1. Derivation of the sine-Gordon equation with a continuous junction model

Figure 2.4 a) depicts a scheme of an extended Josephson Junction. γ is influenced by the in-plane component of the magnetic field only. Without loss of generality, the magnetic field direction is assumed to point into the y-direction. Due to the Meissner effect, the magnetic field is screened from the interior of the electrodes. The effective thickness of the JJ in terms

of the magnetic field is called t_{eff}. For electrodes that are considerably thicker than the London penetration depth λ_L, the effective thickness is:

$$t_{\text{eff}} = 2\lambda_L + d \tag{2.30}$$

Here d is the distance of the superconducting electrodes in the JJ.
In order to calculate the change of γ at the point x_0 in the interval Δx, a rectangular integration path is chosen where the horizontal lines run in an area of the electrodes with zero magnetic field (cf. figure 2.3 c)). It follows with the same line of argument as in the preceding chapter:

$$\gamma(x_0 + \Delta x) - \gamma(x_0) = \frac{2\pi}{\Phi_0}\mu_0 H_y\, t_{\text{eff}} \Delta x \Rightarrow \partial_x \gamma = \frac{2\pi}{\Phi_0}\mu_0\, t_{\text{eff}} H_y$$
$$\text{(analog with H in the x-direction)} \quad \partial_y \gamma = -\frac{2\pi}{\Phi_0}\mu_0\, t_{\text{eff}} H_x \tag{2.31}$$

Like in the RCSJ model the Josephson current, the quasiparticle current, and displacement current should be considered. Hence, the Maxwell equation leads to:

$$\partial_x H_y - \partial_y H_x = j_c \sin\gamma + \sigma E + \epsilon\epsilon_0 \dot{E} \tag{2.32}$$

Where σ is the conductivity and ϵ is the permittivity. Using the 2. Josephson equation and equation 2.32 this implies:

$$\frac{\Phi_0}{2\pi\mu_0\, t_{\text{eff}}}\left[\partial_x^2\gamma + \partial_y^2\gamma\right] = j_c \sin\gamma + \frac{\Phi_0\,\sigma}{2\pi\, d}\partial_t\gamma + \frac{\Phi_0\,\epsilon\epsilon_0}{2\pi\, d}\partial_t^2\gamma \tag{2.33}$$

This equation is called the perturbed sine-Gordon equation [30]. Defining following abbreviations

$$\text{Josephson penetration depth: } \lambda_J^2 = \frac{\Phi_0}{2\pi\mu_0\, t_{\text{eff}} j_c} \tag{2.34a}$$

$$\text{plasma frequency: } \omega_{pl}^2 = \frac{2\pi\, d\, j_c}{\Phi_0\,\epsilon\epsilon_0} \tag{2.34b}$$

$$\text{damping parameter: } \alpha = \frac{\Phi_0\,\sigma}{2\pi\, d\, j_c} \tag{2.34c}$$

the perturbed sine-Gordon equation can be written in compact form:

$$\lambda_J^2\left[\partial_x^2 + \partial_y^2\right]\gamma = \sin\gamma + \alpha\partial_t\gamma + \frac{1}{\omega_{pl}^2}\partial_t^2\gamma \tag{2.35}$$

If the damping term is neglected, this equation is called (unperturbed) sine-Gordon equation:

$$\lambda_J^2 \left[\partial_x^2 + \partial_y^2\right] \gamma = \sin\gamma + \frac{1}{\omega_{pl}^2}\partial_t^2\gamma \tag{2.36}$$

With the help of the sine-Gordon equation, it is easy to see that the Josephson penetration depth λ_J is the length-scale for the variation of the gauge invariant phase difference γ.
A Josephson Junction with lateral dimensions smaller than the Josephson penetration depth λ_J is called a short junction and a JJ with lateral dimensions considerable longer than λ_J is called a large junction. If only one dimension is considerable longer than λ_j, such a junction is called a long junction.

2.5.2. Derivation of the sine-Gordon-equation with a lumped circuit model

In this section the sine-Gordon equation for a long Josephson Junction is derived by replacing the system with an equivalent parallel circuit of short Josephson Junctions, which are described by the RCSJ model, cf. figure 2.4. A long Josephson Junction can also be considered as a special transmission line – a so-called Josephson transmission line. The series impedance per unit length can be expressed as a parallel combination of a frequency-independent surface (sheet) resistance per unit length ρ and a frequency-independent inductance per unit length l [85]. $I_{1,n}$ ($I_{2,n}$) denotes the current over the inductance (sheet resistance). The definition of the inductance and equation 2.29 imply[2]

$$\gamma_{n+1} - \gamma_n = -\frac{2\pi\, I_{1,n}\, l}{\Phi_0} dx \implies I_1 = -\frac{\Phi_0}{2\pi l}\frac{\partial\gamma}{\partial x} \tag{2.37}$$

and applying Kirchhoff's voltage law on the n-th mesh leads to

$$V_{n+1} - V_n = -I_{2,n}\,\rho\, dx \implies I_2 = -\frac{1}{\rho}\frac{\partial V}{\partial x} \tag{2.38}$$

[2] An external magnetic field can be considered in the boundary conditions by introducing an "equivalent external magnetic current" [58, p. 226].

According to Kirchhoff's current law at node A

$$\frac{\partial\,(I_1 + I_2)}{\partial x} = j - c\frac{\partial V}{\partial t} - g\,V - j_c\,\sin\gamma \tag{2.39}$$

Using the second Josephson equation and normalizing the time coordinate with the inverse of the plasma frequency and the spatial coordinate with the Josephson penetration depth

$$\frac{t}{\omega_{\mathrm{pl}}^{-1}} \to t \quad \text{with } \omega_{\mathrm{pl}} = \sqrt{\frac{2\pi\, j_c}{\Phi_0 c}} \tag{2.40a}$$

$$\frac{x}{\lambda_J} \to x \quad \text{with } \lambda_J = \sqrt{\frac{\Phi_0}{2\pi\, l\, j_c}} \tag{2.40b}$$

leads to the perturbed sine-Gordon equation again

$$\partial_x^2\gamma - \partial_t^2\gamma = \sin\gamma + \alpha\partial_t\gamma - \beta\partial_x^2\partial_t\gamma - \frac{j}{j_c} \tag{2.41}$$

Here

$$\alpha = \frac{\Phi_0\, g}{2\pi\, j_c}\omega_{\mathrm{pl}} \tag{2.42}$$

is the damping factor,

$$\beta = \frac{l}{\rho}\omega_{\mathrm{pl}} \tag{2.43}$$

is the damping factor due to surface losses, and j is the injection current. The capacitance per unit length and the inductance per unit length can be obtained by comparing equation 2.40 with equation 2.34

$$c = \epsilon\epsilon_0\, w/d; \quad l = \mu_0(2\lambda_L + d)/w \tag{2.44}$$

w is the width of the long Josephson Junction, λ_L is the London penetration depth of the top and bottom electrode, and d is the barrier thickness.

2.6. Solutions of the sine-Gordon equation

The non-linearity of the sine-Gordon equation can cause highly complex dynamics. This chapter is restricted to two prominent solutions. For the sake of simplicity, only the one-dimensional unperturbed sine-Gordon equation is discussed.

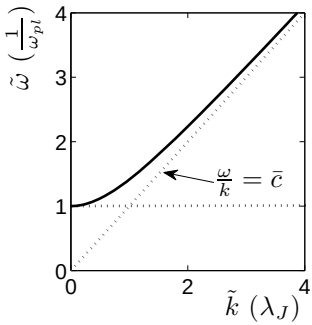

Figure 2.5.: Dispersion relation $\omega/\omega_{\mathrm{pl}} = \sqrt{1 + k^2\lambda_j^2}$ of a plasma wave in long Josephson Junction. The horizontal dashed line indicates the plasma gap.

2.6.1. Plasma waves

The sine-term in the sine-Gordon equation is linearized in order to analyze the dynamic of small deflections. This leads to the well-known wave equation:

$$\lambda_J^2 \partial_x^2 \gamma - \frac{1}{\omega_{\mathrm{pl}}^2} \partial_t^2 \gamma - \gamma = 0 \tag{2.45}$$

The solution is found through transversal waves $\gamma = \exp\left[i(\omega + k\,x)\right]$ with following dispersion relation:

$$\omega^2 = \omega_{\mathrm{pl}}^2 + k^2 \omega_{\mathrm{pl}}^2 \lambda_J^2 \tag{2.46}$$

These waves are usually referred to as plasma waves. The Swihart velocity is defined as:

$$\bar{c} = \omega_{\mathrm{pl}} \lambda_J \tag{2.47}$$

For large k values the dispersion relation approaches the linear dispersion relation of a free wave with a phase velocity that equals the Swihart velocity (cf. figure 2.6.1). Only waves with a frequency above the plasma frequency can be excited (plasma gap).
In a conventional planar Josephson tunneling junction, the Swihart velocity is only a small fraction of the velocity of light. Such a configuration can be considered as a transmission line. The electric field cannot penetrate the superconducting electrodes. While the electric field is compressed, the magnetic field can occupy considerably more space. This leads to the slowdown in the wave propagation [95].

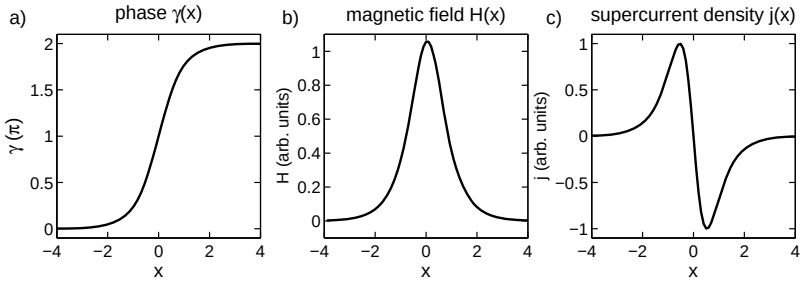

Figure 2.6.: "Snap-shot" of a) the phase, b) the magnetic field, and c) the supercurrent density distribution corresponding to a soliton in a Josephson Junction. The length scale is normalized to the Josephson penetration depth λ_J.

2.6.2. The soliton/fluxon solution

A medium is called dispersive if the phase velocity $\frac{\omega}{k}$ is not constant. For a medium that is in addition linear (i.e., it is described by linear wave equation), a locally defined wave packet disperses, because the plane waves that the wave packet is composed of propagate with different velocities. This is independent of the form of the wave packet. The most prominent example is the dispersion of a probability wave corresponding to a free particle in quantum mechanics.
In a non-linear medium, an oscillation with one frequency can convert into an oscillation with another frequency. In such a medium, it is possible to prepare a special wave packet for which the dispersion is compensated by the non-linearity effect. This wave packet would propagate with a certain group velocity without changing its shape. Such a wave packet, or in other words such a solution to the wave equation, is called a soliton.
It can be shown that the sine-Gordon equation has a soliton solution of the following form ([4, p. 264 ff.] :

$$\gamma(x,t) = 4\arctan\left[\exp\left(\pm\frac{x-ut}{\lambda_J\sqrt{1-\frac{u^2}{\bar{c}^2}}}\right)\right] \text{ with } |u| < \bar{c} \tag{2.48}$$

u denotes the velocity of the soliton. The sign in the exponential function indicates a soliton and an antisoliton respectively.
This solution corresponds to a phase shift of 2π (2π-kink) that propagates through the junction (cf. figure 2.6 a)). According to equation 2.31, the magnetic field distribution can be easily calculated (figure 2.6 b)) and the 1. Josephson equation leads to the current distribution (figure 2.6 c)). A soliton corresponds to a circulating supercurrent that carries one flux quantum Φ_0. For that reason some authors refer to a soliton in a Josephson Junction as a Josephson vortex or fluxon. In contrast to a vortex in a type 2 superconductor, there is no normal conducting core in a Josephson vortex.

2.7. Boundary conditions

The junction geometry and the externally applied magnetic field determine the boundary conditions, which have a significant effect on the junction properties. This is elucidated in the following sections by a few simple examples.

2.7.1. A small junction in an external field

The effect of a magnetic field that lies in-plane of a small planar Josephson Junction is discussed. Without loss of generality, the magnetic field is chosen to point into the y-direction. Because the junction is small, the self-field effect can be neglected. Integrating equation 2.31 results in:

$$\gamma = \frac{2\pi}{\Phi_0}\mu_0 t_{\text{eff}} H_y x + \gamma_0 \tag{2.49}$$

For a stationary solution, the sine-Gordon equation is reduced to the 1. Josephson equation. Equation 2.49 is inserted into the 1. Josephson equation and implies:

$$j(x,y) = j_c(x,y)\sin\left(\frac{2\pi}{\Phi_0}\mu_0 t_{\text{eff}} H_y x + \gamma_0\right) \tag{2.50}$$

Therefore, the Josephson current density exhibits a periodic distribution inside the junction. This periodic distribution can be considered as a stationary chain of Josephson vortices. The number of Josephson vortices is

proportional to the applied magnetic field. It can be shown that the maximum Josephson current at a given magnetic field $I_{\max}(k)$ is represented by the modulus of the Fourier transform of I_y (cf. [4, *ff.* p.71]).

$$I_{\max}(k) = \left| \int_{-\infty}^{\infty} dx I_y \exp(ikx) \right| ; \; k \equiv \frac{2\pi}{\Phi_0} \mu_0 t_{\text{eff}} H_y \tag{2.51}$$

Where I_y is defined as:

$$I_y = \int dy j_c(x, y) \tag{2.52}$$

This explains the well-known Fraunhofer pattern of the critical current vs. magnetic field for a rectangular planar Josephson Junction.

2.7.2. Geometry effects in long junctions

In this section, only stationary solutions sall be regarded. For strong magnetic fields, the current distribution is similar to the one in the preceding section. Because of the self-field effect, the current distribution of the stationary Josephson vortex chain is not sinusoidal, but the shape of the Josephson vortices is similar to figure 2.6.
There are three different geometries in which a long junction can be realized. The first geometry is the overlap geometry, where the bias current is injected perpendicular to the long side of the junction. The uniform current distribution has to be considered by an additional term in the sine-Gordon equation. The second geometry is the inline junction. Here, the current is injected perpendicular to one short side of the junction and is drained off the opposite side. For small magnetic fields, the current density is significantly increased at both short edges of the junction. The third geometry is the asymmetric in-line junction, where the current is injected and drained at the same short side. The current density is increased at only one side. These geometry effects are reduced when the junction is located above a superconducting ground plane, which creates an image current line. For a more detail discussion of the geometry effect, refer to [4, 3, 94].

2.8. Resonances in Josephson Junctions

In the preceding sections, it was shown that a Josephson Junction is both a cavity for plasma waves and a Josephson oscillator, which in some cases exhibits very complex dynamics of Josephson vortices. Those oscillators can cause a variety of resonances that influence the current-voltage behavior of the junction.

2.8.1. Shapiro steps

If a Josephson Junction is irradiated with microwaves of angular frequency ω_r, constant voltage steps in the dc IV-curve appear at voltages $V_n = n\frac{\hbar}{e}\omega_r$. These so-called Shapiro steps are caused by the phase-locking of the Josephson oscillation to the external electromagnetic field. In order to calculate the height of the Shapiro steps, the microwave radiation is treated as an alternating voltage source. The total voltage applied to the junction can be written as $V(t) = V_0 + v\cos(\omega_r t)$. With the help of the Josephson relations and by expanding the sine into Bessel functions, the following equation for the maximum height of the n-th step can be deduced.

$$I_n = I_c \left| J_n \left(\frac{nv}{V_0} \right) \right| \tag{2.53}$$

J_n is the n-th Bessel function.

2.8.2. The Fiske resonance

First, small junctions are discussed. If the junction is in the resistive state, the oscillating Josephson current is uniformly distributed along the junction. On the other hand, the different modes of the plasma oscillation are associated with a characteristic non-uniform alternating current distribution. Hence, there is only a small interaction between the Josephson oscillator and the Josephson plasma.
Things change when an in-plane magnetic field of sufficient strength is applied. Now the Josephson current is sinusoidaly modulated in the direction perpendicular to the magnetic field (cf. section 2.7.1) and the corresponding plasma mode is excited. Again, the magnetic field should point into the y-direction and the junction has the length L in x-direction.

For open-ended boundary conditions, the standing wave current pattern in x-direction for the n-th mode is

$$i(x,t) = A_n \exp(i\omega_n t) \sin(\frac{n\pi x}{L}) \tag{2.54}$$

with the angular frequency

$$\omega_n = \frac{n\pi\bar{c}}{L} \tag{2.55}$$

Therefore, the interaction of the Josephson oscillation and the plasma modes creates voltage steps at

$$V_n = \frac{\hbar}{2e}\omega_n = \frac{h}{2e}\frac{\bar{c}}{2L}n \tag{2.56}$$

By choosing the corresponding magnetic field, those resonances can be selected.
For a long junction, the fluxon dynamics have to be considered [72, 25]. By applying an external magnetic field, the reflection of fluxons is enhanced at one end of the junction, i.e., energy is added to the system while at the other end the reflection is impeded, i.e, energy is subtracted. For a sufficiently strong magnetic field, the fluxons at one end of the junction are just annihilated, giving rise to a small amplitude wave packet that propagates along the junction and triggers the creation of a fluxon on the other end. This creates the Fiske steps at the same voltage mentioned above.

2.8.3. Zero field steps

If the driving current on a long underdamped Josephson Junction is reduced after the junction has switched into the resistive state, fluxon-antifluxon pairs are spontaneously created. Respectively, the fluxon and antifluxon are driven along the junction in opposite directions. At the junction edge, the fluxon is reflected as an antifluxon and vice versa. The sine-Gordon equation is invariant under the Lorentz transformation, where the Swihart velocity corresponds to the speed of light. Therefore, the Josephson fluxons can be regarded as relativistic particles. Hence, the energy that is needed to accelerate a fluxon with a velocity near the Swihart velocity diverges. This creates steps in the IV-curve.

In order to calculate the position of the steps, one fluxon that is reflected as an antifluxon shall be considered. The velocity of the fluxon should be near the Swihart velocity $v \approx \bar{c}$. In a junction of length L, a full period of motion back and forth takes time $T = 2L/\bar{c}$ and accomplishes an overall phase advance of 4π. The second Josephson equation implies:

$$\langle \dot{\gamma} \rangle = \frac{4\pi n}{T} = \frac{2\pi \bar{c} n}{L} = \frac{2\pi}{\Phi_0} V_n \tag{2.57}$$

Therefore, the voltage is

$$V_n = n \frac{\Phi_0 \bar{c}}{L} \tag{2.58}$$

The spacing between the zero field steps is twice as much as between the Fiske steps.
It should be noted that zero field steps are not restricted to long junctions characterized by soliton dynamics. By taking into account the first-order harmonics in the perturbed sine-Gordon equation, Takanaka was able to derive zero field steps corresponding to cavity resonance modes [96]. The zero field steps occur at voltages below a temperature-dependent cut-off voltage $V_c = \frac{\hbar(\bar{c}/\lambda_j)^2}{2e\alpha}$ only.

2.8.4. Eck peak/Flux-flow step

If the damping and/or the magnetic field is increased, the line widths of the Fiske resonances increases and they merge into a single peak (Eck peak) [58]. Because of the high magnetic field, fluxons are injected at a high rate in one end of the junction. This way, a flux-flow state is created, which is a chain of fast-moving fluxons. If the speed of the flux-flow state is approaching the Swihart velocity, this current wave interacts strongly with a traveling electromagnetic wave of the same velocity. That is why the Eck-peak or flux-flow step sometimes is called a velocity-matching step.
The number of fluxons in the flux-flow state is $n = \frac{B\,L\,t_{\text{eff}}}{\Phi_0}$. The distance between the fluxons is $l = \frac{L}{n}$. If a fluxon enters the junction, it causes a phase change of 2π. The voltage of the flux-flow state with fluxons moving almost with the Swihart velocity can be calculated:

$$V_{\text{FFS}} = \frac{\langle \dot{\gamma} \rangle}{2\pi} \Phi_0 = \frac{\bar{c}}{l}\,\Phi_0 = \bar{c}\,B\,t_{\text{eff}} \tag{2.59}$$

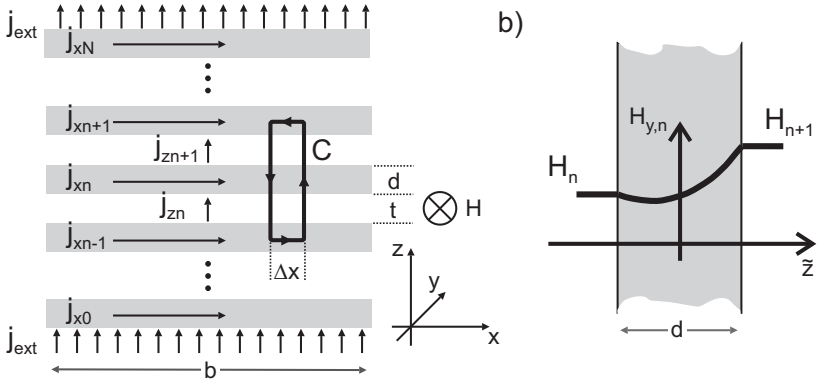

Figure 2.7.: a) Stack of N Josephson Junctions in a magnetic field. Electrodes are numbered from 0 to N. The length of the stack is b. The width of the stack a is assumed to be smaller than the characteristic correlation lengths λ_m and λ_k. The screening currents flowing along the n-th electrode are denoted $j_{\mathrm{x,n}}$. The z-axis currents $j_{\mathrm{z,n}}$ flowing across the n-th electrode of the junction are given by the sum of the Josephson currents, quasiparticle currents, and displacement currents. Transport currents with homogeneous density j_{ext} are fed into the outermost electrodes. The magnetic field is directed along y parallel to the layers. b) Magnetic field distribution $H_{\mathrm{y,n}}$ in the n-th electrode according to the London theory. H_{n} denotes the magnetic field in the tunneling barrier of the n-th junction.

2.9. Dynamics of stacked Josephson Junctions

2.9.1. A stack of inductively coupled junctions

In a stack of Josephson Junctions, with thin superconducting electrodes, the magnetic field in one junction is not completely screened by the Meissner effect. Therefore, the magnetic field penetrates into the neighboring junctions causing inductive coupling. The dynamic of such a system can be described by a set of coupled sine-Gordon equations [79, 73]. In this work, the model described in [52, 49] is used for the derivation.

The stack consists of N planar junctions. The thickness of the superconducting electrodes is d and of the tunneling barriers is t (cf. figure 2.7 a). The magnetic field in the superconducting electrodes can be determined using the London theory.

$$\partial_z^2 H_y(z) = \frac{1}{\lambda_L^2} H_y(z) \tag{2.60}$$

Taking the boundary conditions set by the magnetic fields in the adjacent tunneling barrier into account (cf. figure 2.7 b)) results in

$$H_{\mathrm{n,y}}(\tilde{z}) = \frac{H_{\mathrm{n}} + H_{\mathrm{n+1}}}{2} \frac{\cosh(\tilde{z}/\lambda_L)}{\cosh(d/2\lambda_L)} + \frac{H_{\mathrm{n+1}} - H_{\mathrm{n}}}{2} \frac{\sinh(\tilde{z}/\lambda_L)}{\sinh(d/2\lambda_L)} \tag{2.61}$$

The screening currents j_{xn} can be calculated using Ampère's law

$$j_{\mathrm{xn}}(\tilde{z}=0) = \left(\nabla \times \vec{H}_n\right)_x = -\,\partial_z H_{\mathrm{y,n}}|_{\tilde{z}=0} = \frac{H_{\mathrm{n+1}} - H_{\mathrm{n}}}{2\lambda_L} \frac{1}{\sinh(d/2\lambda_L)} \tag{2.62}$$

Integrating the gauge invariant phase difference along the path C and following the same line of argument as in section 2.4 results in

$$\partial_x \gamma_n = \frac{2e}{\hbar} \left[\partial_x \underbrace{\oint_C \vec{A} d\vec{s}}_{\mu_0 H_{\mathrm{n}} t_{\mathrm{eff}} \Delta x} + \mu_0 \lambda_L^2 (j_{\mathrm{xn}} - j_{\mathrm{xn\text{-}1}}) \right] \tag{2.63}$$

Again Ampère's law implies for the tunneling currents

$$j_{\mathrm{zn}} = \left(\nabla \times \vec{H}_n\right)_z = \partial_x H_{\mathrm{n}} \tag{2.64}$$

Inserting equation 2.62 and 2.64 in equation 2.63 and differentiating with respect to x leads to

$$\gamma'' \equiv \partial_x^2 \gamma = \frac{1}{\lambda_m^2} \frac{j_{\mathrm{zn}}}{j_c} + \frac{1}{\lambda_k^2} \frac{2\, j_{\mathrm{zn}} - j_{\mathrm{zn\text{-}1}} - j_{\mathrm{zn+1}}}{j_c} \tag{2.65}$$

where the length

$$\lambda_m^2 = \frac{\Phi_0}{2\pi\, j_c\, \mu_0\, t_{\mathrm{eff}}} \tag{2.66}$$

and

$$\lambda_k^2 = \frac{\Phi_0 d_{\text{eff}}}{2\pi\, j_c\, \mu_0\, \lambda_L^2} \tag{2.67}$$

The effective thickness of the tunneling contacts is $t_{\text{eff}} = t + 2\lambda_L \tanh(d/2\lambda_L)$ and of the electrodes is $d_{\text{eff}} = 2\lambda_L \sinh(d/2\lambda_L)$. The z-axis currents $j_{\text{z,n}}$ are given by the sum of Josephson, Ohmic, and displacement currents, which may be expressed as

$$j_{\text{z,n}} = j_c \sin\gamma_n + \sigma E_{\text{z,n}} + \epsilon\epsilon_0 \dot{E}_{\text{z,n}} = j_c \sin\gamma_n + \sigma \frac{\Phi_0}{2\pi\, t_{\text{eff}}} \dot{\gamma}_n + \underbrace{\epsilon\epsilon_0 \frac{\Phi_0}{2\pi\, t_{\text{eff}}}}_{1/\omega_{\text{pl}}^2} \ddot{\gamma}_n \tag{2.68}$$

Here σ is the electric conductivity, ϵ is the permittivity, and $E_{\text{z,n}}$ is the electric field component in the z-direction across the n-th barrier.
Bias currents are introduced by

$$j_{\text{z,0}} = j_{\text{z,N+1}} = j_{\text{ext}} \tag{2.69}$$

Additional boundary conditions are

$$\gamma_n'(x=0) = \gamma_n'(x=b) = \frac{2\pi\, \mu_0\, t_{\text{eff}}}{\Phi_0} H_{\text{ext}} \tag{2.70}$$

Comparing the sine-Gordon equation of a single junction with equation 2.65 motivates the definition of the Josephson penetration depth for a system of inductively coupled junctions

$$\lambda_j \equiv \left[\frac{1}{\lambda_m^2} + \frac{2}{\lambda_k^2}\right]^{-1/2} \tag{2.71}$$

The dimensionless coupling parameter s is defined as

$$s \equiv \frac{\lambda_j^2}{\lambda_k^2} = \frac{\lambda_m^2}{\lambda_k^2 + 2\lambda_m^2} \tag{2.72}$$

For $d \gg \lambda_L$ t_{eff} approaches $t + 2\lambda_L$ and d_{eff} diverges. Hence, because of the divergence of λ_k, s is reduced to zero in the limit of weak coupling. In the limit of strong coupling ($d \ll \lambda_L$), d_{eff} approaches d and λ_k is reduced to zero. Therefore, s converges to 0.5.

λ_m can be identified as the screening length for small magnetic fields directed along y, while λ_k is the length-scale for a Josephson vortex in an individual junction of the stack (cf. [52]).
In order to write equation 2.65 in a more compact form, the vectors $\vec{\gamma} = (\gamma_1, \ldots, \gamma_N)$ and $\vec{j}_z = (j_{z1}, \ldots, j_{zN})$ are introduced. The boundary conditions 2.69 are considered by adding the external currents to the first and last column.

$$\vec{\gamma}'' = \mathbf{M}\frac{\vec{j}_z}{j_c} - \frac{1}{\lambda^2}(1, 0, \ldots, 0, 1)\frac{J_{\text{ext}}}{j_c} \tag{2.73}$$

or, equivalently,

$$\vec{\gamma}'' - \frac{1}{\lambda_m^2}\frac{j_{\text{ext}}}{j_c} \cdot \mathbf{1} = \mathbf{M}\,\frac{\vec{j}_z - \vec{j}_{\text{ext}}}{j_c} \tag{2.74}$$

with $\mathbf{1} = (1, \ldots, 1)$. The matrix elements $M_{i,k}$ of the matrix $\mathbf{M}$ are given by $M_{i,i} = \lambda_j^{-2}$, $M_{i,i+1} = M_{i-1,i} = -\lambda_k^{-2}$ and $M_{i,k} = 0$ otherwise.

2.9.2. Plasma oscillations in a stack of inductively coupled Josephson Junctions

In order to describe the dynamics of oscillations in γ_n with small amplitudes A_n a plane wave approximation can be used [76]:

$$\vec{\gamma}''(x,t) = \vec{A}\exp[i(kx - \omega t)] \tag{2.75}$$

With a linearized sine-function, zero external current, and no damping equation 2.74 is reduced to

$$\mathbf{M}\,\vec{A} = \frac{k^2}{\left(\frac{\omega}{\omega_{\text{pl}}}\right)^2 - 1}\vec{A} \tag{2.76}$$

The eigenvalues of the matrix $\mathbf{M}$ are

$$\frac{1}{\lambda_j^2}\left[1 - 2s\cos\left(\frac{n\pi}{N+1}\right)\right], \quad n = 1, 2, \ldots, N \tag{2.77}$$

with the corresponding eigenvectors

$$\left(\vec{A}_n\right)_i = \sqrt{\frac{2}{N+1}}\sin\left(\frac{in\pi}{N+1}\right), \quad n = 1, 2, \ldots, N \tag{2.78}$$

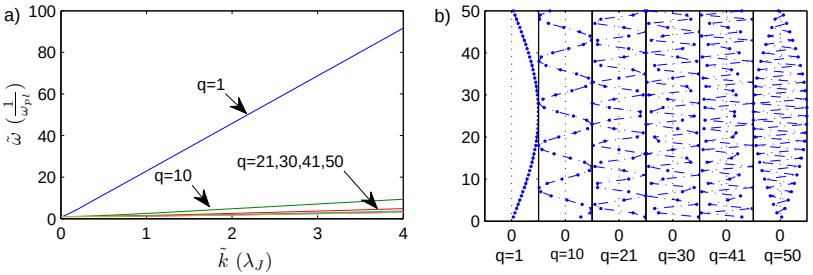

Figure 2.8.: Plasma wave approximation in a stack of inductively coupled Josephson Junctions: a) Dispersion relation of different plasma modes denoted with q in units of the Josephson penetration depth λ_J and the inverse of the plasma frequency $1/\omega_{\mathrm{pl}}$. The lowest mode q=1 has the highest mode velocity. b) Electric field amplitude in the individual layers for different plasma modes. For the lowest mode (q=1), the field amplitude has the same sign in all the layers, while for all the other modes there is always a sign change. The most extreme case is the highest mode (q=50). Here, the sign in neighboring layers is different.

This results in the dispersion relation

$$\omega = \omega_{\mathrm{pl}} + \frac{\omega_{\mathrm{pl}}^2 \lambda_j^2 k^2}{1 - 2s\cos\left[n\pi/(N+1)\right]}, \quad n = 1, 2, \ldots, N \tag{2.79}$$

Hence, in a stack of N, inductively coupled Josephson Junctions plasma waves with N different modes can be excited. The mode velocity c_n of the plasma wave n is

$$c_n = \frac{\omega_{\mathrm{pl}} \lambda_j}{\sqrt{1 - 2s\cos\left[n\pi/(N+1)\right]}}, \quad n = 1, 2, \ldots, N \tag{2.80}$$

2.9.3. The π-kink state

In section 2.8.2 it was demonstrated that the Josephson oscillation does not necessarily couple to the plasma modes. For that reason, it is quite remarkable that, by numerical calculation, the existence of a dynamical state in stacks of strong inductively coupled Josephson Junctions was discovered, which provides a coupling mechanism between the plasma modes and the Josephson oscillations even in a zero magnetic field environment [50, 59, 54, 42].
The principal characteristic of this state is an in c-axis periodic assembly of π-kinks in the order parameter, which is stabilized by an in c-axis uniform plasma wave. This state could cause coherent super radiation with a fundamental frequency determined by the Josephson relation. Such a π-kink state is a peculiarity of inductively coupled stacks of Josephson Junctions and there exists no analogy in a single Josephson Junction.

2.10. Intrinsic Josephson Junction in $Bi_2Sr_2CaCu_2O_8$

2.10.1. Properties of $Bi_2Sr_2CaCu_2O_8$

The high-temperature superconductor $Bi_2Sr_2CaCu_2O_8$ has the typical layered perovskite crystal structure (figure 2.9 a), [98]). CuO_2 double layers alternate with SrO and Bi_2O_3 layers (figure 2.9 a)).

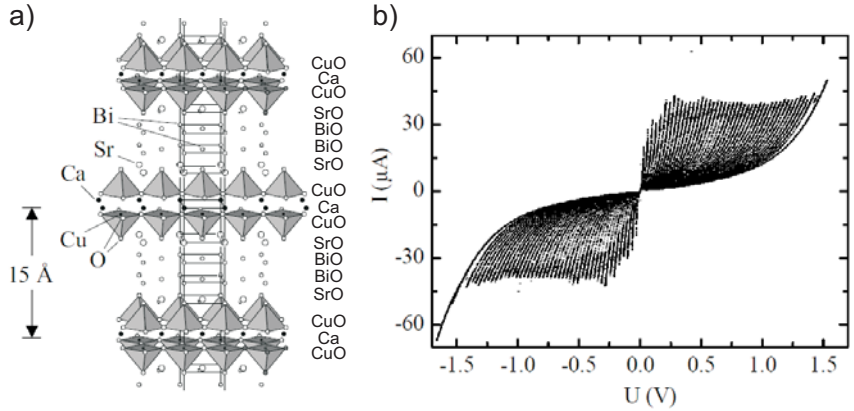

Figure 2.9.: a) Crystal structure of $Bi_2Sr_2CaCu_2O_8$ [65] b) IV-curves of a $2 \times 2\,\mu m$ $Bi_2Sr_2CaCu_2O_8$ -mesa at 4.2 K showing the characteristic branch structure [39]

While the CuO_2 layers carry the superconducting wave function, the insulating SrO/Bi_2O_3 layers serve as a reservoir for charge carriers. With an optimal stoichiometry, $Bi_2Sr_2CaCu_2O_8$ is electrically insulating. But $Bi_2Sr_2CaCu_2O_{8-\delta}$ becomes conductive for reduced oxygen concentration, because charge carriers (holes) are injected in the CuO_2 layer. These holes condensate into a superconducting state below the critical temperature T_c. The highest T_c is achieved with $\delta_0 \approx 0.16$ [1, 97].
The layered structure of $Bi_2Sr_2CaCu_2O_8$ causes extremely anisotropic behavior: The resistivity at room temperature in the ab-plane is approximately $100\,\mu\Omega$cm, while the resistivity along the c-axis is a few Ωcm. For underdoped crystals, ρ_c increases with decreased temperature, leading to a ratio ρ_c/ρ_{ab} of up to 10^5. Because there is a significant phonon contribution, the anisotropy of the thermal conductivity κ is much smaller ($\kappa_{ab}/\kappa_c \approx 6$) [18]. For low temperatures, the London penetration depth $\lambda_{ab} \approx 200 - 300\,\text{nm}$ and $\lambda_c \approx 100\,\mu$m [104]. Measurements of the critical field reveal that the Ginzburg-Landau coherence length $\xi_{ab} \approx 23\,\text{Å}$ and $\xi_c < 1\,\text{Å}$ [67].

2.10.2. The intrinsic Josephson effect

A small coherence length in c-direction ξ_c indicates that the superconductivity is confined to the CuO_2 double layers. Although these layers are separated by insulating SrO/BiO, they are electronically coupled. The discovery of the ac- and dc-Josephson effect revealed that a $Bi_2Sr_2CaCu_2O_8$ single crystal forms a stack of natural (intrinsic) planar Josephson Junctions [53]. As depicted in figure 2.9, the distance between two CuO_2 double layers of 15 nm implies a junction number of 660 for a crystal with a height of 1 μm.
The Stewart-McCumber parameter of the Josephson Junctions depends on the doping level (lower damping for underdoped crystal) and on the temperature. The hysteresis in the current-voltage relation and the fact that the junctions in the stack are connected in series is the reason for the characteristic IV-behavior of underdamped crystals, cf. figure 2.9 b). If the c-axis current is increased from zero above the critical current I_c, only a small number (ideally only one) junction switches into the resistive McCumber state. Because the junction is hysteretic, this causes a jump in the IV-curve. Immediately after this jump, the current is reduced to zero. This way, the first branch in the IV-curve is recorded. Now the current is increased up to the second jump and the current is reduced to zero again causing the next branch which bends at higher voltages. This procedure is repeated until all junctions are in the resistive state leading to the characteristic branch structure.

2.10.3. Self heating in $Bi_2Sr_2CaCu_2O_8$ stacks

$Bi_2Sr_2CaCu_2O_8$, like all high T_c superconductors, is a bad thermal conductor. Because of the high power density deposited in a BSCCO stack with junctions in the resistive state, significant self-heating can be expected. This is confirmed by the two experiments and the simulation briefly discussed in the following.
Fenton et al. have investigated the current-voltage characteristic of $(30\mu m)^2$ mesas with square wave current pulses [26]. Because the pulse height was chosen above the critical current of the individual junctions, all junctions were driven into the resistive state. They have varied the pulse height and recorded the voltage response with a 100 MHz digital storage oscilloscope. From these data, the current-voltage characteristics (IVCs) for

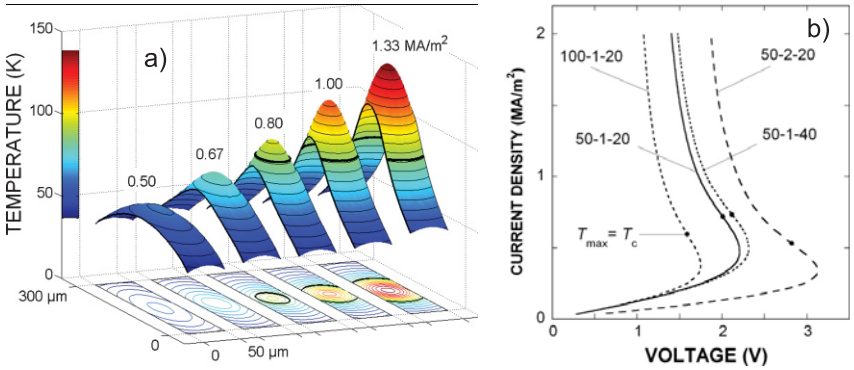

Figure 2.10.: Self heating in BSCCO-mesa calculated using "Comsol Multiphysics": a) The temperature distribution in a 50 μm wide mesa at different current densities and a base temperature $T_0 = 10$ K. The contour lines are drawn for every 5 K. $T = T_c$ is marked by the thick lines. b) Calculated IVC at $T_0 = 10$ K. The triple numbers indicate the mesa width, the mesa height, and the thickness of the underlying single crystal (in μm). The dots mark the I-V points where $T_{max} = T_c$. The solid line corresponds to the temperature distributions in a). From A. Yurgens, Phys. Rev. B **83**, 184501 (2011), Ref. [116]; © 2011 American Physical Society.

a certain time delay after biasing have been extracted. At a delay of 50 ns, a reduction of the resistance is evident and indicates a significant heating of the sample. For delays above 10 μs, the IVCs show a S-shaped IV characteristic resembling the IVCs presented in chapter 4. At a base temperature of 33 K, the mesa temperature for delays longer than 10 μs was estimated to be above the critical temperature of $Bi_2Sr_2CaCu_2O_8$ for high-bias currents.
Wang et al. have fabricated a mesa with a lateral size of a few microns [107]. By choosing an in-line geometry the influence on the measurement due to the Joule heating created by the contact resistance was avoided. In the middle of the mesa, an electrode with a height of 100 nm was defined, dividing the stack in a top and a bottom stack of 55 junctions each. With the help of the middle electrode, it was possible to bias both stacks independently. By making use of the temperature dependence of the critical current, the top stack was utilized as a temperature sensor. This way the self-heating in the bottom stack was investigated. Again the IVC showed the S-shaped characteristics for high-bias currents. For a bath temperature of 4.2 K, a maximum mesa temperature of 85 K was detected. An influence on the critical current and temperature measurement, respectively, can be excluded, because the middle electrode was significantly thicker than the c-axis quasiparticle relaxation length of approximately 16 nm estimated in [114].
A. Yurgens calculated the temperature distribution in a large BSCCO mesa using the finite element analysis software environment "Comsol Multiphysics", cf. Ref. [116]. Great care was taken in order to make the model as realistic as possible. For an increase in bias current, the simulation reveals, that the maximum mesa temperature increases considerable due to self heating, and that the temperature distribution becomes more and more non uniform with the maximum in the center of the mesa due to the strongest cooling at the edges, cf. figure 2.10 a). Note, that the maximum temperature exceeds the critical temperature T_c for high currents. The calculated IVCs show again the characteristic back bending ("knee"), cf. figure 2.10 b).
Both experiments and the simulation demonstrate the influence of self-heating on the IVC even for small mesas. For high-bias currents, the self-heating can be so strong that the mesa is heated above the critical temperature of $Bi_2Sr_2CaCu_2O_8$.

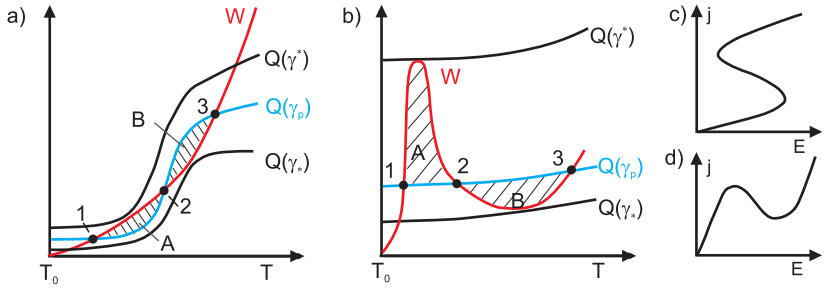

Figure 2.11.: Heat balance between Joule self-heating and heat-transfer power. The thermal bistabilty is caused by a) an abrupt change in the resistivity or b) an N-shaped temperature dependence of the heat-transfer power. [38] c) S-shaped and d) N-shaped current-voltage characteristics. [101]

2.11. Thermal bistability in electric conductors

The S-shaped current-voltage characteristics mentioned in the preceding section 2.10.3 is an indication for thermal bistability, which is discussed in the following. If the heat balance condition between the Joule self-heating $Q(T, \gamma)$ and the specific heat-transfer power $W(T)$ from the sample to the coolant holds for more than one temperature [38], an electrical system is thermally bistable.

$$Q(T, \gamma) = W(T) \tag{2.81}$$

This situation occurs if either the resistivity changes abruptly with temperature, cf. 2.11 a), or if the temperature dependence of the heat-transfer power from the sample to the coolant is N-shaped, cf. 2.11 b). In the following only the first case is considered. γ is the control parameter of the Joule heating and corresponds either to the current density j or the electric field strength E depending on the sign of the resistivity change. If the resistivity increases with temperature, the appropriate control parameter is the current density and $Q(T, j) = \rho(T)\, j^2$, otherwise the appropriate control parameter is the electric field strength and $Q(T, E) = \frac{E^2}{\rho(T)}$.
In [101] Volkov et al. distinguish between thermally bistable systems with N-shaped and S-shaped current-voltage characteristics (IVC), cf. figures

2.11 c) and d). By considering the voltage drop, it is easy to see that an abrupt increase of the resistivity corresponds to an N-shaped IVC, while a decrease corresponds to an S-shaped IVC.
There are many examples for thermally bistable systems and only a small selection is given in the following: The Gunn-effect in a "two valley" semiconductor [101] and the self-heating hot spot in a superconducting thin film micro bridge [87] are examples for bistable systems with N-shaped IVC, while the thermal break-down in a plate-shaped negative temperature coefficient thermistor [88] causes thermal bistabilty in a system with S-shaped IVC.
According to figure 2.11 a) there are three equilibrium points for a bias in the interval $\gamma_* < \gamma < \gamma^*$. Investigating the dynamic equation (where ν denotes the specific heat)

$$\nu\, \partial_t T = Q(T, \gamma) - W(T) \tag{2.82}$$

with a small temperature perturbation $\delta T \propto \exp(\lambda t)$ the stability criterion

$$\partial_T W > \partial_T Q \tag{2.83}$$

can be obtained [38]. Hence, at point 2 the system is meta-stable and the IVC is hysteretic in the interval $\gamma_* < \gamma < \gamma^*$.

2.11.1. Electro-thermal domains

In an extended conductor, the thermal bistabilty can cause the formation of electro-thermal domains. These are areas that have a significantly higher temperature and either a higher electric field strength (for $\gamma = j$) or a higher current densitiy (for $\gamma = E$) than the rest of the conductor.
A simple model is given in [88]: Consider a plate-shaped negative temperature coefficient thermistor (NTC) that is mounted with good thermal and electric contact between two conducting pins, cf. figure 2.12 a). The temperature dependence of the resistivity creates an S-shaped IVC for a homogeneous temperature distribution in the NTC. In a "Gedankenexperiment" the NTC is divided into two parts and the system is replaced by an equivalent thermal and electric circuit that is a parallel circuit of two NTCs with similar IVC, cf. figure 2.12 b). A_1/A_2 and A_{12} denote

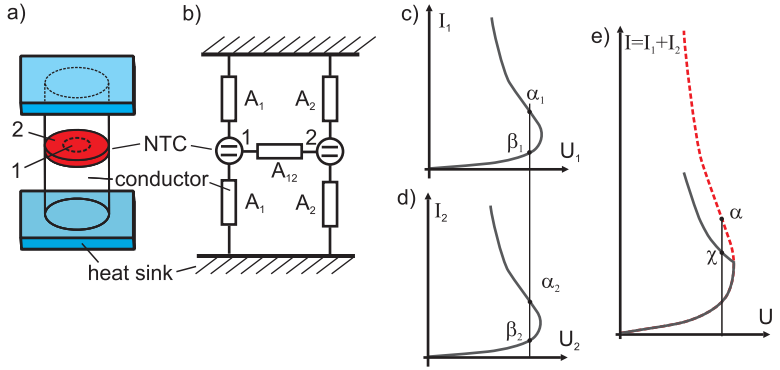

Figure 2.12.: a) Negative temperature coefficient thermistor (NTC) mounted between two conducting pins; b) Equivalent thermal circuit; c) and d) IVC corresponding to NTC-1 and NTC-2 in the equivalent circuit; e) IVC of the parallel circuit with thermal branching. (From Ref. [88])

the thermal coupling coefficients between the pins and the NTCs, respectively.
First, the case of two thermally decoupled NTCs is discussed ($A_{12} = 0$). If the voltage is increased, both parts of the NTC enter the current interval with negative differential resistivity simultaneously. In figure 2.12 c) and d) a bias point with negative differential resistance is denoted with α_1 and α_2, respectively. α denotes the corresponding bias point for the whole device in figure 2.12 e). The meta-stable state of two conductors with negative differential resistance in parallel is stabilized if one of those conductors switches into the β-state with positive differential resistance and lower temperature (point χ in the total IVC). This creates a branching in the IVC of the device, cf. figure 2.12 e).
In the case of thermal coupling between the two parts of the NTC ($A_{12} > 0$), it is possible to show that the point of branching is shifted to higher currents for increasing A_{12} [89]. That is plausible because a strong thermal coupling works against an inhomogeneous temperature distribution.

Another way to motivate the existence of electro-thermal domains is

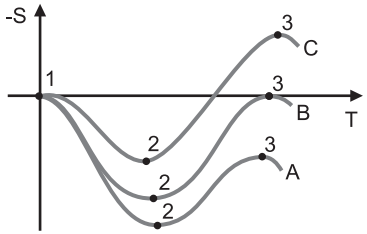

Figure 2.13.: Sketch of the potential -S for A, $j < j_P$; B, $j = j_P$; and C, $j > j_P$. 1, 2, and 3 denote the temperatures of the equilibrium points in figure 2.11 a).

to consider thermal switching waves in a quasi one-dimensional bistable conductor [38, 10, 101], e.g. a micro bridge in a superconducting thin film. Such a system is described by the non-linear heat-conduction equation

$$[\nu(T) + G\delta(T - T_c)]\,\partial_t T = \partial_x\left(\kappa(T)\,\partial_x T\right) + Q(T) - W(T) \qquad (2.84)$$

ν is the heat capacity, κ the thermal conductivity, and G is the latent heat of the phase transition associated with the thermal bistability. For the sake of simplicity, it is assumed that $G = 0$ and κ constant in T.
In order to acquire the solution in an infinitely long conductor, the propagating heat distribution $T = T(x - vt)$ with the velocity v is inserted into equation 2.84

$$\kappa\,\partial_x^2 T + \nu v\,\partial_x T + Q - W = 0 \qquad (2.85)$$

If x is identified with the time and T with the position, equation 2.85 corresponds to the equation of motion of a particle with the mass κ, under the friction νv and the force $Q - W$. Only solutions $T(x,t)$ that approach a constant value for $x \to \pm\infty$ are physically relevant

$$\lim_{x\to-\infty} T(x,t) = T_a \qquad \lim_{x\to\infty} T(x,t) = T_e \qquad (2.86)$$

Equation 2.85 is multiplied with $\partial_x T$ and integrated from $-\infty$ to x

$$\underbrace{\left[\frac{1}{2}\kappa(\partial_x T)\right]_{T_a}^{T(x)}}_{\text{kinetic energy}} + \underbrace{\int_{-\infty}^{x} \nu v(\partial x T)^2 dx}_{\text{friction}} - \underbrace{\int_{T_a}^{T(x)} (W - Q)dT}_{\text{potential}} = 0 \qquad (2.87)$$

The first term corresponds to the kinetic energy of a particle of mass κ that moves in a potential $-S = \int_{T_a}^{T}(W - Q)dT$ under a friction that is proportional to the velocity v of the thermal switching wave.

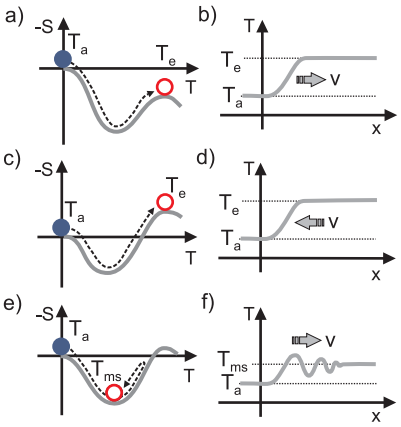

Figure 2.14.: Thermal switching waves: The time coordinate of the motion on the left side corresponds to the spatial x-coordinate on the right side. The filled blue circles mark the starting points, while unfilled red circles mark the stopping points. a) and b) solitonic switching waves with positive velocity. c) and d) with negative velocity. e) and f) shockwave in a conductor switching from the meta-stable state with temperature $T_{ms} = T_e$ into a stable state with temperature T_a.

The shape of the potential S depends on the control parameter γ, which, is in the case of a micro bridge, the current density j. By considering figure 2.11 a) the dependence of S on the current density can be understood easily, cf. figure 2.13. Note that for $j = j_p$ the areas A and B in figure 2.11 are the same size.

According to equation 2.87 the problem can be solved by considering the motion of a ball in the potential $-S$. The boundary conditions 2.86 are only met for a motion sequence, where the ball starts at an equilibrium point of the potential $-S$ with an infinitesimally small velocity and finally stops at an equilibrium point.

First, solutions where the heat distribution propagates with a finite velocity v are discussed. A motion sequence of a ball starting at one maximum and stopping at another maximum corresponds to a solitonic wave, where the conductor switches from one stable state into another, cf. figure 2.14 a)-d). The sign of the friction term in equation 2.87 determines the propagation direction of the wave. A ball starting at a maxium and stopping at the minimum of the potential corresponds to a shockwave where the conductor switches from the meta stable state into a stable state, cf. figure 2.14 e)-f). Note that the sign of the friction term has to be positive in this case, otherwise the ball would escape. Hence, the conductor always switches into a stable state.

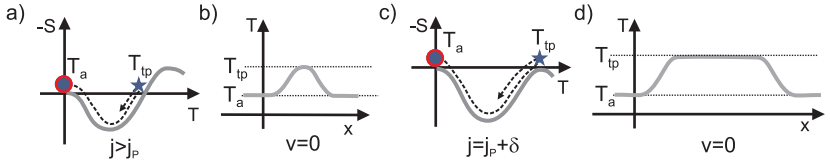

Figure 2.15.: Stationary temperature distributions in an infinitely long micro bridge: The starting points are identical with the stopping points. The turning points are marked with a blue star. a) and b) spatially confined temperature fluctuation. c) and d) spatially extended electro-thermal domain.

Stationary ($v = 0$) heat distributions are discussed in the following. Because the velocity is zero, the friction term in equation 2.87 vanishes. One solution corresponds to a motion sequence of a ball starting at one maximum and stopping at another, cf. figure 2.14 a)-d). Due to conservation of energy, the maxima have to be at the same level in this case. This implies $j = j_P$. Such a heat distribution can be regarded as a "frozen" solitonic switching wave.
Another category of solutions corresponds to a ball starting at one maximum of $-S$ changing its direction of motion at a turning point, and returning to its origin, finally, cf. figure 2.15 a) and b). This usually results in a spatially confined heat distribution. In the special case of a small δ with $j = j_P + \delta$ and $\delta > 0$, the ball stays at the turning point for quite a long time. The resulting heat distribution can be considered as an extended electro-thermal domain, cf. figure 2.15 c) and d). The smaller the δ, the longer the ball stays at the turning point and consequently the wider the electro-thermal domain in the micro bridge is. Because the existence of a electro-thermal domain implies $j \approx j_p$ in this model, the IVC is horizontal while an electro-thermal domain exists. Note that the temperature of the (hot) electro-thermal domain is approximately the equilibrium temperature T_3.

The switching process in an extended bistable electric conductor is similar to the phase transition in thermodynamics. This is elucidated in the following by comparing the switching process in a superconducting micro bridge with the isothermal compression of van der Waal gas in a piston.

The voltage across the bridge corresponds to the volume of the gas and the current density to the pressure, respectively. First, the bridge is superconducting. The current is increased to a point where the bridge enters into the flux-flow state. This leads to a voltage drop. If the voltage across the bridge is increased further, the system enters the bias interval of thermal bistability between the superconducting and normal conducting state. As a consequence, an electro-thermal domain (i.e., a hot spot) emerges. According to the preceding paragraph, the current density is approximately j_p. This is comparable to a point where the van der Waal gas starts to condens. An increase of voltage enlarges the electro-thermal domain, while the current stays at j_p as the pressure in the piston stays constant during phase transition. At the point where the whole bridge becomes normal conducting, the system is leaving the bias interval of bistabilty. This corresponds to a situation where all the gas in the piston is liquefied.

To summarize this section: Thermal bistability in an extended conductor with N-shaped IVC can cause the formation of electro-thermal domains in which the electric field density is increased. In this case the electro-thermal domain walls are always perpendicular the direction of the electric current.[3] The existence of an electro-thermal domain is associated with an almost horizontal section in the IVC. On the contrary, in an extended conductor with S-shaped IVC the electric current density is increased in the electro-thermal domains and the electric current flows parallel to the domain walls. Hence, the electro-thermal domains are pinches or hot spots in the conductor. A vertical section in the IVC indicates the existence of an electro-thermal domain in this case.

[3] Hence, the so-called hot spot in a superconducting micro bridge is in fact a hot layer.

3. Experimental techniques

3.1. Sample preparation

First, it should be said that the author was not involved in the sample preparation and that all samples investigated in the course of this thesis have been fabricated by Huabing Wang and his colleagues. For that reason, this section is restricted to what is absolutely necessary.
The single crystals were grown by floating zone technique in a four-lamp arc imaging furnace. They were annealed at a temperature between $600 - 650\,°\mathrm{C}$ in an Ar 99 %, O_2 1 % atmosphere for 48-72 h. The crystals were slightly underdoped with a T_c of approximately 83-87 K. The single crystals were glued on a sapphire or Si substrate with polyimide and were cleaved using an adhesive tape in order to obtain a flat surface. The final cleaving step was performed in a vacuum atmosphere and subsequently a several 10 nm thick Au thin film was evaporated in situ. This way, any oxidation of the freshly cleaved surface is avoided and good electrical contact is ensured. The mesa structure was defined using photolithography and Ar-ion milling. It is important to note that due to the Ar-ion milling, the flanks of the mesa do not have an angle of 90 ° to the crystal surface but were shallow leading to a trapezoidal cross-section of the mesa [70, 34]. Part of the base crystal and one edge of the mesa was covered with polyimide to isolate the top electrode. Then an Au-wire with a diameter of 50 μm was glued on the polyimide surface and a conducting path was drawn to the top of the mesa with silver paste. An additional Au-wire was connected to the part of the crystal pedestal, wich was not covered with polyimide, as a bottom (ground) electrode.

3.2. The low-temperature scanning laser microscope (LTSLM) set-up

Motivated by the successful research with the low-temperature scanning electron microscope (LTSEM) at the Physiklisches Institut in Tübingen, M. Peschka started to develop a low-temperature scanning laser microscope (LTSLM) as part of his doctoral thesis [75]. Subsequently, it was tested and improved by several diploma students [27, 64, 84, 103]. The biggest advantage of the scanning laser microscope over the scanning electron microscope is that the sample under investigation can be situated in a high magnetic field. Therefore, the original plan was to integrate the microscope in a 5 T superconducting magnet with an out-of-plane field direction, but, because of the modular concept, the microscope can also be used in a low field configuration, which was used for the experiments during this thesis. Another advantage of the LTSLM set-up with respect to the low-temperature electron-scanning microscope set-up is the usage of a LHe continuous-flow cryostat, which allows choosing a sample temperature between 3.5-300 K at will. Therefore, this system is particularly suitable for investigating samples of high T_c superconductors when a sample temperature between the boiling temperature of LHe and LN_2 is necessary.
This section is organized as follows: Before the scanning laser microscope is described in detail, an overview of the set-up including the cryo-system is given. Then the imaging process of the microscope is explained. In the last subsection, transport measurements and imaging on BSCCO mesas are discussed.

3.2.1. Overview

The sample under investigation is vertically mounted in vacuum on the cold finger of a custom-made optical LHe continuous-flow cryostat from Janis Reasearch with sapphire windows in the vacuum isolation and IR-shielding, respectively (cf. figure 3.1). A Zeiss LD Achroplan 20x0,4 objective lens with correction collar (to keep the optical error caused by the sapphire windows at a minimum) is used.
The temperature of the sample is stabilized by a PID temperature controller (Lakeshore LS340) via the current through a heater loop and the

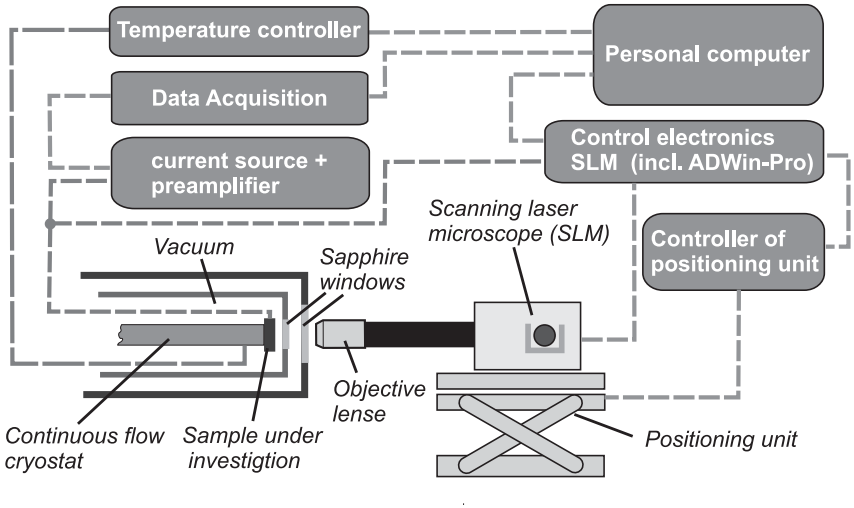

Figure 3.1.: Schematic diagram of the low-temperature scanning laser microscope set-up

temperature readout of a Cernox CX-1050-CU temperature sensor (not depicted). Without great effort, it is possible to keep the temperature fluctuation below 10 mK by choosing the appropriate PID values. A GPIB connection to a personal computer facilitates the remote control of the temperature controller by a Labview program.
For biasing the sample and measuring the voltage drop, a low noise-current source with a range $10\,\mu\mathrm{A} - 100\,\mathrm{mA}$ and a preamplifier with an amplification $10 - 10^4$ are available among others. By supplying these devices, which are realized as electronic modules, with a 20 V lead storage battery, they are galvanically isolated from the power grid. For a detailed description on the biasing circuit, refer to the following sections.
A National Instruments PCI-6259 AD/DA converter in combination with a BNC-2090 connector box is used for data acquisition and setting the output of the current source via a control voltage. This way a Labview program can be used for the transport measurements.
The control electronics of the scanning laser microscope consists of several devices, which are controlled by a real-time computer system ADWin-Pro,

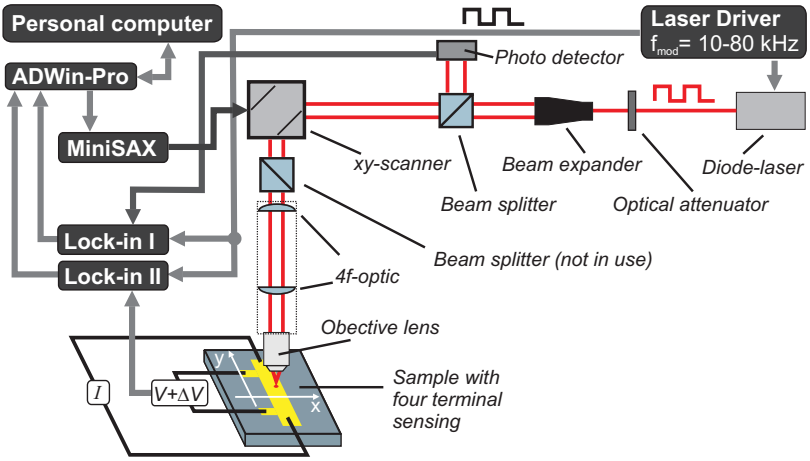

Figure 3.2.: Scheme of the low temperature scanning laser microscope (LTSLM). The sample is disproportionally enlarged for clarity.

which is connected to the personal computer via Ethernet. In section 3.2.2 the functional interaction of these devices is detailed.
Because the sample is fixed in the continuous-flow cryostat, a positioning unit for choosing the field of view and focusing is required. The controller of this positioning unit is connected to the ADWin-Pro system mentioned above.

3.2.2. The scanning laser microscope in detail

Figure 3.2 depicts the scheme of the LTSLM. A temperature-stabilized diode laser with a wavelength of 680 nm, a Gaussian beam diameter of 1.3 mm, and an output power of 25 mW are used. The amplitude of the laser is modulated via a TTL signal generated by the laser driver. The modulation frequency can be tuned between 10 kHz and 80 kHz. For some experiments, it is necessary to reduce the power of the laser beam. This is done by positioning an attenuator in the optical path.

In order to increase the diameter of the laser beam, a Galilean beam expander is used. This way, the entrance pupil of the objective lens is illuminated optimally. The laser beam passes a beam splitter and a scanning unit, which is composed of two galvano scanners (General Scanning-XY9.52T-S open frame scan head) for the x and y direction, respectively. A Keplerian telescope (4f-optic) is used to overcome the distance between the xy-scanner and the objective lens (Zeiss-LD-Achroplan 20x0,4 korr.), which has a large working distance of 12.4 mm and is corrected for the two sapphire windows in the optical cryostat (not depicted in the figure). The diffraction limited spot diameter of the laser probe on the sample would be about $0.85\,\mu m$. Due to the inadequate correction of the sapphire windows and the misalignment of the system, a diameter of $1.0 - 1.3\,\mu m$ is more realistic.
The proportion of light that is reflected back into the instrument is deflected via a beam splitter into a photo detector. The signal of the photo detector is analyzed by an analog lock-in amplifier (Princeton Applied Research Model 124A with a differential preamplifier Model 119) that supplies an output voltage proportional to the intensity reflected by the sample surface. A second lock-in amplifier (Standard Research SR830DSP) is used to filter out the response ΔV to the heating of the laser spot on the sample. The laser driver supplies a reference signal to both lock-in amplifiers, which is synchronous to the amplitude modulation of the laser beam.
Both lock-in amplifiers transmit their output signals to an AD converter module (AIN-F4/14 SP) in the ADWin-Pro system, which is connected to a personal computer via an Ethernet-cross-cable. An additional DA converter module (Aout14/16) in the ADWin-Pro-system provides the signals for setting the x and y position of the laser beam on the sample to the MiniSAX controller of the two galvano scanning-mirrors. The imaging process is controlled by a program on the ADWin-Pro real-time computer, which is monitored by another program on the personal computer. Confer to [37, 84] for an elaborate description of the computer system including the programs.

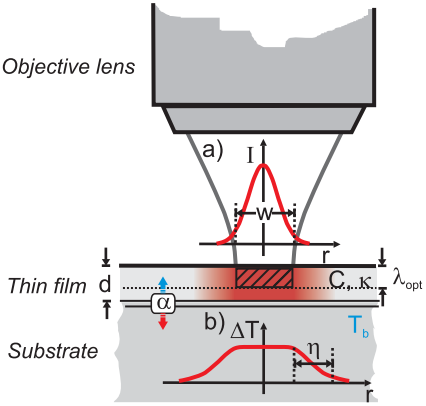

Figure 3.3.: Model of a LTSLM probe on a thin film with thickness d according to [17]. λ_{opt} is the optical penetration depth. C and κ are the heat capacity and thermal conductance of the thin film material, respectively. α denotes the heat-transfer coefficient. Graph a) depicts the lateral intensity distribution of the laser spot with a diameter w, while graph b) is the lateral heat distribution in the thin film with a thermal healing length η.

3.2.3. The principle of low-temperature scanning laser microscopy

While in the preceding subsection the individual components of the LTSLM are discussed, the focus in this subsection is on the working principle, and particularly on the response mechanism leading to the so-called voltage image.

The samples under investigation are usually thin film structures, which are in many cases superconducting. A good thermal coupling between the sample and the cold finger is necessary for the voltage imaging, as will be explained in the following. In all cases, a transport measurement in either a four terminal or a two terminal sensing configuration is applied. Usually, the samples are not specially prepared for the LTSLM, but are transferred to the LTSLM set-up for further analysis.

By mapping the response of the photo detector (cf. figure 3.2 and subsection 3.2.2) an optical image is acquired that is comparable to the images taken by a conventional optical microscope with a numerical aperture of 0.4 and a monochromatic light source. This optical image is most useful for relating the sample geometry to the voltage image.

In the following, the interaction of the laser beam with the sample is illustrated by a simple example (cf. figure 3.3). If a laser beam is focused on the surface of a metallic thin film that is thicker than the optical pen-

etration depth λ_{opt}, a proportion of the light intensity is absorbed, while the rest is reflected. Clem et al.[17] have discussed a similar scenario for the interaction of an electron beam with a thin film sample. Because the exact mechanism of the energy transfer from the microscope probe to the sample does not matter, this model can be adopted. A substrate with a high thermal conductance and good coupling to the cold finger is assumed, leading to an almost homogenous temperature distribution in the substrate with an average equal to the temperature T_b of the cold finger. The lateral heat distribution in the thin film is governed by the heat-transfer coefficient of the substrate/thin film interface and the thermal conductance of the thin film. In this model, the thermal healing length is given by $\eta = (\kappa d/\alpha)^{1/2}$ and the thermal response time is $\tau_\alpha = Cd/\alpha$. The maximum temperature rise depends on the power deposited P_0 and is $\Delta T_{\max} \approx P_0/\kappa d$. Realistic values for the thermal healing length are a few μm , for the maximum temperature rise a few K, and for the response time a few 10 μs. Concerning more complex samples, in most cases it is still safe to assume that an amplitude modulated laser beam with a modulation frequency between 10 kHz and 80 kHz creates a localized heat distribution with a diameter of a few μm that almost instantaneously follows the modulation.

The amplitude modulated heat distribution influences the four-terminal sensing of the transport measurement, causing a response ΔV that is measured by lock-in technique (cf. figure 3.2). This response depends on the position of the laser probe. By scanning the laser probe over the sample and mapping the output signal of the lock-in amplifier, which is proportional to ΔV, a voltage image is acquired.

The response mechanism depends on the characteristics of the sample. If for instance the resistivity of a TMR-element defined by a grain boundary has different temperature dependence for different relative magnetization direction between the electrodes, it is possible to image the magnetic state of the TMR-element [103].

It is not always necessary to apply a current in order to detect a voltage response ΔV. In certain samples, the laser probe is inducing a local current source due to the Seebeck effect, which causes a voltage drop between the voltage taps of the four-wire sensing [64]. [1]

[1] At first glance, it seems somewhat counterintuitive that a localized current source in a conducting thin film causes a voltage drop between two voltage taps that

Because a far-reaching understanding of the system under investigation is necessary in order to explain the response mechanism, the interpretation of the voltage images can be quite challenging. Sometimes it is helpful to refer to older experiments with the LTSLM or LTSEM, respectively, in order to interpret certain features.
Despite the difficulties, LTSLM is a powerful tool to acquire the lateral characteristics of certain electronic properties of a sample.

3.2.4. Investigation of BSCCO mesas with the LTSLM set-up

If a current source is used for biasing a BSCCO-mesa, it is difficult to trace the complete branch structure. For instance, confer to figure 2.9 b: Some of the outer branches have a smaller critical current I_c as the inner ones. Hence, these branches cannot be accessed. The complete branch structure can be traced by using a voltage source instead of a current source. Because the resistance of the mesa decreases for high-bias currents ("back-bending" of the IVC), this could cause overheating and at worst the destruction of the sample. In order to protect the sample, a resistor with a resistance approximately equal to the high-bias resistance of the sample should be connected in series.
Alternatively, a current source can be used with a resistor in parallel (cf. figure 3.4). This way, the output impedance of the current source is reduced, the load line of the mesa becomes diagonal, and consequently all branches can be accessed. In the LTSLM set-up a potentiometer is used as a parallel resistor to adjust the load line. In order to determine the current across the sample, a measuring resistor of 10 Ω is used. Both pre-amplifiers are connected to the input channels of the data acquisition system, cf. figure 3.1. In addition, an output channel of the data acquisition system provides a control voltage for the current source. With the help of a Labview program a current-voltage curve (IVC) of the mesa can be recorded. As explained in section 3.2.3, the heat distribution of the laser probe is crucial for the response and the resolution of the voltage

are a considerable distance away. But by applying the reciprocity theorem for electrical circuits, i.e., replacing the voltage measurement with an imaginary current source and the localized current source with an imaginary voltage probe, it is quite plausible that a voltage drop can be detected in the vicinity of the laser probe position.

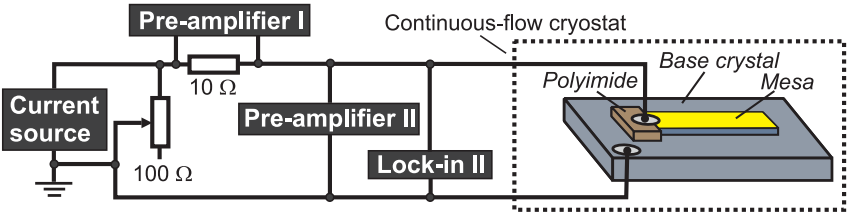

Figure 3.4.: Transport measurement on a BSCCO mesa with two-terminal sensing. The impedance of the current source is reduced by a 100 Ω potentiometer. In order to read out the current across the sample with pre-amplifier I, a 10 Ω resistor is used. The voltage drop across the mesa is measured by pre-amplifier II and lock-in II.

image. In BSCCO both the electrical and thermal conductivity are highly anisotropic and thus the resulting temperature distribution should be calculated explicitly.
The laser probe in BSCCO was investigated with a simple COMSOL-Multiphysics model (figure 3.5). In the rotational symmetric model, a disc with a diameter of 20 and a thickness of 1 micron was defined. In order to simulate BSCCO, the values of $\kappa_{\mathrm{ab}} = 4\frac{\mathrm{W}}{\mathrm{m\,K}}$ and $\kappa_c = 0.5\frac{\mathrm{W}}{\mathrm{m\,K}}$ from [18] were used for the horizontal and vertical thermal conductivity. On top of the BSCCO layer a 60 nm-thick gold layer was constructed. The laser spot was simulated by a boundary on the gold layer that corresponds to a disk with a diameter of 2 microns. For the energy flow through that boundary, a value was chosen that corresponds to a total power of 250 μW. This is a good approximation because the thickness of the gold layer is larger than the optical penetration depth. Therefore, less than 10 % of the laser intensity is absorbed by the gold layer. Additionaly, in order to take account for the reflections at the beam splitters and at other components in the optical path of the scanning laser microscope, it can be assumed that only 10 % of the laser intensity is reaching the sample. For the bottom of the BSCCO disk, a fixed temperature of 50 K was chosen as the boundary value in order to simulate the cold finger.
As can be seen, the temperature distribution is confined and the maximum temperature rise at the surface is about 5 K, decaying to half of

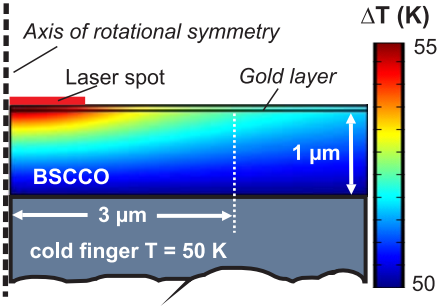

Figure 3.5.: COMSOL Multiphysics simulation of the laser probe in BSCCO. The thickness of the gold layer is 60 nm and the diameter of the laser spot 2 μm. It is assumed that a power of 250 μW is deposited in the gold layer.

this value at a distance of 2.5 μm (giving a resolution of the LTSLM images of about 5 μm). In c-direction the temperature rise has decreased to 50 % about 0.5 μm away from the surface. It should be noted that the maximum temperature rise of the heat distribution is proportional to the power of the laser spot.

3.3. LTSLM/LTSEM imaging

In this section, two examples are discussed in which certain characteristics of the electric state have been imaged via LTSEM/LTSLM technique. Both examples are helpful for the interpretation of the LTSLM images of intrinsic Josephson Junctions in large BSCCO mesas that are presented in chapter 4.

3.3.1. Cavity modes and fluxon dynamics in planar Josephson junctions

Cavity modes and soliton dynamics in planar Josephson Junctions (e.g. $Nb/Al_2O_3/Nb$) have been imaged via LTSEM- and LTSLM technique. By analyzing the response of the perturbed sine-Gordon equation on a beam-induced local thermal distribution, Lachenmann et al. developed a theory on the imaging mechanism in a LTSEM [55].
For a long Josephson Junction with in-line geometry, the perturbed sine-

Gordon equation[2] (cf. section 2.5.2) is given by

$$\phi_{\mathrm{xx}} - \phi_{\mathrm{tt}} - \sin\phi = \alpha\phi_t - \beta\phi_{\mathrm{xxt}} \tag{3.1}$$

with boundary conditions

$$\phi_x(0,t) + \beta\phi_{\mathrm{xt}}(0,t) = -\kappa + \eta \tag{3.2}$$

$$\phi_x(L,t) + \beta\phi_{\mathrm{xt}}(L,t) = \kappa + \eta \tag{3.3}$$

Here $\eta = H_y/J_0\lambda_J$ is the external magnetic field and $\kappa = I_B/2J_0w\lambda_J$ takes into account the bias current. H_y is the magnetic field component along the short side of the junction, J_0 is the critical current density, λ_J is the Josephson penetration depth, I_B is the external bias current, and w is the width of the junction.
The temporal change of the total energy is given by (cf. appendix A.1)

$$\begin{aligned}\frac{dH}{dt} = &\int_0^L dx\, \left[-\alpha\phi_t^2 - \beta\phi_{\mathrm{xt}}^2\right] \\ &+ \eta\left(\phi_t(L) - \phi_t(0)\right) + \kappa\left(\phi_t(L) + \phi_t(0)\right)\end{aligned} \tag{3.4}$$

The local heating of the tunnel junction generated by the electron beam irradiation at position x_0 creates a local increment $\Delta\alpha(x_0)$ and $\Delta\beta(x_0)$ of the damping coefficients α and β, respectively. Assuming that the increment of the damping parameter is independent of the position for homogeneous junctions, the time-averaged beam-induced power loss in a linear approximation is, according to equation 3.4,

$$\left\langle \frac{d\Delta H}{dt} \right\rangle = -\Delta\alpha\left\langle \phi_t^2 \right\rangle - \Delta\beta\left\langle \phi_{\mathrm{xt}}^2 \right\rangle \tag{3.5}$$

For a constant bias current I_B this leads to a voltage response

$$\Delta V(x_0) \propto -\Delta\alpha\left\langle \left[\phi_t(x_0)\right]^2 \right\rangle - \Delta\beta\left\langle \left[\phi_{\mathrm{xt}}(x_0)\right]^2 \right\rangle \tag{3.6}$$

Therefore, the contribution of $\Delta\alpha$ and $\Delta\beta$ to the voltage signal are modulated by the time average of the square of the local electric field $\left\langle \left[\phi_t(x_0)\right]^2 \right\rangle$ and of the square of the local time derivative of the magnetic field $\left\langle \left[\phi_{\mathrm{xt}}(x_0)\right]^2 \right\rangle$

[2] The indices denote partial derivatives.

in the junction, respectively.
If the junction dimension is small with respect to λ_J, the dynamics is governed by its electromagnetic cavity modes.
LTSEM voltage images of cavity modes at Fiske or zero field resonances in Nb/Al2O3/Nb junctions reveal that for these types of junctions mainly the magnetic field creates a response [61]. It seems that the change in the damping parameter β dominates. Because the response is proportional to the square of the time derivative of the magnetic field, the wavelength of the wave pattern has to be doubled in order to deduce the wave length of the cavity mode.
In [61] the LTSEM voltage images of the cavity modes were interpreted similarly as above. It was assumed that the local heating caused by the electron beam influences the quality factor (Q-factor) of the cavity, which is given by $Q^{-1} = Q_s^{-1} + Q_p^{-1}+$, where Q_s describes the surface loss and Q_p the loss due to quasi particle tunneling, respectively. If the electron beam is on a position of an anti-node of the cavity mode, a large response can be expected, while if the electron beam is at a node there is no response.
For junctions with dimensions larger than λ_j, the dynamic is described by the movement of solitons. It is possible to image this state via LTSLM/LTSEM, because the slowdown of the solutions in vicinity of the local heat distribution creates a change in the voltage drop over the junction, cf. [55, 13].

3.3.2. Hot-spot in a superconducting bridge

Self-heating hot spots in superconducting thin film micro bridges (as discussed in section 2.11.1) have been imaged via LTSEM technique [23, 20]. In [22] the theory of the imaging mechanism is discussed in detail. If the position of the heat distribution generated by the electron beam is on the normal conducting domain of the micro bridge (position A in figure 3.6 a)), the heat distribution changes the resistivity in its vicinity. In the case of a micro bridge that is wider than the lateral diameter of the heat distribution (a few microns), the voltage response of the four-terminal sensing is very small, because the region with changed resistivity is shunted by the rest of the bridge. If the electron beam is at the superconducting domain (position B in figure 3.6 a)) and if, in addition, a beam intensity is chosen for which the maximum temperature change in the heat distribution is

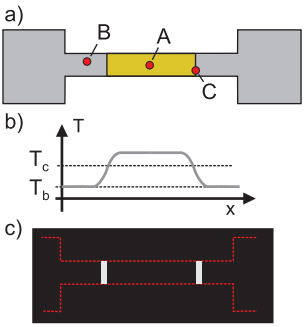

Figure 3.6.: a) Scheme of a superconducting micro bridge with a hot spot. A: electron beam on the normal conducting domain; B: on the superconducting domain; and C: on the hot spot edge. b) Temperature distribution in the micro bridge. T_b is the base temperature and T_c the critical temperature of the superconductor. c) Sketch of an LTSEM image. The red dashed lines indicate the edge of the micro bridge for clarity.

smaller than the difference between the critical temperature of the superconductor T_c and the base temperature T_b (cf. figure 3.6 b)), the electron beam does not influence the transport measurement at all and the voltage response is zero. Only for a position where the electron beam is at the edge of the hot spot is the response significantly increased (position C in figure 3.6 a)). In this case, the energy deposited by the electron beam increases the size of the hot spot and consequently changes the resistance of the micro bridge. The LTSEM voltage image resembles two vertical stripes, which indicate the edge of the hot spot (cf. figure 3.6 c).

3.4. Detection of coherent THz-radiation

3.4.1. Introduction

There are different methods to detect electromagnetic radiation in the THz range: One way is to measure Shapiro steps in the current-voltage relation of a detector Josephson junction and to determine the frequency by the voltage difference cf. 2.8.1. This was tried in the course of this thesis with specially prepared samples consisting of a large main mesa surrounded by small detector mesas, but without success. Another method is to downmix the signal in a heterodyne receiver [5]. Because the mixing frequency should be in the range of the detected signal, one should have a rough idea of the expected frequency in advance.
Using optical interferometry to determine the frequency is a method which delivers undisputable results over a wide frequency range. But the design

of optical systems is challenging because beam splitters and lenses exhibit strong dispersion at wavelengths of 100-300 μm. Usually Mylar- and wire-grid beam splitter are used. In Eisele et al. [24] a simple and compact but powerful design of a far-infrared Fourier-transform spectrometer was presented. The system works as a Michelson interferometer, but the use of conventional beam splitters and lenses is avoided. The main feature of this instrument is a lamellar split mirror, which combines the role of a beam splitter and the element that causes the phase difference in the interferometer. The optical components used show no dispersion, are polarization insensitive, and are not subject to vibrational noise. In addition, no power is reflected back into the sample under investigation.
Eisele et al. have suggested using either a pyroelectric or a Golay cell detector. Both methods were tried, but it turned out that the power radiated by the BSCCO mesa is so weak that the use of He-cooled bolometer is necessary for good results.
The interferometer described was first built at the National Institute of Material Science in Japan. On the basis of the experience gained, first steps were taken to realize a similar set-up at the Physiklisches Institut in Tübingen.

3.4.2. An interferometer for the detection of THz radiation

In this section the interferometer set-up is described in detail, cf. figure 3.2.1. The sample under investigation is mounted in LHe continuous-flow cryostat Janis Research (modified ST-100) with polyethylene windows in the vacuum shroud and an aperture in the IR shielding that is minimized with an aluminum foil in order to reduce the heat load of the sample. The temperature control of the cryostat is identical as described in section 3.2.1. The sample is in the focus of a 90° off-axis parabolic mirror with gold coating, a focal length of 100 mm, and a diameter of 2 inches. A moveable split mirror divides the signal into two groups of beams with a phase delay defined by the translation stage, cf. figure 3.8. The mirror is made from brass and is gold coated. Both halves have six lamellas each with a height of 5 mm. A second parabolic mirror with identical properties as the one already mentioned reflects the beams in an optical He-cryostat with a polyethylene window. The electromagnetic radiation is collected by a Winston cone (an optical antenna) and detected by a

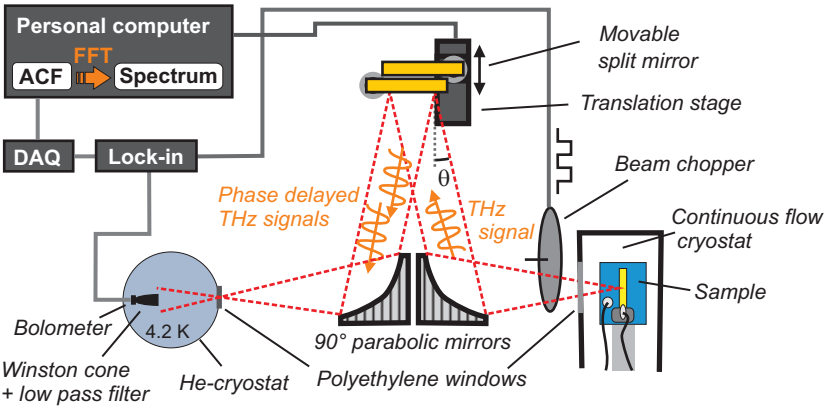

Figure 3.7.: Setup for the detection of coherent THz-radiation.

bolometer at a temperature of 4.2 K. In front of the Winston cone is a low-pass filter with a cut-off frequency of 1 THz. Please note that the focus of the second parabolic mirror is on the window of the cryostat instead of the aperture of the Winston cone. This mistake reduces the solid angle of detection to about 0.04 sr. In order to lower the noise of the bolometer system caused by 1/f-noise, the beam is amplitude-modulated by a chopper with a frequency of 13 Hz and lock-in technique is used. By recording the bolometer signal with respect to the mirror displacement, the auto correlation function is acquired, which is mapped into a spectrum using fast-Fourier transformation (FFT). The frequency resolution of the interferometer depends on the maximum displacement of the split mirror $\Delta f = c/(2d_{\max}\, cos\theta)$, where θ is the angle of incidence of the beam and $\cos\theta \approx 0.998$. The maximum displacement of the translation stage is 25 mm, leading to a theoretical frequency resolution of $\Delta f \approx 6\,GHz$.
Because the emitter is mounted on the coldfinger of a continuous flow cryostat the alignment of the system is challenging. If the emitter is out of focus the divergence of the beam introduces an additional optical path difference, which reduces the modulation in the autocorrelation function, and consequently results in a line broadening ([33] chap. 1, sec. VII). This can easily deteriorate the frequency resolution to about 15 Ghz.
If the auto correlation function is modulated over the complete range, the

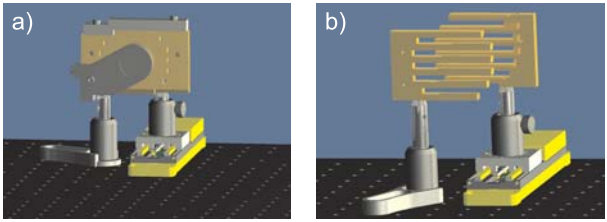

Figure 3.8.: Autodesk-Inventor images of the lamellar split mirror on a translation stage (Thorlabs MTS25/M-Z8) a) during assembly: Both halves of the mirror are aligned with a removable holder (horizontal bar at the top). In front of the mirror a holder for the adjustment mirror is attached. b) during operation

minimum coherence length of the signal is given by $l_c = 2d_{\max}\, cos\theta \approx 50\,\text{mm}$ and the coherence time is given by $t_c = c/l_c \approx 1.6 \cdot 10^{-10}$ s. It should be noted that the coherence length and coherence time of a narrow bandwidth thermal light source is $l_c = 3\,\text{m}$ and $t_c = 10^{-8}$ s, respectively [113]. Hence, the requirements on the coherence of the signal for interferometry are not very high and, consequently, it is not evidence for a highly coherent signal, if it is possible to record an auto correlation function.
The split mirror can be considered as a single lamellar grating, which in addition to the phase delay between the mirror halves causes diffraction [93]. As a consequence, the modulation in the auto correlation function caused by the interference of the zero order diffraction maxima is superposed by interference patterns of higher order with the same modulation frequency, but shifted by 90 degrees. This could cause artifacts in the spectrum like an additional peak at double frequency. In order to prevent these artifacts, a horizontal slit in front of the detector can be used to cut off first-order diffraction beams [24]. It was refrained from using a slit aperture because such a system is more difficult to align.
This set-up can also be used to detect the emitted power of the sample under investigation. For this purpose, the split mirror is brought into zero position and the bolometer signal is read out.

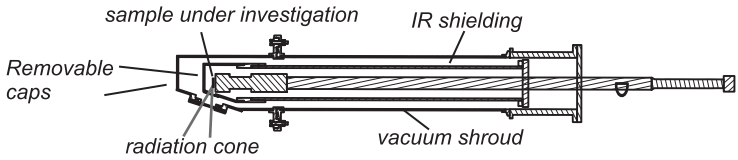

Figure 3.9.: Modified continuous flow cryostat for a THz-interferometer

3.4.3. A modified continuous-flow cryostat

Originally, a set-up was planned in which it was possible to detect THz radiation and to make LTSLM images simultaneously. Because of the small working distance of the LTSLM ($w_d \approx 13mm$), it is impossible to design a cryostat, which provides an optical window in front and a second window for THz radiation at the side of the sample. Alternatively, a modified vacuum shroud and IR shielding were designed with a window at the side of the sample only (cf. figure 3.9) for a THz interferometer. The idea is to use the continuous-flow cryostat in the LTSLM set-up as usual for the imaging and then to warm up the cryostat and to move the cold finger into the new vacuum shroud without demounting the sample. Therefore, the experimental conditions are almost identical in both set-ups except for the IR radiation caused by the different window configuration. Both, the vacuum shroud and the IR shielding are equipped with removable caps. This way, it is possible to position the sample mounted on the cold finger in the focus of the parabolic mirror with the help of a pilot beam.

3.4.4. An optical He-cryostat for a bolometer

For the realization of an interferometer set-up at the Physikalisches Institut in Tübingen, a suitable detector was needed. Because the emission power of the BSCCO emitter was expected to be small, a highly sensitive LHe-cooled bolometer would be the first choice. The costs for such a system including the necessary cryostat would have been to high. Therefore, it was decided to build an optical cryostat and to send it to the supplier (QMC Instruments LTD.) for installation of a bolometer including Winston cone and low-pass filters.
The following requirements for this cryostat were defined: a hold time of LHe of 12 h at minimum, sufficient space to mount the bolometer including

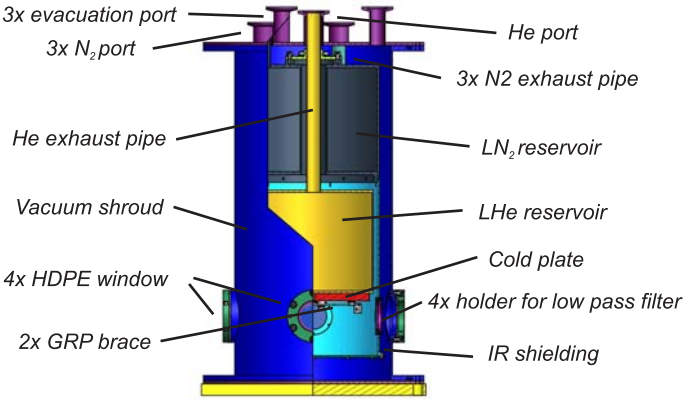

Figure 3.10.: An optical cryostat for a bolometer

the Winston cone on a cold plate, an HDPE window, which allows optical access, and the possibility to mount a low-pass filter in the IR shielding. In addition the design should keep vibrational noise, e.g., caused by boiling coolant, as low as possible.
For cooling the IR shielding, a design with an LN_2 reservoir was chosen, cf. figure 3.10. This reservoir is equipped with three exhaust pipes that are welded to the ceiling of the vacuum shroud, giving the cryostat more stability than a configuration with one exhaust pipe only. Below the LN_2 reservoir is the LHe reservoir. The LN_2 reservoir has a hole through which the He exhaust pipe is connected to the ceiling. Both reservoirs are made of 1.4301 steel sheets. On a ring at the bottom of the LN_2-reservoir, the IR-shielding made of chrome-plated aluminum is mounted. The cold plate made of gold-plated copper is fixed to the bottom of the LHe-reservoir. Two glass-reinforced plastic (GRP) braces are connected to the IR shielding, providing additional stability. In the vacuum shroud and the IR shielding are four windows each, which can be sealed with an aluminum plate if they are not in use.
Because both reservoirs are non-detachably connected with the ceiling of the vacuum shroud, they form, together with the IR shielding, an assembly that is plugged into the vacuum shroud from the top and sealed with an O-ring. In order to provide easy access to the cold plate, the bottom

of the vacuum shroud and the IR shielding can be removed.
The volume of the reservoirs is 2 L each. The hold time of LHe during operation is 24 h at a minimum. The hold time of LN_2 is 10-12 h.
The cryostat has two minor flaws. First, it is recommended that during cool down the cryostat is still evacuated by a turbomolecluar pump, otherwise the vacuum is insufficient. Because a leak can be excluded, this might be caused by out-gassing of components inside (probably the GRP braces). Second, the exterior of the cryostat is noticeably below room temperature during operation. Together with the relative short hold time of LN_2, this is an indication of a high thermal load to the LN_2-reservoir, which is caused by the three relative short exhaust pipes and is a trade-off for the high mechanical stability.

4. Results & Discussion

Most of the results presented in this chapter have already been published in [106], [105] and [36].

4.1. Wave pattern at low bias

Before the LTSLM images of a $40 \times 330\,\mu m^2$ mesa are presented, the characteristics of the current-voltage curve (IVC) are discussed. The thickness of the mesa is approximately $1\,\mu m$, which corresponds to 670 junctions, and the cold finger temperature was about 25 K. Confer to figure 3.4 for the electronic circuit used for biasing.
The IVC was basically recorded by sweeping the current through the mesa from 0 mA to 35 mA and to 0 mA again, cf. figure 4.1 a). Starting from 0 mA (A) the first branch is almost perpendicular, because the contact resistance has been subtracted numerically. At 10 mA (B) resistance appears [1] and at 13 mA (C) there is a jump in the IVC (denote by a red arrow), which is caused by simultaneous switching of several junctions in the stack into the resistive state, cf. section 2.10.2. Three more jumps follow. The line from 10 mA and 1.1 V (D) to 7 mA and 1.6 V (E) is caused by many switching processes. The big jump to 15 mA and 1.2 V (F) is the result of the formation of a hot spot,cf. section 2.11.1 and 4.2.1. Due to Joule-heating in the mesa, the IVC is almost perpendicular for high-bias currents. The disappearance of the hot spot is resulting in a jump from 10 mA and 1.25 V (G) to 4 mA and 1.4 V (H) while reducing the current. Note that the IVC has been traced out by increasing the current again after this jump. For low-bias currents, the IVC seems to be a continuous line, but it consists of a series of little jumps caused by the switching of junctions from the resistive into the superconducting state.
Figure 4.1 b) depicts a section of the IVC. The scope is denoted by a small square in figure a). This segment of the IVC is just before a jump

[1] Probably caused by flux flow.

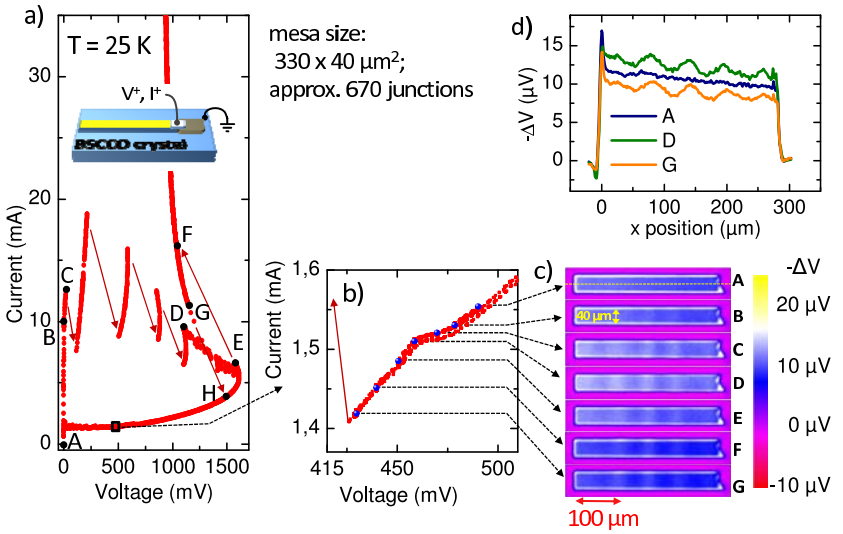

Figure 4.1.: LTSLM images of a BSCCO mesa in the low-bias (sub gap) regime: a) IVC, solid arrows denote jumps in the IVC; b) zoom in the IVC, blue dots symbolize bias points at which LTSLM images were recorded; c) series of LTSLM images; d) line scans extracted from the LTSLM images along the line symbolized by dashes in image G. From H.B. Wang, S. Guénon et al., Phys. Rev. Lett. **102**, 017006; © 2009 American Physical Society.

symbolized by the red arrow. The blue dots denote bias points, where LTSLM images have been recorded.
A series of seven LTSLM images is presented in figure 4.1 c). The shape of the mesa is recognizable in all images due to a strong signal at the edge. At the edge of the mesa, more energy of the laser spot is absorbed than inside, where the mesa is covered by a gold layer. In image A the LTSLM signal is homogeneous inside the mesa. Note that the negative sign of the response is consistent with the fact that the c-axis resistance of the mesa decreases with increasing temperature.
In the LTSLM images with lower-bias currents (B-G), a wave pattern appears that is modulated along the long side of the mesa. From images A,D, and G, line scans along a line denoted by dashes in image A have been extracted, cf. figure 4.1 d). The three images C-E were recorded at the little bump in the IVC. Although the amplitude of wave pattern stays constant, the background signal of these three images is increased.
Standing wave patterns in BSCCO stacks have been imaged in the past using LTSEM [14]. The response mechanism seems to be similar to the one of planar Josephson Junctions described in section 3.3.1. The local heating influences the damping and consequently the Q-factor of the junction stack. If the electron/laser beam is at a position of an anti-node of the cavity resonance, the response is strong. In contrast there is no response at the nodes. Because the intensity is imaged and not the field strength, the period of the standing wave pattern in the images is half of the wave-length of cavity mode.
With the help of the line scans in figure 4.1 d) a wave length $\lambda \approx 120\,\mu$m is deduced. Assuming that 60-70% of the junctions are in the resistive state, the average voltage per junction is $1 - 1.2$mV. Hence, using Josephson relation, a frequency $f = 0.5 - 0.6\,$THz and a mode velocity $c = (6-7)\times 10^7$m/s can be estimated. This is in agreement to the highest possible plasma mode velocity $c_0/n = 9 \times 10^7 \mathrm{m}/s$, where c_0 is the vacuum speed of light and $n \approx 3.5$ is the far infrared diffraction index [69] (cf. section 2.9.2 for a discussion of plasma modes in a stack of Josephson Junctions).
Finally, it should be emphasized that the bias interval is similar to the one in which Ozyuzer et al. detected coherent THz emission [69]. Unlike their assumption that the cavity mode is along the short side of the mesa, the imaged wave pattern is modulated along the long side of the mesa.

4.2. The formation of a electro-thermal domains at high bias

For high injection currents, where the IVCs show significant back bending ("knee of the IVC"), a characteristics feature appears in the LTSLM voltage images of the BSCCO mesas. The emergence of this feature is associated with a little kink or jump to lower voltages in the IVC. In this section it is explained that this LTSLM-feature is an electro thermal domain (i.e., a hot spot).
In the first subsection the LTSLM voltage images with the corresponding IVCs of two different BSCCO-mesas are presented. In the second subsection a special sample is discussed enabling monitoring the temperature distribution of the base crystal in the vicinity of the mesa for high bias currents. In the last subsection the self heating and the formation of electro-thermal domains is analyzed in a uniform temperature distribution model.

4.2.1. LTSLM voltage images of BSCCO-mesas at high bias currents

First the data of a $30 \times 330\,\mu\text{m}^2$-wide mesa are discussed, cf. figure 4.2. The base temperature is 50 K and the thickness of 1 μm corresponds to approximately 670 junctions. The current-voltage curve (IVC) of the mesa is similar to the IVC of the 40 μm-wide mesa in the preceding section 4.1. There are two major exceptions: First, the maximum voltage drop over the mesa is approximately half of the maximum voltage of the 40 μm mesa. Second, there is no big jump from the bias point of maximum voltage to the regime of high-bias currents (cf. figure 4.1 E to F) but there is a bending and a small jump at the bias of 610 mV and 16 mA marked by a black circle.
Confer to the inset in figure 4.2 a) for the sample geometry.
For low-bias currents the LTSLM-images resemble the image A in figure 4.2 b) i.e., no wave pattern appears in this bias regime. Above the bending in the IVC, a feature appears in the LTSLM-images at the right of the mesa, where the current is injected (image B). Note that the edge signal is increased at the right of the mesa and that there are two bright vertical stripes (marked by white arrows) at a distance of approximately 40 μm

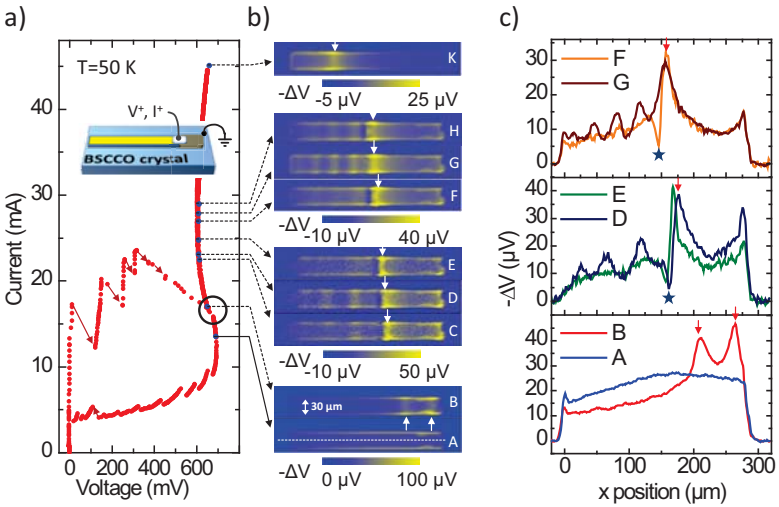

Figure 4.2.: LTSLM images of a 30 μm-wide mesa: a) IVC; dashed lines with arrow are pointing to the image recorded at the corresponding bias point; b) LTSLM-images (color bar is indicating the voltage response); c) Linescans extracted from the LTSLM-images. From H.B. Wang, S. Guénon et al., Phys. Rev. Lett. **102**, 017006; © 2009 American Physical Society.

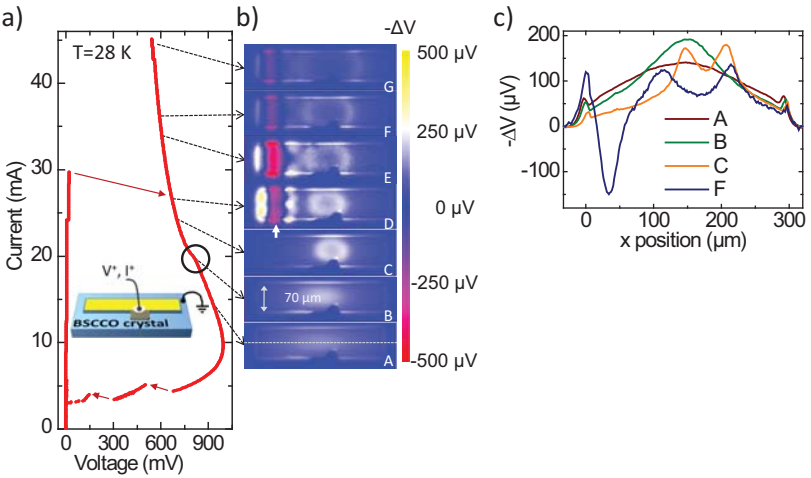

Figure 4.3.: LTSLM-images of a 70 μm-wide mesa: a) IVC; dashed lines with arrow are pointing to the image recorded at the corresponding bias point; b) LTSLM-images (color bar is indicating the voltage response); c) Linescans extracted from the LTSLM-images. From H.B. Wang, S. Guénon et al., Phys. Rev. Lett. **102**, 017006, (Supplemental Material); © 2009 American Physical Society.

and they have a slight convex bending. At higher-bias currents, only the left stripe remains (marked by a white arrow) and the feature grows for increasing bias currents (image C-H). For the highest bias current at 45 mA, almost three-fourths of the mesa are occupied by this feature (image K). In two bias intervals around 24 mA and 28 mA, respectively, a quasi one-dimensional standing wave pattern appears on the left of the mesa, cf. images C-E and images F-H.
In figure 4.2 c) line-scans extracted from the LTSLM-images are depicted. Confer to the white dashed line in image A for the path of the line-scans. Comparing line-scan B with line scan A reveals that while the signal is increased at the right, it is suppressed in the other part of the mesa.
The voltage response of the wave pattern is negative, as can be seen by comparing line-scan D with E, and G with F, respectively. Under the assumption that the wave pattern corresponds to a cavity mode, this would be consistent with the finding in [61] that the Fiske modes in planar Niobium Josephson Junction are causing a negative voltage response in LTSEM-images. In [61] the wave pattern of rectangular cavity modes has nodes at the edges of the junctions. Hence, the voltage response is proportional to the square of the magnetic field in this case. Because the amplitude of the wave pattern decreases at the left and it is not clear where the end of the cavity is at the right, cf. line-scans F and D, it is not possible to determine without a doubt if the square of the electric field or the magnetic field is imaged in the case of the 30 μm BSCCO mesa. Note the anti-peak in line-scans E, D, and F to the right of center marked by a blue star, which corresponds to a vertical dark stripe in the LTSLM images. It seems not to be correlated either to the wave pattern or the feature at the right, cf. line-scans B and G.
By applying an in plane magnetic field with a field strength that corresponds to approximately half of a flux quantum per junction it is possible to suppress the wave pattern at the left side, while the feature at the right is unaffected, cf. figure 4.4. This is a strong indication that the wave pattern is related to the phase dynamics in the Josephson Junctions stack. Note, that according to the line-scans in figure 4.4 the wave pattern has a node at the left edge.
Before the feature at the right in the LTSLM images of the 30 μm mesa is interpreted, the LTSLM-images of an additional sample shall be discussed, cf. figure 4.3. The size of the mesa was $70 \times 330\,\mu\text{m}^2$ and the base temperature was 28 K. Again the thickness was 1 μm. The IVC is

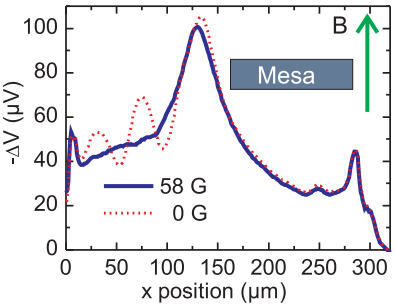

Figure 4.4.: LTSLM line-scan of the 30 × 330 μm-mesa (cf. figure 4.2) with an in plane magnetic field oriented along the short side of the mesa (blue solid line). For comparison, line-scan at the same bias in zero field (red dotted line). From H.B. Wang, S. Guénon et al., Phys. Rev. Lett. **102**, 017006, (Supplemental Material); © 2009 American Physical Society.

similar to the IVC of the 30 μm-mesa, except that there is only a bending and no jump at the bias point marked by the circle and that for high-bias currents, the IVC has a negative slope. The sketch of the sample geometry is depicted as an inset of the IVC. In this case, the top electrode was connected at the center of a long side of the mesa. A series of LTSLM images for high-bias currents, at different bias points has been recorded, cf. figure 4.3 b). The response in image A is homogeneous. The silver paste connecting the top electrode can be seen at the lower long side of the mesa. At a bias point right below the bending, the signal is stronger in the center of the mesa (image B). For higher bias points an elliptic ring appears, which becomes bigger for higher bias currents (image C-G). In image G the ring resembles two vertical lines with a slight convex bending similar to image B in figure 4.2 b).
Beside the ring on the left, a wave pattern appears (image D-G). Note the vertical red stripe marked by a white arrow in image D, which corresponds to a very strong positive voltage response. Confer also to the line-scan in figure 4.3 c). This strong positive response conflicts with the fact that for the 30 μm, sample the wave pattern was exclusively associated with a negative response, cf. figure 4.2 c). It is not clear if the strong positive response is part of the wave pattern or if it resembles the antipeak mentioned in connection with the line-scans of the 30 μm sample (cf. figure 4.2 c) line scans E, D, and F marked by a blue star.

Both the feature at the right in the LTSLM-images of the 30 μm mesa and the elliptic ring in the LTSLM-images of the 70 μm mesa, are caused

by electro-thermal domain walls (ETDW). The back-bending of the IVC in figure 4.2 and 4.3 indicates an S-shaped IVC and thermal bistabilty. According to section 2.11.1, thermal bistabilty might lead to the formation of electro-thermal domains and as consequence to the redistribution of the current density in the mesa, which is associated with a bending (thermal branching) in the IVC, cf. figure 2.12 e). The bias points marked by a black ring in the IVCs of figures 4.2 and 4.3 resemble precisely these points of thermal branching. The fact that the feature monotonously grows with increasing current and that the IVC is more or less vertical in the corresponding bias regime is consistent with the interpretation as an electro-thermal domain, cf. section 2.11.1.
Note, that in the following the electro-thermal domain with the high temperature is called a hot spot in order to use the same term as in the discussion of electro-thermal domains in superconducting micro bridges.
The voltage response of electro thermal domains in a BSCCO mesa during LTSLM-imaging is similar to the one described in section 3.3.2 in connection with the LTSEM-imaging of a hot spot in a superconducting micro bridge. The LTSLM voltage response of the laser probe within the limits of an electro-thermal domain is almost negligible. In the contrary, if the laser probe position is at an ETDW, it is shifting the ETDW and enlarging the domain with the high temperature. This results in a reduction of the mesa resistance and a negative LTSLM voltage response. According to figures 4.2 b) and 4.3 b), the LTSLM response of the domain wall decreases with increasing size of the domain with high temperature. By taking into account that the load line of the bias circuit is influenced by the size of the electro-thermal domains the reduction of the response can be explained. Confer to section A.2 for a theoretical investigation of the electro-thermal domain wall response in a simple model.

4.2.2. The formation of a hot spot monitored by detector stacks

A sample with a special design was used to monitor the temperature distribution in the vicinity of a large BSCCO mesa for high-bias currents. The main mesa with a size of $70 \times 330\,\mu\mathrm{m}^2$ is surrounded with a U-shaped mesa on which small stacks with a size of $(10\,\mu\mathrm{m})^2$ and a thickness corresponding to 15-20 junctions have been structured, cf. figure 4.5 b). The

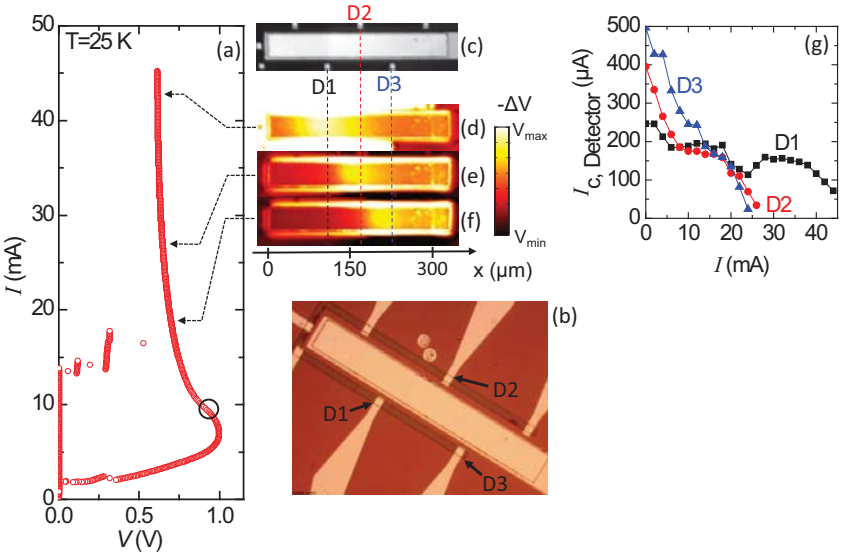

Figure 4.5.: The formation of a hot spot monitored by detector stacks: a) IVC at a base temperature of 25 K. The black dashed lines with an arrow denote the bias points at which the LTSLM images d)-f) were recorded. The point of thermal branching is marked by a black ring. b) Optical microscope image of the sample during fabrication. The main mesa is the large diagonal rectangle with its long sides running from the top left to the bottom right corner of the image. A U-shaped mesa surrounds the main mesa. Detector stacks were structured on the U-shaped mesa. The working ones are denoted with D1-D3. c) Optical LTSLM image recorded simultaneously with the LTSLM voltage images d)-f). For each of the three voltage images, a different color scale is chosen with V_{max} equals 100 μV, 200 μV and 320 μV for image d), e) and f). V_{min} was -50 μV for all three images. g) Critical current of the detector stacks vs. current through the main mesa. From S. Guénon et al., Phys. Rev. B **82**, 214506; © 2010 American Physical Society.

spacing between the main mesa and the U-shaped structure is 10 μm. Because of the small size of the structures, a vapor deposited gold layer was used for contacting the top layer of the mesas instead of silver paste. Confer to the diploma thesis of M. Grünzweig [34] for a detailed description on the sample fabrication. The main mesa has a thickness of only 0.5 μm because the resist that was used for e-beam lithography was limiting the depth for Ar-ion milling.
The original plan was to use this sample for detecting electromagnetic radiation from the main mesa by measuring Shapiro steps in the IVC of the small detector stacks. But the mesa did not radiate. Probably the junction number was too small. At the time this sample was investigated, the reason for the LTSLM feature discussed in section 4.2.1, that was identified as a hot spot, was under dispute. An alternative interpretation was that this feature is caused by the suppression of the superconducting gap via quasi particle injection. In order to resolve that question, the monotonic temperature dependence of the critical Josephson current of the detector stacks was utilized (in analogy to the experiment described in [107]) and the stacks surrounding the main mesa were used as temperature sensors. The size and the position of the electro-thermal domains were determined via the LTSLM-imaging, while the temperature distribution surrounding the mesa in the base crystal was monitored by the detector stacks.
The graph in figure 4.5 a) is the IVC of the main mesa at 25 K. The bias point of thermal branching is at approximately 8 mA. Figure 4.5 c) depicts an optical LTSLM image that was simultaneously recorded with the LTSLM voltage image d). This way, the position of the detector stacks with respect to the voltage image is documented. Only three detector stacks were intact, which are denoted by D1-D3. Figure 4.5 d)-f) is a series of LTSLM voltage images recorded at bias-points with high bias currents. The position of the detector stacks is indicated by dashed lines. At the right of the main mesa, a hot spot that resembles the quasi one dimensional one of the 30 μm mesa in figure 4.2 is clearly visible. The edge of the hot spot is moving to the left for higher bias currents.
For every individual detector stack, the IVC was recorded, while simultaneously the main mesa was biased with a certain current I. From these IVCs the critical current I_C was extracted and plotted in graph 4.5 g). Comparing graph g) with the LTSLM images d)-f) reveals that the critical current in the detector stacks is suppressed after the hot spot edge has

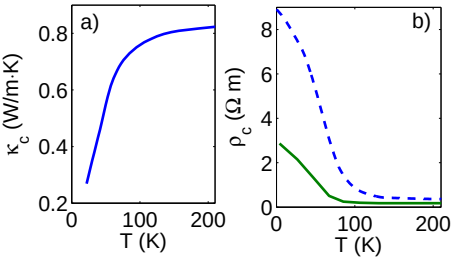

Figure 4.6.: a) c-axis thermal conductivity according to [18]. b) c-axis resistivity according to [57] (solid line) and according to [115] (dashed line).

passed the detector. Hence, the temperature in the base crystal is above the critical temperature of BSCCO in the vicinity of the hot spot.

4.2.3. The self heating and the formation of electro-thermal domains in a uniform temperature distribution model

In this section the current voltage characteristics of a $30 \times 330\,\mu\text{m}^2$-mesa is derived from the c-axis resistivity of BSCCO under the assumption that the temperature distribution in the mesa is uniform. In addition, the branching temperature is calculated according to E. Spenke [89]. By comparing these theoretical results with the data of section 4.2.1 strong evidence is provided that the kink in the IVC above the "knee" (marked by a black circle) is caused by thermal branching, i.e., by the formation of electro-thermal domains.
From Ohm's law $\frac{U}{R(\vartheta)} = I$ and Newton's law of cooling $U\,I = A(\vartheta)$, where $\vartheta \equiv T - T_b$ is the excess temperature of the base temperature T_b and $A(\vartheta)$ is the heat flow coefficient, the following relations can be derived easily

$$U = \sqrt{R(\vartheta)A(\vartheta)}; \quad I = \sqrt{\frac{A(\vartheta)}{R(\vartheta)}} \tag{4.1}$$

Hence, if the $R(\vartheta)$ and $A(\vartheta)$ are known, the IVC can be parameterized, cf. [12].
The dimensions of the narrow mesa described in section 4.2.1 are chosen. In order to keep calculations simple, a base crystal with the same lateral

dimensions as the mesa is assumed, cf. figure A.3. Note, in contrary to figure 2.10 in section 2.10.3, there is no edge cooling in this model. Therefore the assumption of a uniform temperature distribution is justified. The resistance and the heat flow coefficient can be calculated as

$$R(\vartheta) = \frac{H}{A}\rho_c(\vartheta); \quad A(\vartheta) = \frac{A}{L}\int_{T_b}^{T_b+\vartheta} dT\,\kappa_c(T) \tag{4.2}$$

In this section a mesa height $H = 1\,\mu$m, a mesa area $A = 30 \cdot 330\,\mu\text{m}^2$ and a base crystal height of $L = 20\,\mu$m is assumed.
A profound discussion of the temperature dependence of the electric resistivity $\rho_c(T)$ and the thermal conductivity $\kappa_c(T)$ in direction of the c-axis can be found in [115]. In this section the results of [18] are used for $\kappa_c(T)$ and it was extrapolated to lower temperature in order to cover the whole range of interest. The c-axis resistivity strongly depends on the doping level. In order to investigate the IVC, two different resistivity ρ_c vs. temperature T curves are used, cf. figure 4.6. The first one is based on transport measurements on a small mesa defined in a BSCCO-whisker, cf. [57]. The second one is the c-axis resistivity measured in a magnetic field of 6 T along the c-axis by Ozyuzer et al. (cf. supplement of [69]) and it is extrapolated according to [115].

In figure 4.7 the measured IVC at a base temperature $T_b = 50\,\text{K}$ of the $30 \times 330\,\mu\text{m}^2$-mesa discussed in section 4.2.1 is depicted together with the calculated IVCs for comparison. Both calculated curves show an almost vertical IVC for high currents resembling the measured one. Considering the maximum voltage at the "knee" of the IVC, it is smaller or considerable larger in the curve b) or c), respectively, as in the measured curve a). Note that the maximum temperature reached in curve c) is considerable larger than in curve b) indicating the strong influence of the c-axis resistivity on the self-heating. The curve c) is s-shaped, which is according to the discussion in section 2.11.1 a clear indication for thermal bistability.
Additionally, IVCs with a base temperature $T_b = 30\,\text{K}$ are depicted in figure 4.8. Again, the measured IVC a) shows a jump marked by a black circle indicating the formation of electro-thermal domains (point of thermal branching). In this case both calculated IVCs are s-shaped.
There are several possible reasons for the deviation of the calculated IVCs from the measured ones: The first reason is that most likely the c-axis resistivity ρ_c corresponding to the measured mesa is between the two depicted in figure 4.6 b). The second reason is that the base crystal height L

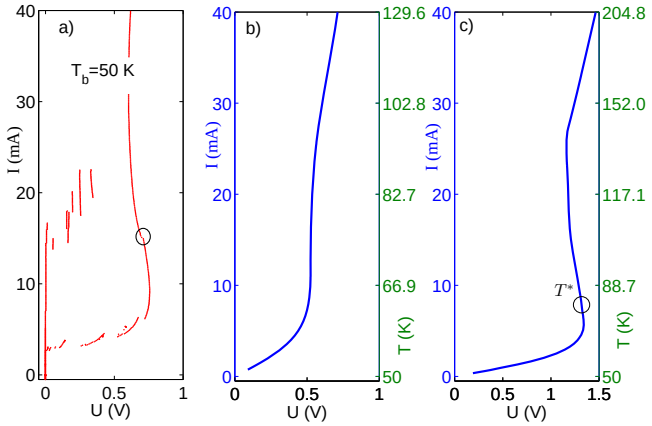

Figure 4.7.: a) IVC of the $30 \times 330\,\mu$m-mesa at a base temperature of $T_b = 50\,\mathrm{K}$. b) calculated IVC; ρ_c of [57] was used cf. figure 4.6. c) calculated IVC; ρ_c of [115] was used; the branching temperature $T^* = 81.7\,\mathrm{K}$.

is just a rough estimate. Note, that according to equation 4.1 and 4.2 the maximum voltage of the IVC scales with $\sqrt{\frac{H}{L}}$. The third reason is that even for such a narrow mesa the temperature distribution is not uniform. According to [60], edge cooling has a similar effect on the IVC as if a resistor is in parallel to the mesa tilting the IVC.

In order to discuss the formation of electro thermal domains in detail, a zoom in the IVC at 30 K (figure 4.8 b) is depicted in figure 4.9. Here, the s-shaped character is more pronounced and the interval with a negative differential resistance, which is associated with thermal bistability, can be seen clearly. Note, that the outermost bias point at the knee of the IVC, which corresponds to the temperature $\widetilde{T}$ is indicated by a red square . If the mesa is biased in the interval of negative differential resistance above a certain threshold temperature T^* (branching temperature) then the bias is stabilized if the mesa splits into two domains with different temperatures T_H and T_L, which both operate at a bias with positive differential resistance, cf. figure 4.9, figure 2.12. This results in a branching and an almost vertical dependence of the IVC for high currents. Note,

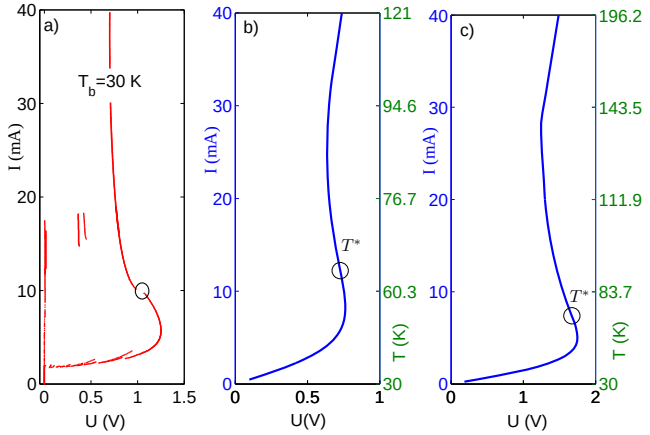

Figure 4.8.: a) IVC of the $30 \times 330\,\mu$m-mesa at a base temperature of $T_b = 30\,\mathrm{K}$. b) calculated IVC; ρ_c of [57] was used cf. figure 4.6; the branching temperature $T^* = 64.6\,\mathrm{K}$. c) calculated IVC, ρ_c of [115] was used; the branching temperature $T^* = 74.9\,\mathrm{K}$.

that this interpretation is a bit different to Spenke et al. [88], where a negative exponential temperature dependence of the resistivity is assumed and only the low temperature electro thermal domain operates at a bias with positive differential resistance, but it is in full agreement with the interpretation in more recent works [38, 101]. Confer to the measured IVC at a base temperature of 30 K (figure 4.8 a). The almost vertical IVC indicates the existence of electro-thermal domains from approximately 10 mA to above 40 mA. This is in contrary to the theoretical consideration in figure 4.9, where the electro-thermal domains only exists in a current interval of 11 mA and 25 mA. Again, the deviation can be explained by the unknown temperature dependence of the c-axis resistivity and the rough estimate of the base crystal thickness L.
The branching temperature is determined by the transverse thermal coupling that hinders the formation of electro thermal domains. In section A.3 a formula for the branching temperature was derived for this model following the consideration of Spenke [89]. With the help of this formula A.36, T^* was calculated for all the s-shaped theoretical curves depicted

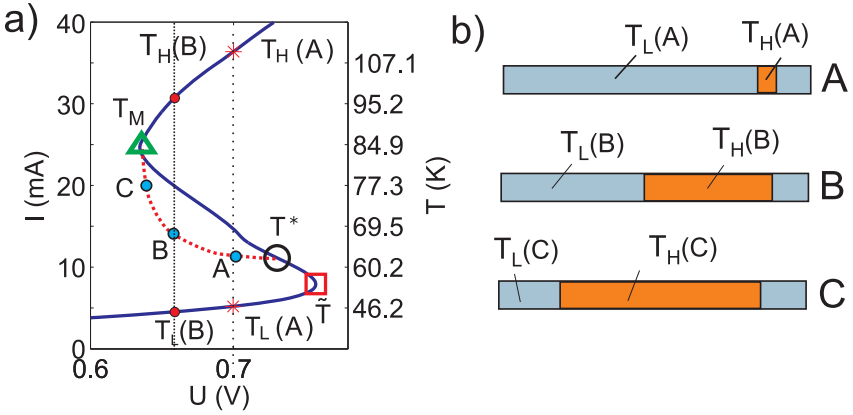

Figure 4.9.: The formation of electro-thermal domains: a) Zoom in the IVC of figure 4.8 b) (blue solid line); sketch of the IVC influenced by the formation of electro-thermal domains (red dashed line); $\widetilde{T}$ denoted with a red square and T_M denoted with a green triangle are the minimum and maximum temperatures of the interval of thermal bistabillity; the thermal bistabillity leads to the formation of electro-thermal domains above a certain threshold temperature T^* (branching temperature); at the bias point A the mesa is divided into electro-thermal domains at the temperatures $T_L(A)$ and $T_H(A)$, respectively; analog at the bias points B and C. b) Sketch of the electro-thermal domains in a narrow mesa corresponding to the bias points A,B and C in figure a).

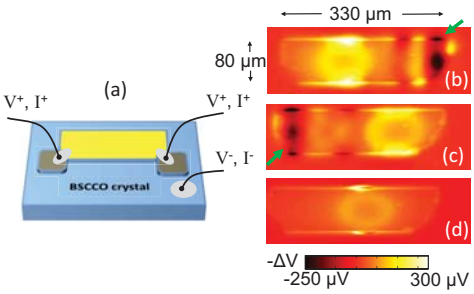

Figure 4.10.: Mesa with current leads at both sides: a) Sketch of the mesa b) LTSLM voltage image with current injection from left, c) from right, and d) from both sides. From S. Guénon et al., Phys. Rev. B **82**, 214506; © 2010 American Physical Society.

in this section and the position of the points of thermal branching were marked by black circles. A comparison with the kinks in the measured IVCs reveals that they are in good agreement.
Note, that in principle the branching temperature T^* can be above the critical temperature T_c of $Bi_2Sr_2CaCu_2O_8$. For instance, this might be the case for a disc shaped mesa, where the transversal thermal coupling, and consequently the branching temperature is higher as in the quasi one dimensional case, cf. also Ref. [88].

4.3. Changing the hot spot position and switching the wave pattern

A review of the LTSLM voltage images of the hot spot in the preceding sections reveals that the electro-thermal domain with higher temperature (hot spot) is usually located near the current injector of the top electrode. This is demonstrated by considering a $80 \times 330\,\mu m^2$-mesa: Two current leads are connected to the corners of the top electrode by silver paste, cf. figure 4.10 a). The LTSLM voltage images clearly reveal that the hot spot is positioned on the side from which the current is injected. For the case that the current is injected in equal parts from both sides, the hot spot stays in the center of the mesa.
Obviously, the hot spot position is determined by three competing effects: First, because the cooling is strongest at the edge of the mesa, the hot spot has the tendency to stay in the center. Second, the hot spot can be

considered as a drain for the in plane current of the mesa. Hence, if the current is injected from one side it is energetic favorable that the hot spot is shifted towards the current injector. Third, the contact resistance of the current leads generates Joule heating. This would favor a hot spot position directly under the current injector. The LTSLM voltage images reveal that the first two effects are dominating in this case, cf. figure 4.10 b-d.
Note the standing wave pattern beside the hot spot in figure 4.10, images b and c. There is a dark stripe corresponding to a strong positive response at the edge (marked by green arrows) like in the 70 μm-mesa of figure 4.3. Confer to the second part of section 4.5.1 (figure 4.14) for a discussion of this phenomenon.

4.4. The switching of the wave pattern in an arrow shaped mesa

In this section an arrow shaped mesa is discussed, cf. figure 4.11 a) for an optical image. This sample was originally fabricated together with a y-shaped mesa in order to investigate the wave splitting at the intersection. The current voltage curve (IVC) has a jump at a current of approximately 18 mA to higher voltages indicating the switching of a few junctions, cf figure 4.11 b). A series of LTSLM was acquired at different bias points. For high bias currents a considerable part of the arrow is surrounded by a dark line in the base crystal, which corresponds to a positive voltage response, cf. figure 4.11 c). For lower current, the line becomes clearer and its circumference is reduced, cf. figure 4.11 d). Note also, that this black line extends into the three branches of the arrow shaped mesa. This feature can be traced through the LTSLM images c-f and is denoted by blue arrows, cf. figure 4.11. The LTSLM voltage image at a bias slightly above the jump does not show a distinct edge signal corresponding to an electro-thermal domain as it is usually the case if a hot spot emerges, cf. figure 4.11 f).
A standing wave pattern appears in different parts of the arrow for different bias currents (image f-i). The bias interval, in which the image g-i was acquired, is above the "knee" of the IVC. Hence, self heating

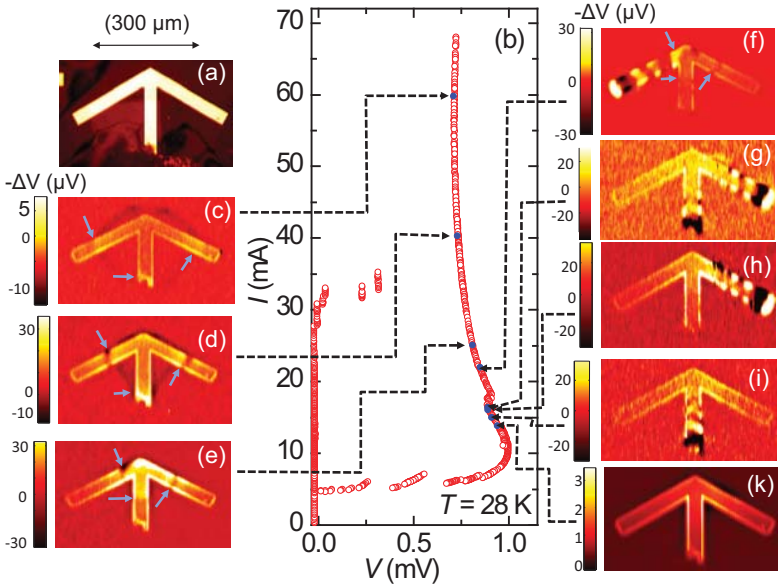

Figure 4.11.: The switching of a standing wave pattern in an arrow shaped mesa: a) optical image. b) current voltage curve (IVC). c)-k) LTSLM voltage images. The corresponding bias points are marked by red dots in the IVC and are indicated by dashed lines. The blue arrows denote the edge of the region that is above the critical temperature T_c. From S. Guénon et al., Phys. Rev. B **82**, 214506; © 2010 American Physical Society.

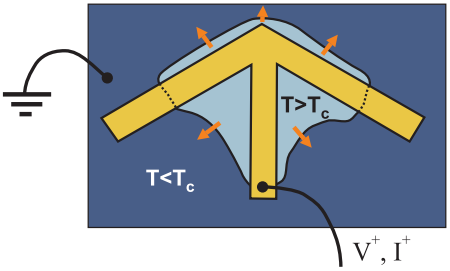

Figure 4.12.: Sketch: Base crystal heating in the vicinity of an arrow shaped mesa. The in plane current in the base crystal is symbolized by arrows.

is considerable. But there is no kink in the IVC indicating the formation of electro-thermal domains (hot spot). Even if there is no hot spot, the lateral temperature distribution in the mesa is highly non uniform for bias currents above the "knee" of the IVC. Confer to the calculated temperature distribution of a rectangular mesa depicted in figure 2.10. Obviously the power density caused by Joule heating is higher in the tip of the arrow as in the three branches. Therefore the maximum of the temperature distribution is in the tip of the mesa. The heating in the tip of the arrow seems to be so strong that arrow is separated into three quasi independent cavities (branches of the arrow) with slightly different resonance conditions. Hence, the standing wave pattern emerges in different branches of the arrow at different bias points.
It is not clear from the data, if above the jump in the IVC at 18 mA, which is indicating the switching of additional junctions, a hot spot is formed or not. But for bias currents greater than 18 mA, it is for sure that a considerable part at the tip of the arrow is above the critical temperature T_c .The dark line in the base crystal of image e-c can be explained by a LTSLM voltage response at the interface of the superconducting part to normal conducting part of the base crystal to an in plane current, cf. figure 4.12.

4.5. Detection of THz radiation in the hot spot bias regime

The standing wave patterns in the LTSLM images of the preceding section 4.2.1 raise the question if they are correlated with THz radiation. As described in section 3.4, an interferometer set-up was realized at the

National Institute of Material Science (NIMS) in Japan. The bolometer used as a detector with a 1 THz low-pass filter had been calibrated by a black body reference source (Infrared Systems Development Cooperation IR-564/3010) and independently by a Gunn Oscillator. Because the interferometer was by mistake aligned in such a way that the second parabolic mirror was focused on the aperture of the bolometer-cryostat and not on the entrance pupil of the Winston cone inside, the solid angle covered by the detector was reduced considerably to the value of 0.04 sr. Therefore, the maximum value of the emission power presented in this section is relatively small.
By measuring the angular dependence of the emission power from a BSCCO mesa, Yamaki et al. discovered an anisotropy in the emission characteristics [45]. This could be confirmed: In the case of a rectangular mesa the emission power from the short side of the mesa was lower than from the long side. Note that all the emission data presented in this section were detected from the long side of the mesa.
It should not go unmentioned that, although the author was in charge of setting up the interferometer, the emission data presented in this thesis were measured by Boris Groß, Huabing Wang, and his colleagues.
After the characterization of the emission properties at the NIMS in Japan, the samples were shipped to the Physikalisches Institut in Tübingen for LTSLM-imaging.

This section is organized as follows: First, the emission characteristics of two different mesas are discussed. In particular the frequency spectra of the radiation are presented from which the average frequency and the line width can be derived. These data are correlated with voltage response in the LTSLM. The second subsection is dedicated to the emission characteristics at different temperatures.

4.5.1. Emission characteristics of two rectangular mesas with different thickness

First, the emission characteristics (EMC) of a $330 \times 50\,\mu\mathrm{m}^2$ mesa with a thickness of approximately $1\,\mu$m, at a base temperature of 20 K, acquired in the interferometer set-up described in section 3.4, is discussed, cf. figure 4.13.
For biasing the mesa, the usual electric circuit consisting of a current

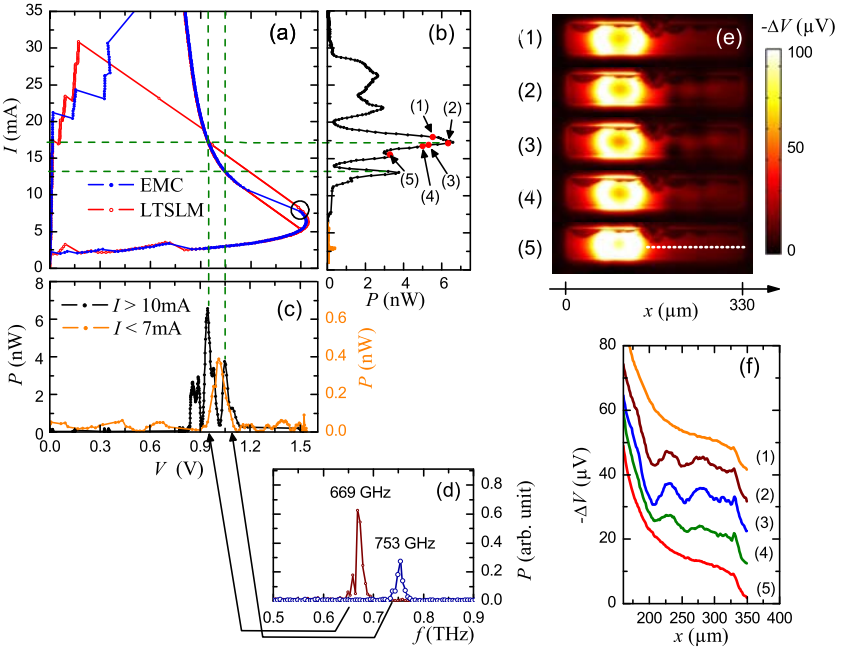

Figure 4.13.: Emission characteristics of a $50 \times 330\,\mu m^2$ mesa with thickness of approximately $1\,\mu m$ at a base temperature of 20 K: a) Current-voltage characteristics (IVC). The EMC curve corresponds to the emission measurement, while the LTSLM curve was recorded at the same base temperature in the LTSLM set-up. The point of thermal branching is denoted with a black circle. b) Emission power vs. current (EMIC). c) Emission power vs. voltage. The orange curve and the scale to the left correspond to the emission at low bias. d) Frequency spectra at a bias of 13.2 mA, 944 mV, and 17.2 mA, 1046 mV, respectively. The dashed green lines in figures a)-c) are indicating the bias points. e) LTSLM voltage images. Bias points are denoted with numbers in the EMIC of figure b). f) Linescans extracted from the LTSLM images. The path of the linescan is denoted by a white line in image (5). Adjacent linescans are shifted by $10\,\mu V$. From H.B. Wang, S. Guénon et al., Phys. Rev. Lett. **105**, 057002; © 2010 American Physical Society.

source with a load resistor in parallel to the sample (figure 3.4) was used. While sweeping the current injected into the mesa slowly, the current-voltage curve (IVC) was recorded (figure 4.13 a), curve EMC). Simultaneously, with the lamellar mirror of the interferometer at zero position, the bolometer was read out using lock-in technique. This way, the radiation power vs. current and voltage, respectively, was acquired, cf. figure 4.13 b) and c).
The contact resistance was removed numerically in the IVC. In the preceding sections 4.2.1, 4.2.3 and 4.2.2, the influence of self-heating on the IVC has been discussed in detail. The point of thermal branching is about 8 mA, 1.5 V (figure 4.13 a). Hence, the three large emission peaks in the emission power vs. current curve (EMIC) depicted in figure 4.13 b) are in the bias regime where a hot spot exists. Note also the small emission peak colored in orange in the low-bias regime where Ozyuzer et al. [69] have detected THz emission. In the emission power vs. voltage curve, for the emission power two different scales in the high-bias (hot spot) and the low-bias regime were used for clarity.
Assuming isotropic radiation, the maximum detected power of 6.5 nW can be extrapolated to a total power of 2.0 μW emitted in the whole solid angle of 4π. Note that a direct comparison between the documented radiation power in [69] and in this work is difficult due to different calibration techniques.
Ozyuzer et al. [69] have reported that at bias intervals in the low-bias regime, where electromagnetic radiation is detected, a bump in the IVC can be found, which is similar to the one depicted in figure 4.1 b). The height of this bump was up to 70 μA. This was explained by the transfer of power into the electromagnetic cavity modes at the resonance. In the IVC of figure 4.13 a) no bump can be seen after zooming in. Therefore, from the fact that for this sample the emission is significantly stronger in the hot spot regime than in the low-bias regime, it would not be safe to conclude that, in general, the emission in the hot spot regime is stronger. In the high-bias regime, any power transfer to the cavity mode could be compensated (at least to some extent) by the hot spot changing slightly in size. This would explain the absence of any bump in the IVC at high bias. Another explanation would be that simply no power is pumped into the cavity and the amount of power emitted is so small that it does not influence the IVC. Note that an emitted power of 2 μW at a voltage of approximately 1 V would only cause an increase in the current of 2 μA.

At the maxima of the two largest emission peaks, an autocorrelation function was acquired and mapped in a spectrum using fast Fourier transform with a Hanning window. Confer to section 3.4.2 for the details on the working principle of the interferometer. The spectra reveal that the emission is monochromatic with a center frequency of 669 GHz and 753 GHz, and a linewidth of 10 GHz and 16 GHz, respectively, cf. figure 4.13 d). The linewidths are in the resolution limit of the interferometer, cf. section 3.4.2. Note, because a 1 THz cut-off filter was used in front of the bolometer, it would not be possible to detect higher harmonics.
Assuming that the radiation is caused by the Josephson effect, the voltage drop per junction can be calculated by inserting the center frequency of the spectrum into the 2. Josephson relation. Then the number of junctions in the resistive state can be estimated by dividing the bias voltage by the voltage drop per junction. This results in a junction number of 682 and 671, respectively, which is in agreement with the estimated mesa thickness of 1 μm.
The sample was shipped to Tübingen for LTSLM-imaging. In figure 4.13 a) the IVC recorded in the LTSLM and in the interferometer set-up (EMC) are depicted. Despite the differences in thermal branching, the two curves are congruent in the outer-most branch.
In the low-bias regime, the LTSLM voltage images are homogeneous inside the mesa. In particular, no wave pattern appears at the bias of the small emission peak (orange curve in the EMCs). At the high-bias above the point of thermal branching, the typical hot spot feature described in section 4.2.1 appears, which in this case is elliptically shaped, similar to the one in the 70 μm mesa depicted in figure 4.3. In figure 4.13 e) a series of five LTSLM voltage images recorded at bias points of the largest emission peak is depicted. At the top edge of the mesa, the wave-like feature is the epoxy isolation while the largest dark spot is the silver paste connecting the top electrode. Left to the center of the mesa, the hot spot can be seen clearly. To the right a weak two-dimensional wave pattern appears in the images 2-4, which seems to attenuate to the right. For clarity, linescans have been extracted from the LTSLM voltage images, cf. figure 4.13 f).
If one assumes that the standing wave pattern in the LTSLM images 2-4 consists of a half wave along the width and three half waves along its length, the mode velocity $c \approx 4.7 \times 10^7$m/s can be calculated using $f = c(\lambda_x^{-2} + \lambda_y^{-2})^{1/2}$, with $f = 0.67$ THz and $\lambda_x \approx \lambda_y \approx 100\,\mu$m. Again the highest plasma mode is excited.

It was impossible to image a standing wave pattern at the two other emission peaks in the hot spot regime.

The second sample that shall be discussed here was a 0.7 μm-thick mesa with a size of $50 \times 330\,\mu$m. A base temperature of 40 K was chosen in this case.

Figure 4.14 a) depicts the two IVCs recorded at the interferometer setup (EMC) and the LTSLM setup (LSLM), respectively. Note that the abscissa is limited to high-voltage values. The point of thermal branching can be seen clearly. There is a small deviation between the curves for high-bias currents.

This mesa features an emission peak in the bias interval of 41 mA-55 mA and 449 mV and 465 mV, cf. figure 4.14 b) and c). Two spectra have been acquired at a bias voltage of 440 mV and 451 mV with a center frequency of 531 GHz and 554 GHz. The line width is approximately 20 GHz for both. The number of resistive junctions can be estimated between 401 and 394. Figure 4.14 e) depicts five LTSLM voltage images acquired at bias points in the emission interval. The current is injected from the left short edge of the mesa. In image 5) a hot spot feature can be seen on the left. For higher bias currents, the right hot spot edge, which is indicated by black arrows, moves to the right.

The other outstanding feature is the strong positive response at the long edges of the mesa at the right end, which seem to be connected by a dark stripe inside the mesa marked in image 3) with character A. Note, that this feature also appears in the LTSLM-images of other mesas (for instance, 70 μm-mesa (figure 4.3), two-injector mesa (figure 4.10), and arrow shaped mesa (figure 4.11)).

In the images 2-4 a second feature appears (marked by character B), which resembles feature A. Apparently, the emission of THz radiation is correlated with the emergence of this feature B. Because the LTSLM voltage images are to a certain degree quasi one-dimensional, it makes sense to investigate the LTSLM voltage response with a series of linescans, cf. figure 4.15 and figure 4.14 f). The colormap plot of the linescan series reveals again that the hot spot occupies more and more space of the mesa for higher bias currents and in this way reduces the length of the electromagnetic cavity defined by the stacked Josephson Junctions. The other remarkable result is that the emission is correlated with a significant change of the pattern to the right of the hot spot linescan $\alpha - \gamma$ and that this pattern is not adjusted but swallowed by the hot spot.

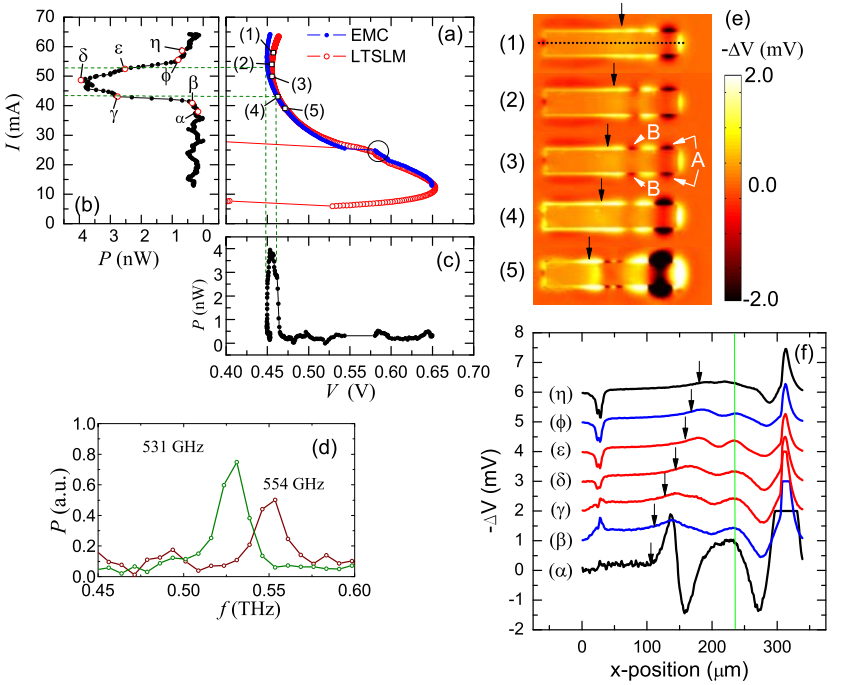

Figure 4.14.: Emission characteristics of a $330 \times 50\,\mu m^2$ mesa with thickness of approximately $0.7\,\mu m$ at a base temperature of 40 K: a) Current-voltage characteristics (IVC). The EMC curve corresponds to the emission measurement, while the LTSLM curve was recorded at the same base temperature in the LTSLM set-up. The point of thermal branching is denoted with a black circle. b) Emission power vs. current (EMIC). c) Emission power vs. voltage. d) Spectra acquired at a bias of 52.65 mA, 440 mV, and 43.82 mA, 451 mV, respectively. The dashed green lines in figure a)-c) indicate the bias points. e) LTSLM voltage images. Bias points are denoted with numbers in the IVC of figure a). Black arrows indicate the right edge of the hot spot. f) Linescans extracted from linescan series, cf. figure 4.15. The path of the linescan is denoted by a black line in image (1). The bias points are marked by Greek characters in figure b). Adjacent linescans are shifted by 1 mV. Black arrows indicate the right edge of the hot spot. From H.B. Wang, S. Guénon et al., Phys. Rev. Lett. **105**, 057002; © 2010 American Physical Society.

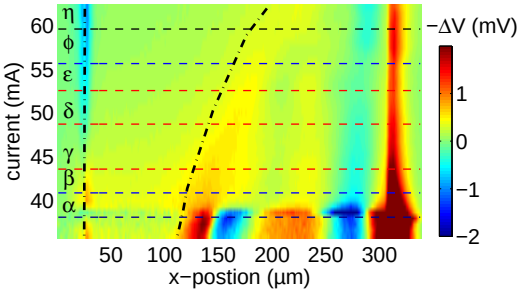

Figure 4.15.: Colormap plot of 41 LTSLM linescans acquired from the 0.7μm-thick mesa at different bias currents (36 mA - 62 mA). Confer to figure 4.14 e) for the path of the linescans. The hot spot (domain which is above T_c) is indicated by two dotted-dashed black lines. The dashed lines labeled with Greek characters indicates the bias currents marked in figure 4.14 b).

From the fact that the dark feature switches (changes its position) in the two-injector mesa and the arrow shaped mesa a defect in the mesa can be excluded. The reason for feature A and B could not be clarified.

4.5.2. Temperature dependence of the emission characteristics

The emission characteristic of the 0.7 μm-thick mesa already discussed in the preceding subsection (cf. figure 4.14) has been investigated over a wide temperature range: For any given base temperature, the emission characteristic has been recorded and three spectra of the emitted radiation (two with a bias point at each flank and one with a bias point at the center of the emission peak) have been acquired. All spectra show one pronounced emission peak with a center frequency of between 0.45-0.67 THz, indicating coherent electromagnetic radiation.
The graph in figure 4.16 a) reveals that for low base temperature, the frequency can be varied over a considerable frequency interval and that the center frequency decreases with increasing temperature. According to fig-

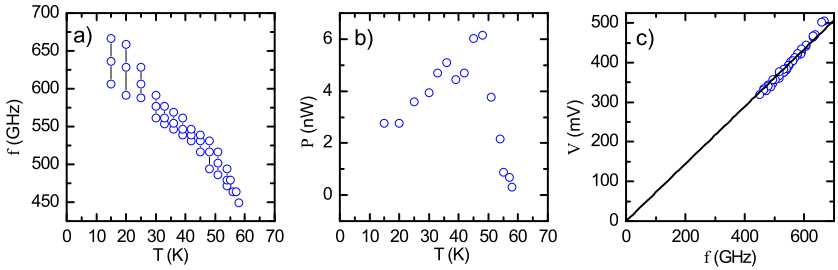

Figure 4.16.: Thin rectangular mesa (cf. figure 4.14) a) temperature dependence of the frequency range; b) emission power vs. temperature; c) bias voltage vs. emitting frequency. The black line is a plot of the voltage vs. frequency according to the 2. Josephson relation under the assumption that 350 junctions are in the resistive state. From H.B. Wang, S. Guénon et al., Phys. Rev. Lett. **105**, 057002; © 2010 American Physical Society.

ure 4.16 b) the emitted power is significant for a base temperature below 50 K. Hence, the frequency of the emitter can be varied over an interval between 470-670 GHz by choosing the appropriate base temperature.
The bias voltage vs. emitting frequency extracted from all spectra acquired are plotted into one graph (cf. figure 4.16 c)). The linear dependence can be seen clearly. The interpolating line is a voltage to Josephson frequency relation of a stack with 350 junctions that corresponds to a thickness of approximately 525 nm. The deviation to the thickness of 0.7 μm could be caused by junctions at the bottom of the mesa which do not switch into the resistive state. This could also explain the exceptional response of this sample during LTSLM-imaging.

4.5.3. Resonances in a disk-shaped mesa

The π-kink state described in section 2.9.3 was investigated theoretically not only for rectangular but also for disk-shaped and annular mesas by Hu et al. [42]. Disk-shaped mesas are particularly interesting in terms of

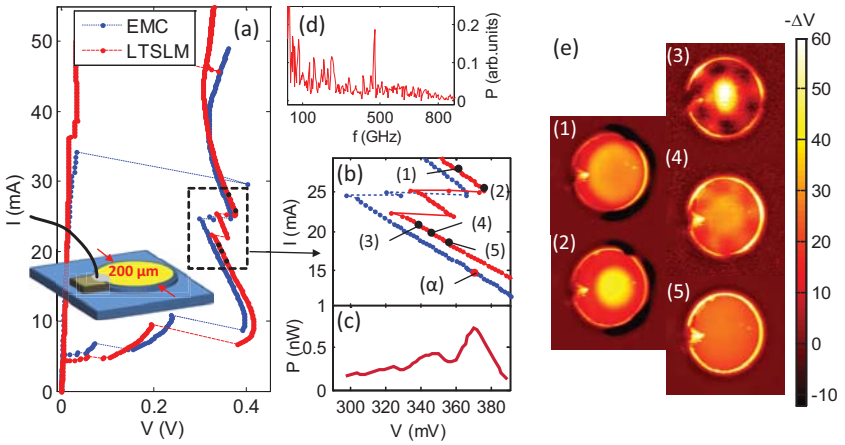

Figure 4.17.: Emission characteristics and LTSLM images of a disk-shaped mesa with a diameter of approximately 200 μm and a thickness of 0.9 μm at a base temperature of 20 K. a) Current-voltage characteristics (IVC); b) Zoom into the IVC; c) Emission characteristic (EMC); d) Spectrum acquired at the bias point (α) is indicated in the zoomed IVC; e) LTSLM images: The bias points are marked by numbers in the zoomed IVC. From S. Guénon et al., Phys. Rev. B **82**, 214506; © 2010 American Physical Society.

LTSLM-imaging, because the wave pattern is expected to be non-trivial and easy to distinguish from a pattern that, for instance, is caused by fluxon dynamics.
In figure 4.17 emission data and LTSLM images of a disk shaped mesa with a diameter of 200 μm at a base temperature of approximately 20 K are presented. Again figure 4.17 depicts the current-voltage curves (IVCs) acquired in the interferometer- (EMC) and the LTSLM set-up (LTSLM), respectively. These two curves do not coincide very well in this case. There is a considerable voltage difference for injection currents above 40 mA, probably caused by a systematic error in one of the set-ups. In the attempt to reduce the mismatch between both IVC, a base temperature of 19 K instead of 20 K was chosen for the measurements in the LTSLM. Note the jump in the current interval between 30-20 mA, which is caused by the switching of approximately 20 % of the junctions from the resistive to the superconducting state. This is remarkable because, in the other samples investigated, the number of resistive junctions stays constant for high-bias currents.Below this jump but above the "knee" in the current interval between 20 mA and 7 mA there is a no kink to lower voltages indicating thermal branching. Obviously the branching temperature is shifted to higher values for this geometry as already mentioned in section 4.2.3.
A section of the IVCs is presented in figure 4.17 b) for clarity. The corresponding emission characteristic is depicted in figure c). The maximum emission power is almost one order of magnitude smaller than for the rectangular mesa. At bias point α with a bias voltage of approximately 370 mV, a spectrum of the electromagnetic radiation was acquired cf. figure d). The center frequency is 472 GHz and the line width is about 12 GHz. The number of resistive junctions calculated using the 2. Josephson relation is about 380. The mesa thickness of 0.9 μm corresponds to approximately 600 junctions. Hence, a considerable number of junctions do not switch into the resistive state.
Confer to the inset of figure 4.17 a) for a scheme of the sample geometry. Note that the top electrode is connected to the mesa at the edge in order to facilitate the LTSLM-imaging process. The LTSLM images for bias points in the interval of emission are depicted in figure 4.17 e). For bias points above the jump (image 1-2), a hot spot feature can be identified. For bias points right below the jump, a non trivial wave pattern appears (image 2-3), which vanishes for smaller bias currents (image 5). Obvi-

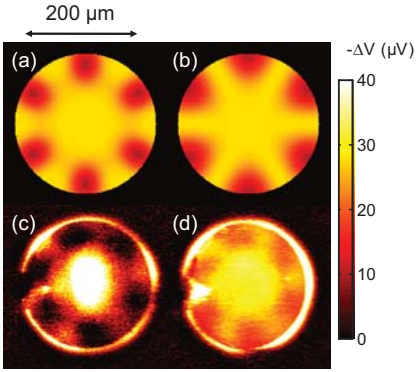

Figure 4.18.: Plots of the (3,1)-plasma modes according to [42] a) the square of the magnetic field B^2. b) the square of the electric field E^2. c) and d) for comparison: LTSLM images of figure 4.17 e) with modified color scale. From S. Guénon et al., Phys. Rev. B **82**, 214506; © 2010 American Physical Society.

ously, the appearance of the wave pattern does not exactly match to the emission peak in figure c), but it is shifted to higher bias currents.

In figure 4.18 the square of the magnetic (a) and electric field (b) of the (3,1) plasma (cavity) mode according to [42] are depicted. The color scale of these plots was chosen to match the color scale of the LTSLM images depicted in figures 4.18 c) and d). Comparing the theoretical plots with the LTSLM images reveals that the LTSLM images resemble the square of the magnetic field plots, which is in agreement with the observation of [61] that in planar niobium-junctions, the square of the magnetic field component of the plasma wave creates the response of the cavity modes in the LTSEM. From the (3,1) mode, a mode velocity of $c \approx 7 \times 10^7$m/s can be derived, which is the value expected if all junctions oscillate in phase.

5. Summary & Conclusions

Using the low-temperature scanning laser microscope (LTSLM), it was possible to image standing wave patterns in a large BSCCO mesa at the low-bias (sub gap) regime where Ozyuzer et al. detected coherent THz radiation of significant power from similar samples. In contrast to the assumption of Ozyuzer et al., that the cavity mode is modulated parallel to the short side of the mesa, the wave patterns are modulated parallel to the long side.

For high bias currents, where the Joule heating is very strong, electro-thermal domains (hot spot) can be identified in LTSLM-voltage images. The formation of electro-thermal domains is associated with a small kink in the current-voltage curve (IVC) (thermal branching). Spenke et al. [88] developed a theory concerning heating in negative thermal resistors. By applying this theory, IVCs were parameterized from the temperature dependence of the c-axis resistivity ρ_c and the thermal conductivity κ_c, which resemble the measured IVCs. In addition, bias points of thermal branching were calculated that were in good agreement with the experiment.

The temperature distribution in the base crystal in the vicinity of a large BSCCO was monitored. For this purpose, a special sample was prepared with a main mesa surrounded by small detector mesas. By making use of the monotonic temperature dependence of the critical current, these detector mesas were used as temperature sensors. It was discovered that the temperature in the base crystal is above the critical temperature T_c of the superconducting BSCCO if the electro-thermal domain wall has passed a sensor.

A simple Michelson interferometer with a lamellar mirror as a beam splitter and a bolometer as a detector was realized: This set-up proved itself as a highly sensitive, relatively cheap tool for detecting THz radiation from a low temperature emitter.

With the help of this interferometer, the emission of coherent THz radiation from a mesa in the hot spot bias regime could be verified. In

terms of applications, the hot spot bias regime might be interesting, because, in contrast to the low-bias regime where Ozyuzer et al. detected THz-radiation for the first time, the bias is much more stable and reproducible. In addition we could show that it is possible to vary the frequency by choosing the appropriate base temperature. Hence, in the hot spot bias regime the THz emitter is to a certain level tunable.
We were also able to verify that in the hot spot bias regime the frequency-voltage relation of the THz emitter is in principle determined by the Josephson relation. This way, other mechanisms causing the THz radiation can be excluded.
In the hot spot bias regime, where electro-thermal domains exist, the mesa is divided into two parts with different temperatures and current densities. Usually, the part at high temperature (hot spot) is considerably above the critical temperature T_c of BSCCO. Hence, the layers (i.e., the intrinsic Josephson Junctions) are individually electrically shunted by the hot spot. The cold part of the mesa, on the other hand, has a more or less uniform heat distribution slightly above the base temperature. In a narrow mesa the electro-thermal domains are quasi one dimensional and the electro-thermal domain wall acts as a moveable boundary of a "cold" cavity.
It is a well known fact that shunt resistors can be useful for synchronizing Josephson net works. But it should be noted, that some BSCCO mesas emit coherent THz radiation of considerable power in the low bias regime or at the "knee" of the IVC (below the point of thermal branching). Therefore, a hot spot might be useful but it is not necessary for synchronizing the Josephson oscillations.
For two cases (rectangular mesa and disk shaped mesa) it was possible to image a standing wave pattern of the plasma modes correlated with the emission of THz-radiation. By calculating the plasma mode velocity using the wave lengths derived from the LTSLM voltage images and the frequencies from the acquired spectra, it can be show that the highest plasma mode with in phase oscillations is excited. This supports the hypothesis of Ozyuzer et al., that the mesa forms a plasma wave cavity which synchronizes the Josephson oscillations.

Part II.

A Cryogenic Scanning Polarizing Microscope for Magneto-Optical Imaging

6. Motivation

Originally it was planned to extend the low-temperature scanning laser microscope (cf. section 3.2) described in the first part of this thesis with the facility of polarizing microscopy. The idea was to combine the LTSLM voltage imaging with the possibility of magneto-optical imaging. But it soon turned out that a new design would be necessary, because the integration of the additional components in the old system was too elaborate.
In magneto-optical imaging, the weak dependence of the optical constants on the direction of the magnetization is utilized cf. [43]. This can lead to a magnetization-dependent birefringence for linear polarized light (Voigt effect/Cotton-Mouton effect) or for circular polarized light (Faraday effect in transmission and Kerr effect in reflection).
With a polarizing microscope, the variation in the birefringence of a sample can be imaged: This is a conventional microscope that is additionally fitted with two (crossed) optical polarizers. The first polarizer linearly polarizes the illuminating light. After the light has passed the sample, the second polarizer (analyzer) generates a contrast in the image that is proportional to the variation in the plane of polarization. This way, the birefringence of circular polarized light can be imaged. If a compensator is added in the optical path, it is also possible to image the variation in the ellipticity, and as a result, the birefringence of linear polarized light.
Because the magneto-optical effects are very weak, the requirements on the polarizing microscope are very high. In order to reduce the contrast of non-magnetic origin (usually caused by the varying reflectivity of the sample surface), it is necessary to subtract a magnetically saturated image from the image that contains the magnetic contrast [41, 86, 83]. Images with a high signal-to-noise ratio are needed for this differential technique. Therefore, the sample should be illuminated with high intensity. A mercury vapor lamp could be used for this purpose. An alternative light-source would be a laser but the coherent illumination causes disturbing diffraction fringes. Therefore, the coherence of the illumination has to be destroyed (e.g., by a vibrating fiber) in this case.

However, a coherent light-source can be used in a scanning laser microscope (SLM). As described in section 3.2 in an SLM, a laser beam is focused on the sample surface by an objective lens and then the reflected light is directed into a photo detector via a beam splitter. By scanning the laser spot and mapping the signal of the photo detector, an image of the reflected light-intensity is acquired. This design can be extended to a scanning polarizing microscope (cf. for instance [15]) by adding an optical polarizer in front of the laser and by replacing the single photo detector with a polarizing beam splitter or a Wollastone-prism, respectively, which divides the laser beam into two cross-polarized beamlets and directs them to two photo diodes. The difference in the signal of the two photo detectors is proportional to the variation in the plane of polarization caused by the sample (cf. section 8.1 for a detailed description).
A laser scanning polarization microscope (SPM) has certain advantages in comparison with a conventional microscope. The laser provides monochromatic illumination of high power which is focused on one spot. Therefore, very high illumination intensities can be reached easily. In fact, usually the illumination intensity is limited by the intensity threshold of the sample. By adding a pinhole in front of the detector, the design of the microscope is made confocal and the resolution is improved by a factor of 1.4. The serial signal processing facilitates the optimization of the signal-noise ratio. Usually it is not necessary to subtract a magnetically saturated image because the non-magnetic contrast can be reduced by normalizing the difference of the two photo detector signals with their sum.
The disadvantages of a scanning polarizing microscope are that, if a slow scanner is used, the imaging takes a longer time, and the thermal load to the sample caused by the laser spot might be quite high.
A SPM would be useful for the research on a broad variety of different samples: One example would be the Kerr microscopy of magnetic thin films or multi-layers [62].
Another example is the tunneling magneto-resistance (TMR) in a magnetic tunnel junction (MTJ): For crystalline tunneling barriers (like MgO), the tunneling is coherent and the temperature-dependence of the TMR depends on the relative orientation of the magnetization in the two electrodes of the MTJ [71]. In this case it is possible to image intermediate magnetic states with an LTSLM voltage image [109]. Utilizing Kerr microscopy the absolute magnetization orientation in the electrodes could be imaged, too.

Kerr microscopy would be also very helpful for the investigation of superconducting-ferromagnetic hetero-structures [29, 110]. Here the LTSLM voltage image provides information on the superconducting state and its current distribution while the magnetization of the ferromagnetic layer can be imaged via the scanning polarizing microscope (SPM).
If a magneto-optical sensor layer is used (for instance EuSe or an iron-garnet single crystal), it is possible to image the magnetic stray field of the sample via a polarization microscope. Welp et al. [108] used this technique to image the domain structure in the diluted magnetic semiconductor GaMnAs. Another application for magneto-optics with a sensor layer is the investigation of vortices in a Type-II superconductor [31, 32].
Many of the samples of interest are cryogenic samples, i.e., their base temperature is supposed to be below 123 K. This has technical consequences: It is impossible to operate a conventional objective lens at cryogenic temperatures because the cool down would destroy the cemented lenses. Therefore, the objective lens must not be in thermal contact with the sample. Hence, oil immersion lenses cannot be used for this application. Cryogenic temperatures imply the usage of an isolation vacuum and, as a consequence, require a cryostat window in the optical path of the microscope. If this cryostat window is located between the objective lens and the sample, the stress-induced birefringence of the window would considerably disturb the polarization microscopy. The solution to this problem is to situate the objective lens inside the vacuum, as realized by Goa et al. [31]. But this configuration poses high mechanical demands on the supports of the cryostat and on the positioning unit, which is needed for focusing and selecting the field of view of the microscope.
This part is organized as follows: In the first chapter, an introduction in the field of magneto-optics is given by discussing the interaction of light and matter. In the following chapter, the planned design and its components are discussed, while in the next chapter the set-ups for testing the microscope are described and the test results are presented. In the last chapter, an outlook is given on how to proceed with this project.

7. Theory & Fundamentals

7.1. Interaction of Light and Matter

7.1.1. Electrodynamics

Classical electro-dynamics is described by the *Maxwell's equations*, which relate the electric displacement field $\vec{D}$, the magnetization field $\vec{H}$, the electric field $\vec{E}$, the magnetic field $\vec{B}$, the charge density ρ, and current density $\vec{J}$.

$$\nabla \cdot \vec{D} = \rho \quad \text{(Gauss's law)} \tag{7.1a}$$

$$\nabla \cdot \vec{B} = 0 \quad \text{(Gauss's law for magnetism)} \tag{7.1b}$$

$$\nabla \times \vec{E} = -\partial_t \vec{B} \quad \text{(Faraday's law of induction)} \tag{7.1c}$$

$$\nabla \times \vec{H} = \vec{J} - \partial_t \vec{E} \quad \text{(Ampère's circuital law)} \tag{7.1d}$$

The macroscopic and microscopic fields are related by the following constituent equations

$$\vec{D} = \epsilon_0 \, \vec{E} + \vec{P} \tag{7.2a}$$

$$\vec{H} = \frac{1}{\mu_0} \, \vec{B} - \vec{M} \tag{7.2b}$$

where ϵ_0 and μ_0 are the vacuum permittivity and permeability, and $\vec{P}$ and $\vec{M}$ are the polarization and magnetization fields.
For isotropic and linear materials, the polarization is proportional to the electric field and the magnetization is proportional to the magnetization field

$$\vec{P} = \epsilon_0 \, \chi_e \, \vec{E} \tag{7.3a}$$

$$\vec{M} = \chi_m \, \vec{H} \tag{7.3b}$$

and the constituent relations are reduced to

$$\vec{D} = \epsilon \, \vec{E} \tag{7.4a}$$

$$\vec{H} = \frac{\vec{B}}{\mu} \tag{7.4b}$$

with

$$\epsilon = \epsilon_0 \, (1 + \chi_e) \tag{7.5a}$$

$$\mu = \mu_0 \, (1 + \chi_m) \tag{7.5b}$$

where the two material constants ϵ and μ are called the permittivity and permeability, and χ_e and χ_m are the electric and magnetic susceptibilities, respectively.
Ohm's law can be written as

$$\vec{J} = \sigma \, \vec{E} \tag{7.6}$$

where σ is the conductivtiy.

7.1.2. Planar electromagnetic waves

Inserting Ohm's law into the fourth Maxwell equation and applying vector analysis leads to the *Telegrapher's equations*

$$\nabla^2 \vec{B} - \mu\epsilon\partial_t^2 \vec{B} - \mu\sigma\partial_t \vec{B} = 0 \tag{7.7a}$$

$$\nabla^2 \vec{E} - \mu\epsilon\partial_t^2 \vec{E} - \mu\sigma\partial_t \vec{E} = 0 \tag{7.7b}$$

For a non-conductive medium ($\sigma = 0$), these equations are reduced to the wave equations

$$\nabla^2 \vec{B} - \mu\epsilon\partial_t^2 \vec{B} = 0 \tag{7.8a}$$

$$\nabla^2 \vec{E} - \mu\epsilon\partial_t^2 \vec{E} = 0 \tag{7.8b}$$

which describe a transversal wave with a phase velocity (speed of light) $c^2 = 1/\mu\epsilon$. The simplest solutions to this equation are *plane waves*.

$$\vec{E}(\vec{r}, t) = \hat{E} e^{i(\vec{k}\cdot\vec{r} - \omega \, t)} \tag{7.9a}$$

$$\vec{B}(\vec{r}, t) = \hat{B} e^{i(\vec{k}\cdot\vec{r} - \omega \, t)} \tag{7.9b}$$

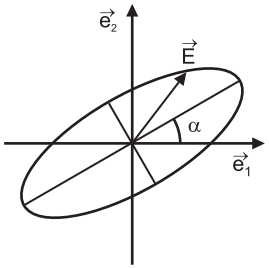

Figure 7.1.: Electric field vector for an elliptically polarized plane wave.

where $\hat{E}$, $\hat{B}$ are the (complex) amplitude vectors, $\vec{k}$ is the wave vector, and ω the angular frequency. The wave equations and Maxwell's equations imply the following well-known relations:

$$|\vec{k}| = \frac{\omega}{c} \tag{7.10a}$$

$$\hat{B} = \frac{1}{c}\frac{\vec{k}}{|\vec{k}|} \times \hat{E} \tag{7.10b}$$

7.1.3. Polarization and Jones calculus

Consider planar waves with the linear-independent unit vectors $\vec{e}_1$ and $\vec{e}_2$ and the complex amplitudes E_{01} and E_{02}

$$\vec{E}_1 = E_{01}\,\vec{e}_1\,e^{i(\vec{k}\cdot\vec{r}-\omega\,t)} \tag{7.11a}$$

$$\vec{E}_2 = E_{02}\,\vec{e}_2\,e^{i(\vec{k}\cdot\vec{r}-\omega\,t)} \tag{7.11b}$$

Such waves are said to be *linearly polarized* with the polarization vector $\vec{e}_1$ or $\vec{e}_2$, respectively. The superposition of those two wave expressions is the most general solution of a plane wave propagating in $\vec{k}$-direction.

$$\vec{E} = (E_{01}\,\vec{e}_1 + E_{02}\,\vec{e}_2)e^{i(\vec{k}\cdot\vec{r}-\omega t)} \tag{7.12}$$

It can be shown that the electric field vector in a plane perpendicular to the direction of propagation $\vec{k}$ describes an ellipse (cf. figure 7.1.3), or in other words the wave is *elliptically polarized*. . If δ is the phase difference between the two complex amplitudes E_{01} and E_{02}

$$E_{01} - E_{02} = |E_{01} - E_{02}|e^{i\delta} \tag{7.13}$$

Polarization	Jones vector
"horizontal" linearly polarized	$\begin{bmatrix}1\\0\end{bmatrix}$
"vertical" linearly polarized	$\begin{bmatrix}0\\1\end{bmatrix}$
"right hand" circularly polarized	$\frac{1}{\sqrt{2}}\begin{bmatrix}1\\-i\end{bmatrix}$
"left hand" circularly polarized	$\frac{1}{\sqrt{2}}\begin{bmatrix}1\\i\end{bmatrix}$

Table 7.1.: Examples of normalized Jones vectors

then the angle α, which denotes the orientation of the ellipse, is given by

$$\tan(2\alpha) = \frac{2\,|E_{01}|\,|E_{02}|\,\cos\delta}{|E_{01}|^2 + |E_{02}|^2} \tag{7.14}$$

If $\delta = \pi/2 \bmod 2\pi$ then $\alpha = 0$ and the ellipse is described by following equation

$$\frac{E_1^2}{|E_{01}|^2} + \frac{E_2^2}{|E_{02}|^2} = 1 \tag{7.15}$$

where E_1 and E_2 are the components of the electrical field vector $\vec{E}$.
If in addition $|E_{01}| = |E_{02}|$ then the field vector describes a circle (*circularly polarized* electromagnetic wave).

The Jones calculus is based on the component notation of the unit vectors in equation 7.12. This way, polarized light and optical components can be described by two component vectors and 2×2 matrices, respectively (cf. table 7.1).

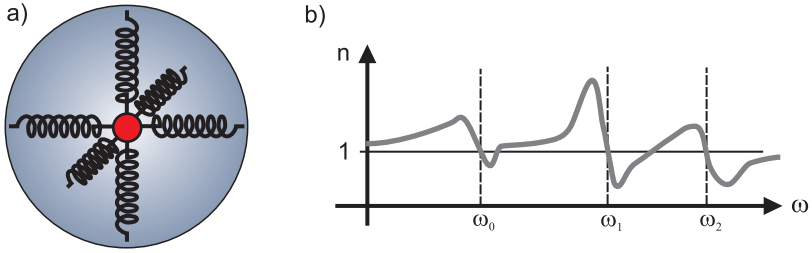

Figure 7.2.: a) Lorentz model: Charge bound in a classical harmonic oscillator. b) Dispersion: Frequency-dependence of the index of refraction (sketch).

7.1.4. Absorption & Dispersion

The index of refraction is defined as the ratio between the speed of light in vacuum c_0 and the speed of light c in the medium of interest

$$n \equiv \frac{c_0}{c} = \sqrt{\frac{\mu\epsilon}{\mu_0\epsilon_0}} \tag{7.16}$$

which depends on the angular frequency ω of the electromagnetic wave. For frequencies higher than a few GHz, the permeability is equal to one in most cases. Hence, in optics the index of refraction is reduced to

$$n = c_0\sqrt{\epsilon} \tag{7.17}$$

If a complex wave number is defined, it is possible to describe a planar electromagnetic wave in a dissipative medium via the wave equation 7.8b

$$k = k' + i\,k'' \tag{7.18}$$

This implies also a complex permittivity and a complex index of refraction:

$$\epsilon = \epsilon' + i\,\epsilon'' \tag{7.19a}$$

$$n = \frac{c_0}{\omega}k \implies n = n' + i\,n'' \tag{7.19b}$$

The complex permittivity and index of refraction are related by (cf. [56], § 63)

$$\epsilon' = c_0^2 \left(n'^2 - n''^2 \right); \quad \epsilon'' = 2c_0^2\, n' n'' \tag{7.20a}$$

$$n' = c_0 \sqrt{\frac{1}{2}\left[\epsilon' + \sqrt{\epsilon'^2 + \epsilon''^2}\right]}; \quad n'' = c_0 \sqrt{\frac{1}{2}\left[-\epsilon' + \sqrt{\epsilon'^2 + \epsilon''^2}\right]} \tag{7.20b}$$

The definition of a complex permittivity is somewhat arbitrary. Instead of regarding the dissipation by the imaginary part of the permittivity, it is also possible to introduce a frequency-dependent conductivity σ (cf. [44], chap. 7.7. and [74] chap. 20.6.). As will become apparent later on, $\epsilon''(\omega)$ diverges for $\omega \to 0$ in metals. In this case most authors introduce the complex optical conductivity

$$\sigma(\omega) = i\,\omega\epsilon(\omega) \tag{7.21}$$

In the *Lorentz model* the response of the charge carriers in the medium to the electromagnetic wave is approximated by classical harmonic oscillators (cf. figure 7.2 a)). Consider the equation of motion for an electron of charge $-e$ bound in an harmonic oscillator with the resonance frequency ω_j under the influence of an electric field $\vec{E}_{\text{local}}$

$$m\left(\partial_t^2 \vec{r} + \gamma \partial_t \vec{r} + \omega_j^2 \vec{r}\right) = -e\vec{E}_{\text{local}}(\vec{r}, t) \tag{7.22}$$

where γ is the damping parameter. The dipole moment $\vec{p}$ of a single electron that is contributing to the polarization $\vec{P}$ is given by

$$\vec{p} = -e\,\vec{r} = \frac{e^2}{m}\left(\omega_j^2 - \omega^2 - i\omega\gamma\right)^{-1} \vec{E}_{\text{local}} \tag{7.23}$$

In the case of $\vec{E}_{\text{local}} = \vec{E}$, where the field influencing the harmonic oscillators is equal to the external field, the (complex) permittivity is

$$\epsilon(\omega) = \epsilon_0 \left(1 + \frac{N\,e^2}{m\,\epsilon_0} \sum_j \frac{f_j}{\omega_j^2 - \omega^2 - i\omega\gamma}\right) \tag{7.24}$$

where the oscillator strength f_j satisfies the sum rule

$$\sum_j f_j = Z \tag{7.25}$$

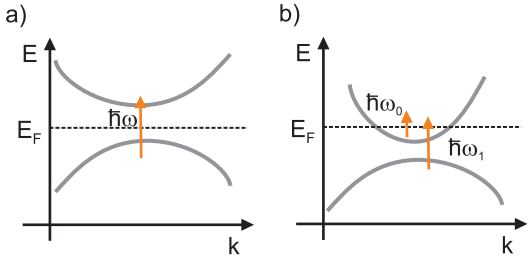

Figure 7.3.: Response to electromagnetic radiation: a) inter-band transition in an isolator b) intra- and inter-band transition in a metal.

and Z is the number of different oscillators in the medium.
In metals there exists an additional response of the free electrons (*Drude-Zener model*). This response can be obtained easily by considering the limit of oscillator equation 7.22 for $\omega \to 0$. Hence, the permittivity of a metal is

$$\epsilon(\omega) = \epsilon_0 \left(1 - \underbrace{\frac{N\,e^2}{m\,\epsilon_0} \frac{1}{\omega^2 + i\omega\gamma}}_{\text{free electron response}} + \frac{N\,e^2}{m\,\epsilon_0} \sum_j \frac{f_j}{\omega_j^2 - \omega^2 - i\omega\gamma} \right) \tag{7.26}$$

In dense media the polarization surrounding the oscillator is influencing the local electric field and $\vec{E}_{\text{local}} \neq \vec{E}$. Analog to the *Clausius-Mossotti equation*, in this case the index of refraction can be written as

$$\frac{n^2 - 1}{n^2 + 2} = \frac{N\,e^2}{3\,m\,\epsilon_0} \sum_j \frac{f_j}{\omega_j^2 - \omega^2 - i\omega\gamma} \tag{7.27}$$

Confer to figure 7.2 b) for a sketch on the typical frequency-dependence of the index of refraction in a solid. Note that (according to equation 7.22) the resonance frequencies ω_j are also the frequencies where the absorption of the material has a maximum.

A quantum mechanical discussion of the dispersion in a solid leads qualitatively to the same result. Here, instead of the resonances of classical oscillators, the *intra- and inter-band transitions* are considered (cf. figure 7.3).

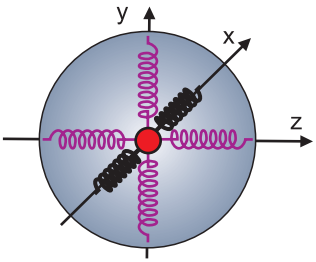

Figure 7.4.: Uniaxial birefringence in the Lorentz model: The optical anisotropy results in different "spring constants" for the x-direction and the y-, z-direction. In this case the optical axis is along the x-direction.

7.1.5. Dichroism & Birefringence

If an optical medium is anisotropic, the electric displacement field $\vec{D}$ is not necessarily collinear with the electric field $\vec{E}$, and as a consequence the scalar permittivity ϵ has to be replaced by a tensor $\bar{\epsilon}$.

$$\vec{D} = \bar{\epsilon}\vec{E} \tag{7.28}$$

The anisotropy also influences the dispersion of the medium. Consider for instance a uniaxial material in the Lorentz model (cf. figure 7.4). The response of the material to an electromagnetic wave depends on the direction of the electric field vector. For an electromagnetic wave polarized in the direction of the optical axis, the resonance frequency is different from the resonance frequency of a wave polarized perpendicularly (cf. figure 7.5). If an electromagnetic wave has a frequency ω_d, the absorption depends on the polarization direction. Such a behavior is called *dichroism*. But even if the wave has a frequency ω_b, where the absorption coefficient is more or less polarization-independent, the phase velocity could depend considerably on the polarization direction. This phenomenon is called *birefringence* and is discussed in the following.
According to the *Huygens-Fresnel principle*, any point of a primary wave front can be considered as the origin of a secondary spherical elementary wave, and at a later point in time these elementary secondary waves compose to a wave front of the primary wave again.
Because the phase velocity depends on the polarization direction, it is necessary to revise the Huygens-Fresnel principle in such a way that (depending on the polarization) the elementary waves are ellipsoids (cf. figure 7.6 a)).

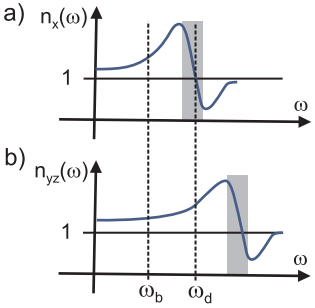

Figure 7.5.: Sketch of the dispersion in an uniaxial birefringence medium: a) in x-direction (optical axis) b) in yz-direction. The shaded rectangles are indicating frequency intervals of resonant absorption. ω_b and ω_d are angular frequencies where the medium exhibits birefringence or dichroism, respectively.

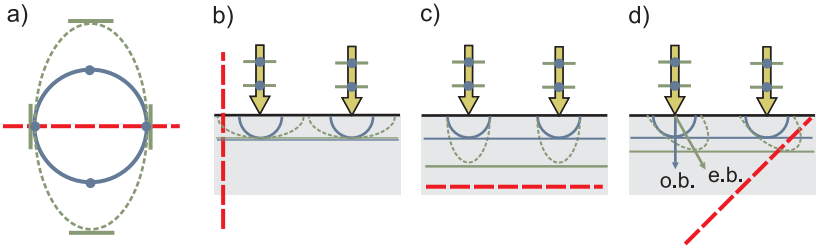

Figure 7.6.: Wave propagation in a uniaxial birefringent material. The polarization direction is indicated by a point if it is perpendicular to the image plane or by a line. a) Depending on the polarization, the elementary wave is circular or elliptical. b)-d) Birefringence depending on the direction of incidence.

Now the Huygens-Fresnel principle is applied to a plane wave entering an interface between vacuum and a uniaxial birefringent material. If the direction of incidence is parallel to the optical axis, the wave propagation is not polarization-dependent (cf. figure 7.6 b)). In the case of an incident direction perpendicular to the optical axis, the incoming wave splits into two waves with different polarization and different phase velocities (cf. figure 7.6 c)). For an optic axis with arbitrary orientation, the incoming wave splits into an ordinary beam (o.b.) and a deflected extraordinary beam (e.o.); its direction can be constructed applying the Huygens-Fresnel principle (cf. figure 7.6 d)).

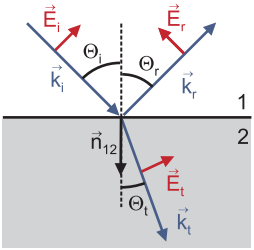

Figure 7.7.: Incident planar wave k_i passes a planar interface between different media, causing a reflected wave k_r and a refracted wave k_t.

7.1.6. Reflection and Refraction on Interfaces

In this section the phenomena of reflection and refraction of light on an interface between two optical media are discussed. Again a light beam is treated as a planar electromagnetic wave. According to the Maxwell equation, the following boundary conditions exist for the electromagnetic fields at the interface:

$$\vec{n}_{12} \cdot (\vec{D}_2 - \vec{D}_1) = \tilde{\rho} \tag{7.29a}$$

$$\vec{n}_{12} \times (\vec{E}_2 - \vec{E}_1) = 0 \tag{7.29b}$$

$$\vec{n}_{12} \cdot (\vec{B}_2 - \vec{B}_1) = 0 \tag{7.29c}$$

$$\vec{n}_{12} \times (\vec{H}_2 - \vec{H}_1) = \tilde{j} \tag{7.29d}$$

$\vec{n}_{12}$ is the unit vector normal to the interface and directed from the first medium to the second. $\tilde{\rho}$ and $\tilde{j}$ are the charge- and current-surface densities, respectively.
The incident planar wave, the reflected wave, and the transmitted wave can be expressed as (cf. figure 7.7)

$$\vec{E}_i = \vec{E}_{0i} \exp\left[i\left(\vec{k}_i \cdot \vec{r} - \omega_i t\right)\right] \tag{7.30a}$$

$$\vec{E}_r = \vec{E}_{0r} \exp\left[i\left(\vec{k}_r \cdot \vec{r} - \omega_r t + \delta_r\right)\right] \tag{7.30b}$$

$$\vec{E}_t = \vec{E}_{0t} \exp\left[i\left(\vec{k}_t \cdot \vec{r} - \omega_t t - \delta_t\right)\right] \tag{7.30c}$$

With the help of the boundary condition 7.29b, it is easy to show that the frequency for all three waves is the same

$$\omega_i = \omega_r = \omega_t \tag{7.31}$$

In addition, the law of reflection

$$\theta_i = \theta_r \tag{7.32}$$

and the *Snell's law* of refraction

$$n_i \sin\theta_i = n_t \sin\theta_t \tag{7.33}$$

can be derived from the same boundary condition.
In order to analyze the amplitudes between two dielectric media it is necessary to distinguish between two cases:
The first case is the incoming wave polarized perpendicularly to the plane of incidence. With the help of the boundary condition 7.29d the *Fresnel equations* can be derived

$$r_\perp \equiv \left(\frac{E_{0r}}{E_{0i}}\right)_\perp = \frac{n_1\cos\theta_i - n_2\cos\theta_t}{n_1\cos\theta_i + n_2\cos\theta_t} \tag{7.34a}$$

$$t_\perp \equiv \left(\frac{E_{0t}}{E_{0i}}\right)_\perp = \frac{2n_1\cos\theta_i}{n_1\cos\theta_i + n_2\cos\theta_t} \tag{7.34b}$$

In the second case, the incident wave is polarized in the plane of incidence and the *Fresnel equations* are

$$r_\parallel \equiv \left(\frac{E_{0r}}{E_{0i}}\right)_\parallel = \frac{n_2\cos\theta_i - n_1\cos\theta_t}{n_1\cos\theta_i + n_2\cos\theta_t} \tag{7.35a}$$

$$t_\parallel \equiv \left(\frac{E_{0t}}{E_{0i}}\right)_\parallel = \frac{2n_1\cos\theta_i}{n_1\cos\theta_t + n_2\cos\theta_i} \tag{7.35b}$$

7.1.7. Magneto-optical Effects

A comprehensive discussion of magneto-optical effects can be found in the monographs [43, 117].
The dynamics of the charge carriers in a medium is influenced by an applied magnetic field resulting in a field-dependent electromagnetic response. Using the sign convention in [2], the permittivity tensor for a cubic crystal can be written as:

$$\bar{\epsilon} = \epsilon \begin{bmatrix} 1 & -iQ_v m_3 & iQ_v m_2 \\ iQ_v m_3 & 1 & iQ_v m_1 \\ -iQ_v m_2 & iQ_v m_1 & 1 \end{bmatrix} + \begin{bmatrix} B_1 m_1^2 & B_2 m_1 m_2 & B_2 m_1 m_3 \\ B_2 m_1 m_2 & B_1 m_2^2 & B_2 m_2 m_3 \\ B_2 m_1 m_3 & B_2 m_2 m_3 & B_1 m_3^2 \end{bmatrix} \tag{7.36}$$

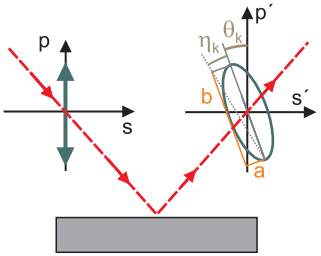

Figure 7.8.: Kerr rotation (schematic view): The coordinate systems p-s and p'-s' lie in a plane perpendicular to the direction of propagation while p and p' are parallel and s and s' are perpendicular to the plane of incidence. Θ_k and η_k denote the Kerr rotation and ellipticity, respectively.

m_1, m_2 and m_3 are the components of the magnetization vector. Q_v is the Voigt constant, which describes the magneto-optical circular birefringence due to the Kerr or Faraday effect, respectively. The constants B_1 and B_2 describe the Voigt effect.
Ignoring the Voigt effect, the dielectric law becomes

$$\vec{D} = \epsilon \left(\vec{E} + iQ_v \vec{m} \times \vec{E} \right) \tag{7.37}$$

where $Q_v \vec{m}$ is the gyration vector, cf. [56] § 82.

The Kerr/Faraday Effect

Linearly polarized light that is deflected by a magneto-optical medium is usually elliptically polarized, cf. figure 7.8.

$$\Phi_k = \theta_k + i\,\eta_k; \quad \eta_k = \arctan\left(\frac{a}{b}\right) \tag{7.38}$$

Depending on the orientation of the magnetization with respect to the plane of incidence and the reflecting surface, three different Kerr effects are distinguished, cf. figure 7.9.

If the sample is magnetized out of plane, it is referred to as the *polar Kerr effect*. For an in-plane magnetized sample where in addition the magnetization is in the plane of incidence, the *longitudinal Kerr effect* is detected. Finally, if the sample is in-plane magnetized with the magnetization direction perpendicular to the plane of incidence, it is called the *transverse Kerr effect*. In the last case, the intensity instead of the ellipticity is influenced by the Kerr effect. Note, although the configuration for the transverse Kerr effect is the same as for the Voigt effect, both effects can be distinguished because the first one depends linearly and the second

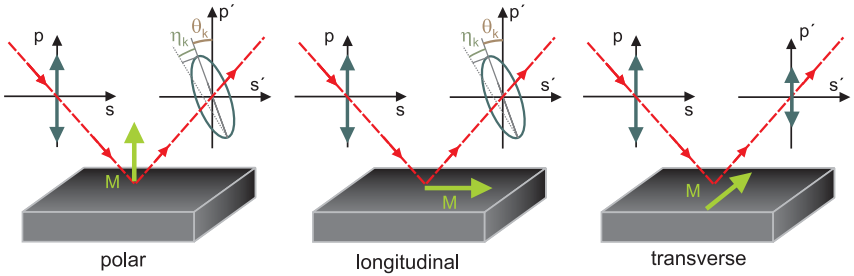

Figure 7.9.: Different configurations of the Kerr effect.

one quadratically on the magnetization.
While the Kerr effect is observed in reflection, the Faraday effect is observed in transmission in transparent media.
By taking the electromagnetic boundary condition at the interface between the magnetic medium and the non-magnetic medium into account, it is possible to relate the coefficients of the permittivity tensor 7.36 to the Kerr rotation 7.38. The calculations are rather complicated for an arbitrary geometry, cf. [102, 28].

The Kerr Effect in the Lorentz-Drude Model

Consider the classical oscillator model, cf. figure 7.2. If in addition a magnetic field is applied, it is necessary to extend the equation of motion 7.22 by a term $-e\,\partial_t \vec{r} \times \vec{B}$ describing the Lorentz force. As a result, an incoming electromagnetic wave, which stimulates a primary (linear) oscillation, also stimulates a secondary (linear) oscillation perpendicular to the first one. Consequently, the reflected wave is elliptically polarized. Confer to [43] chap. 2.3.2 for a detailed and illustrated discussion on the classical model.

Quantum-mechanical Interpretation of the Kerr Effect

The magneto-optical properties of many materials can be discussed by making use of the concepts and methods of the free ion theory, where the wave functions are localized and the inter-band transitions can be approximated by the transition between atomic energy levels, cf. [117] chap.

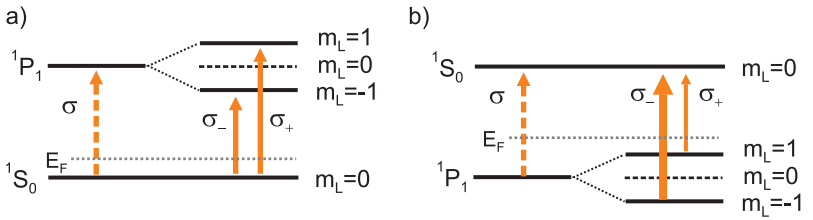

Figure 7.10.: Energy scheme of a $^1S_0 - ^1P_1$ transition: Kerr ellipticity of a) diamagnetic type b) paramagnetic type.

5. The splitting of the energy levels under the influence of the magnetic field or (more importantly) the magnetization, respectively, in combination with the selection rule $\Delta m = \pm 1$ give rise to a dichroism of circular polarized light.
Consider for instance the $^1S_0 - ^1P_1$ transition where an external magnetic field removes the degeneracy of the multiplet in M (Zeeman splitting), cf. figure 7.10 a. The frequency difference between the absorption line of left- and right-handed circularly polarized light induces circular dichroism. This is the so-called Kerr ellipticity of *diamagnetic* type.
In the second example, the degenerated level has a lower energy than the non-degenerated one. In this case the $m_L = 1$ and the $m_L = -1$ level have different populations and, although there is still a frequency difference between the absorption lines, the circular dichroism is dominated (according to Fermi's golden rule) by the different transition probabilities, cf. figure 7.10 b. This is the Kerr ellipticity of *paramagnetic* type.
In a ferromagnetic material, the exchange bias and the spin orbit coupling causes additional level-splitting that is stronger and consequently more relevant for the Kerr effect than the Zeeman-splitting, cf. [9, 102]. Confer also to [68] for an ab initio calculation of the magneto-optical Kerr effect of Fe and Ni.

Voigt Effect

The Voigt effect is detected in a configuration where the sample is magnetized perpendicular to the incoming light. In contrast to the Kerr effect, it depends quadratically on the magnetization components, cf. equation

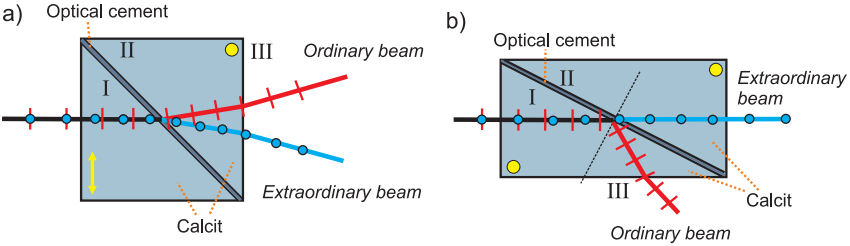

Figure 7.11.: Polarization Optics: The direction of the optical axis is indicated by a yellow point (direction out of image plane) or a double arrow. Refraction interfaces are denoted by Roman numerals. a) Wollaston prism b) Glan-Thomson prism.

7.36. Qualitatively, the Voigt effect can be explained by a stress-induced birefringence of linear polarized light created via magnetostriction, cf. [82].

7.2. Polarization Optics

A *Wollaston prism* consists of two birefringent calcite prisms, which are agglutinated with optical cement in a crossed configuration of the optical axes, cf. figure 7.11 a. The index of refraction of the optical cement lies between the one of calcite for extraordinary and ordinary polarization $n_{\mathrm{ex}} < n_{\mathrm{cement}} < n_{\mathrm{od}}$. Hence, according to Snell's law, the ordinary and the extraordinary beam are refracted in the opposite direction at the calcite-cement (I), cement-calict (II) and calcite-air interface (III). As a consequence the Wollaston prism divides an incoming beam into two linearly polarized beamlets with perpendicular directions of polarization.
A *Glan-Thomson prism* consists also of two cemented prisms, but in this case both optic axes are parallel to the adherend, cf. figure 7.11 b. The prism angle is chosen in such a way that, whereas the extraordinary beam passes unhindered, the ordinary beam is totally reflected at the calcite-cement interface (I), [7] chap. 4.7.

8. Discussion of the Design

8.1. Introduction

Actually, a scanning polarizing microscope (SPM) can be considered as a Kerr magnetometer that facilitates the possibility to move the light/laser probe over the sample and to map the Kerr signal into an image. Hence, there are at least as many different designs of an SPM as there are different ways to realize a Kerr magnetometer.
According to the way the Kerr angle and ellipticity are detected, it is possible to distinguish in principal two different design concepts: In the first one, the ellipticity of the incoming light is modulated (for instance by a Pockels cell or a Faraday modulator) and lock-in technique is used, cf. figure 8.1. By operating one lock-in amplifier at the modulation frequency and the other at twice the modulation frequency, the Kerr rotation and the Kerr ellipticty are detected simultaneously [81].
In the second design concept, the Kerr angle is detected via a cross-polarizer arrangement. This set-up requires a very intensity stable light-source, because the intensity fluctuations superimpose the Kerr signal [6]. By replacing the second polarizer with a polarizing beam splitter or a Wollaston prism, this problem can be overcome, cf. figure 8.2. If the difference of the two detector signals is divided by its sum, the intensity

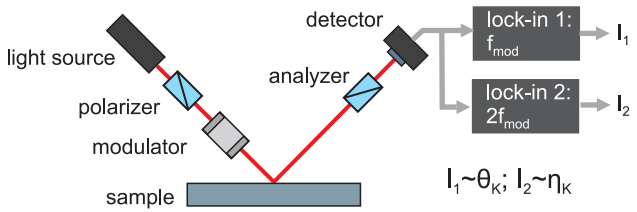

Figure 8.1.: Kerr magnetometer using a polarization modulator.

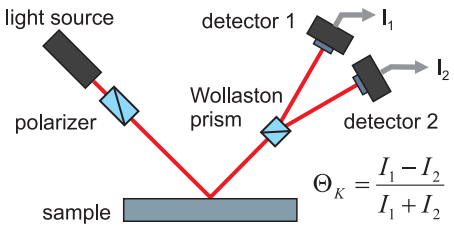

Figure 8.2.: Kerr magnetometer using differential technique: The Wollaston prism is oriented in such a way that for a vanishing Kerr angle, the same intensity reaches both detectors.

fluctuations are canceled [112]. In this arrangement the Kerr signal is proportional to the Kerr rotation. It is possible to detect in addition the Kerr ellipticity if a $\lambda/4$ wave plate is added.
An example for a SPM that uses the first detection scheme is [21], while the SPM described in [46] and the one of Clegg et al. [15, 16, 40] are examples for the latter.

8.2. Overview

A design with a differential detection scheme that is very similar as described by Clegg et al. [16] was chosen for the cryogenic scanning polarizing microscope (CSPM), because this design can be easily extended to LTSLM-voltage imaging, cf. figure 8.3. The main difference is that an opto-mechanical scanning mechanism is used in the new design.
The light source is a laser-diode with a wave-length of 405 nm. It is placed in a separate module. The light is transferred to the SPM via a single-mode fiber. After the beam expander, the plane of polarization is defined with a Glan-Thomson prism. A fast steering mirror is used as an opto-mechanical scanner. Via a transfer optic (Keplerian telescope) the mirror is imaged on the back focal plane of the infinity-corrected objective lens. Note that one lens of the transfer optic serves also as a cryostat window. The sample is mounted on the cold finger of a continuous-flow cryostat, cf. section 3.2.1 for a detailed description.
The light-intensity that is reflected by the sample passes the fast steering mirror and is deflected by a polarization-maintaining beam splitter. The $\lambda/4$ wave plate is used to correct the beam ellipticity and to enhance the contrast. With the help of the $\lambda/2$ wave plate, the plane of polarization

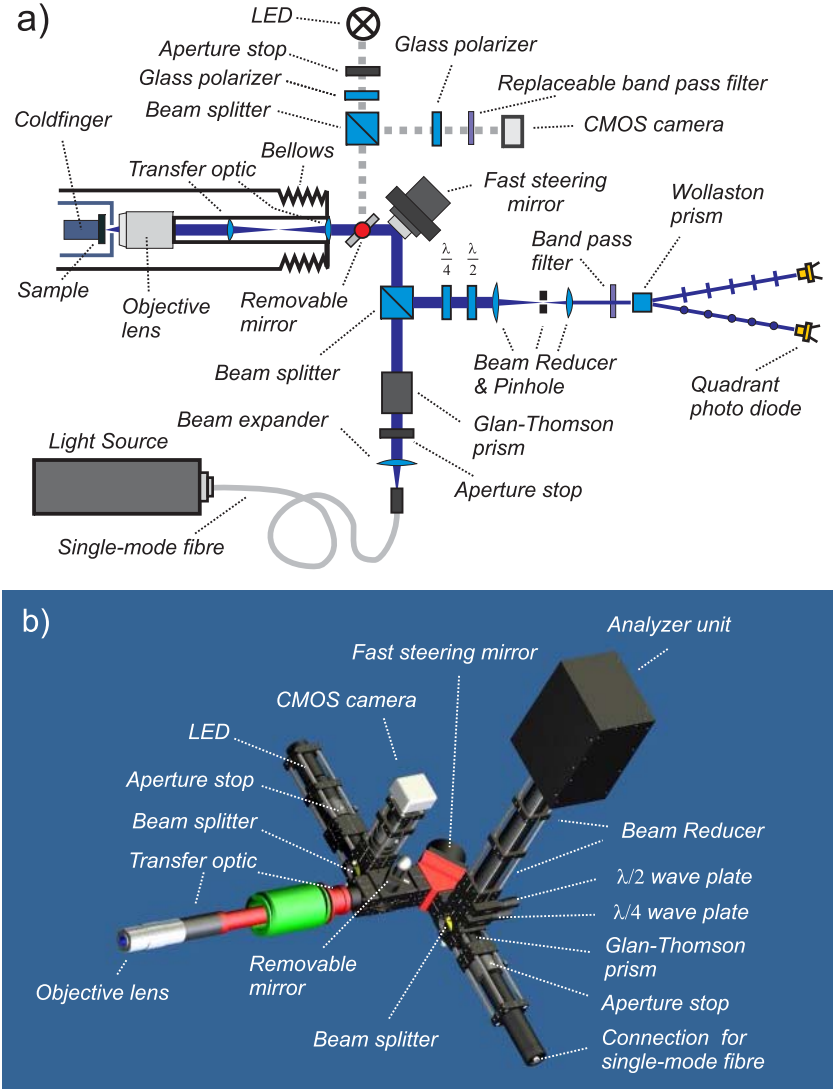

Figure 8.3.: a) Scheme of the cryogenic scanning polarizing microscope (CSPM); b) Autodesk Inventor image of the SPM (continuous flow-cryostat, positioning unit, and light-source not depicted).

can be rotated for zero balancing the Kerr signal. The beam diameter is reduced with another Keplerian telescope. The pin hole serves as a spatial filter, which prevents disturbing reflections from entering the detector, and makes the microscope confocal. In front of the Wollaston prism is an optical band-pass filter with a center wave-length corresponding to the laser diode. The beamlets are detected by two quadrant photo diodes.
There is the possibility to position an aperture stop in front of the Glan-Thomson polarizer and to restrict the illumination of the sample.
By placing the removable mirror into the optical path, the system can operate as a conventional microscope with an LED for illumination and a CMOS camera as detector. This is very helpful for focusing and choosing the field of view. The two glass polarizers facilitate conventional polarization microscopy and the replaceable band-pass filter can be used to restrict the optical band-width of the microscope. With the help of the aperture stop, which is imaged on the back focal plane of the objective lens, the polarization contrast is improved, cf. [43] chap. 2.3.6.
Mainly mechanical components from the Mikrobank system of Linos in combination with C30-Tubes are used. This way the optical path is sealed light-tight and the sensitive optical components are protected against dust. The laser safety of the system is also improved.

8.3. Light-Source

Using a separate light-source module helps to keep the SPM compact. A diode laser is chosen because it can be easily amplitude modulated via the bias current. Note that amplitude modulation is necessary for the LTSLM imaging described in section 3.2. For high resolution, the laser diode has a wave-length of 405 nm. The operating temperature of the laser diode is not actively stabilized. Hence, the system needs a certain time for warming up and reaching a stable operation temperature. With the help of a beam shaper, the coupling to the optical fiber is optimized. If it proves necessary, an optical isolator can easily be added to the light-source. The light is transferred with a polarization-maintaining single-mode fiber to the SPM.

8.4. Scanner

In scanning laser microscopy, two different scanning mechanisms are distinguished in principal: The first mechanism is the mechanical scanning where the sample, the objective lens, or the complete microscope is repositioned either with a stepper or with a piezo drive.
The second mechanism is the opto-mechanical scanning. An optical component is moved, and as a consequence, the optical path of the system is manipulated in such a way that the laser probe changes its position. This is realized, for instance, by rotating a prismatic mirror or a Nipkov disc, or by moving the aperture of an optical fiber in the focal plane of a lens. Note that scanning mirrors like galvano scanners or fast steering mirrors are also opto-mechanical scanners.
For polarizing microscopy, mechanical scanners are preferred, because this scanning mechanism does not influence the polarization. Usually mechanical scanning is slow, but this disadvantage is accepted (especially in research). It is wise to choose a component that is not too heavy and can be moved easily for mechanical scanning. The sample, for instance, would be a good choice. If it is not possible to move the sample, then scanning with the objective lens might be a solution. There are plenty of positioning units on the market that are suitable for this application.
If the sample is mounted in a cryostat, mechanical scanning is difficult. Meanwhile, there are good cryogenic positioning units with a high resolution and an acceptable range available, but they are rather expensive. Scanning with the complete cryostat would be an option. Another solution is to scan with only the evaporator of a continuous-flow cryostat. This way the mass of the scanning object is not too heavy and the positioning units do not need to operate at cryogenic temperatures.
The author decided not to use mechanical scanning. The main reason was the concern that the control voltage of a piezo scanner might disturb the four-terminal sensing during voltage imaging. Also, electromagnetic shielding of the sample would be more difficult. Another reason was the cost of a reasonable mechanical scanner.
If opto-mechanical scanning is used, care must be taken to keep the influence of the scanner on the polarizing state as small as possible. A fiber scanner is the best solution in this case, because it does not influence the polarization at all [77], but in such arrangement it is not possible to image the longitudinal Kerr effect. A Nipkov disc scanner is too difficult to real-

ize in a non-commercial microscope. So, the last option that is left is the use of a scanning mirror: Ping et al. have discussed the problem of using a mirror in a scanning polarizing microscope in detail [78, 77]. Due to the Fresnel equations (cf. section 7.1.6), the polarization of a reflected beam is changed. An exception is a p- or s-polarized beam. Here, p- or s- stands for a beam linearly polarized in the plane of incidence, or perpendicularly polarized to the plane of incidence, respectively. Therefore, the polarizer (Glan-Thomson prism in this case) must be oriented in such a way that the beam is p- or s-polarized with respect to the scanning mirror.
Note that the beam is reflected twice by the scanning mirror, cf. figure 8.3, and at the second reflection the plane of polarization is rotated, by the Kerr angle of the sample. Hence, a systematic error is unavoidable. Ping et al. [77] showed that this error scales with the Kerr angle and that it is smaller than 10%, but they only discussed the case for tilting the mirror around a single axis. By recalculating the error of a two axes scanning mirror (like a fast steering mirror) it can be shown that the effect of the second scanning axis is negligible.

8.5. Objective Lens

An objective lens with a large working distance of 5.2 mm is used. It is crucial that the objective lens has a large working distance, because the IR shielding with a pinhole aperture is situated between the objective lens and the sample in order to reduce the thermal load. In addition there should be enough space above the sample for protruding bond wires. The objective lens has a numerical aperture of 0.75. Hence, the theoretical resolution of the microscope is

$$d_{\min} \approx \frac{0.6\,\lambda}{NA} = 324\,\mathrm{nm} \tag{8.1}$$

and in a confocal arrangement

$$d_{\min}^{\mathrm{cf}} \approx \frac{d_{\min}}{1.4} = 231\,\mathrm{nm} \tag{8.2}$$

A wave-length correction for 436-656 nm is stated by the manufacturer. This refers to the chromatic aberration. Because in the SPM the illumination is monochromatic, the objective lens should also perform at a wavelength of 405 nm.

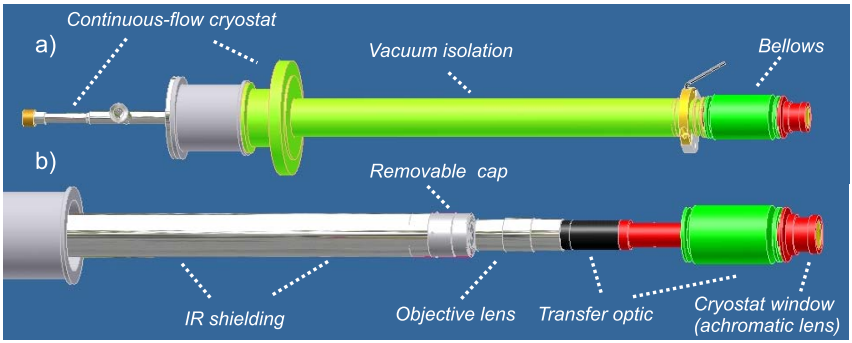

Figure 8.4.: a) Autodesk Inventor image of the continuous flow cryostat with the modification for the SPM; b) vacuum isolation removed.

8.6. Modified continuous-flow cryostat for the SPM

In order to situate the objective lens in the vacuum, it is necessary to modify the vacuum isolation and the IR shielding of the continuous-flow cryostat, cf. figure 8.4 a. A bellows facilitates moving the transfer optic and positioning the objective lens above the sample, cf. figure 8.4 b. Note also the modified IR shielding with a removable cap that allows for the positioning of a pinhole aperture with 1.5 mm diameter above the sample. This pinhole increases the thermal load to the sample by less than 1 mW due to IR radiation.

8.7. Analyzer Unit

The band-pass filter, the Wollaston prism, the two blue enhanced quad-cell silicon photodiodes, and the photo current amplifier are situated in a light-tight metallic casing. This way the electric lines are kept short and the Kerr signal is shielded against noise.
A single amplifier stage consisting of a low-noise operational amplifier is used to convert the small photo current into a voltage signal. It is nec-

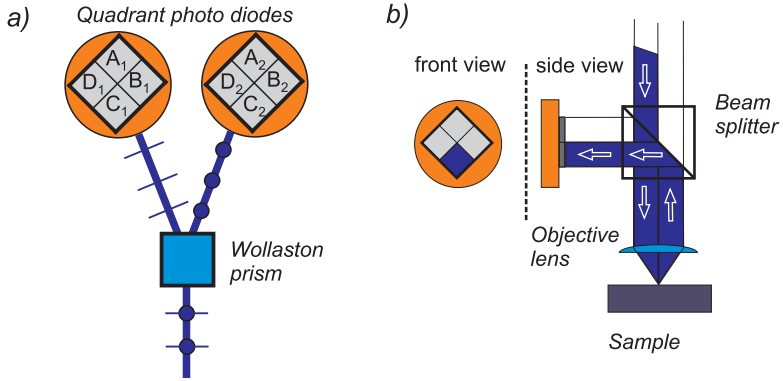

Figure 8.5.: Selecting the illumination angle and direction using quadrant photo diodes: a) Scheme of the detector arrangement b) Scheme of the SPM reduced to the essential, in order to illustrate the illumination of the sample if only one quadrant is read out

essary to restrict the bandwidth of this circuit to 2 kHz in order to avoid positive feedback. If lock-in technique is used for imaging, the lock-in frequency should be considerably larger than the inverse of the residence time per pixel. A lock-in frequency of 10 kHz is a realistic value. Hence, lock-in technique cannot be used in combination with this electronic. This is not considered as a major drawback, because Wrona et al. obtained good results with a differential Kerr magnetometer without using lock-in technique [112].

For perpendicular illumination, only the polar Kerr effect can be detected, and consequently (ignoring the Voigt effect for a moment) it is only possible to image the out-of-plane component of a magnetic structure, cf. section 7.1.7. Note that it is usually energetically favorable that thin films are in-plane magnetized. Clegg et al. [16] describe a detector arrangement with quadrant photo diodes that enables the imaging of the in-plane component in addition via the longitudinal Kerr effect. The signals of different quadrants correspond to different illumination directions, cf. figure 8.5. Processing these signals results in four different images, which can (in principle) be acquired simultaneously:

Reflected intensity (conventional image)

$$A_1 + B_1 + \cdots + D_1 + A_2 + B_2 + \cdots + D_2 \tag{8.3}$$

longitudinal Kerr effect (direction 1)

$$(A_1 - A_2) - (C_1 - C_2) \tag{8.4}$$

longitudinal Kerr effect (direction 2)

$$(B_1 - B_2) - (D_1 - D_2) \tag{8.5}$$

and polar Kerr effect

$$(A_1 - A_2) + (B_1 - B_2) + (C_1 - C_2) + (D_1 - D_2) \tag{8.6}$$

Note that in order to cancel the intensity fluctuation of the light source it is necessary to divide the last three signals by the first (sum) signal. An electronic circuit was designed to perform the preceding calculations. For the difference $A_1 - A_2$, $B_1 - B_2$, etc., a monolithic differential amplifier with a high common-mode rejection is used. This circuit is also situated in the metallic casing of the analyzer unit. The amplification of the differential amplifiers can be chosen via a selector switch. This way the sensitivity of the electronic can be adjusted to the Kerr signal. An external 20 V lead storage battery serves as power supply.

8.8. Controlling the SPM

For acquiring the four signals (equations 8.3-8.6) and controlling the position of the fast steering mirror, a usual National Instruments PCI-6221 AD/DA- converter is used. The images are recorded by a simple Labview program. The programming of the real-time control was quite laborious and the program is not very stable, because it was difficult to synchronize the input and output signals. Therefore, it makes sense to use a real time computer system like ADWinPro in the future.

8.9. Removable Mirror

In order to switch into the camera mode for selecting the field of view and focusing, a removable mirror was designed that is compatible to the Linos

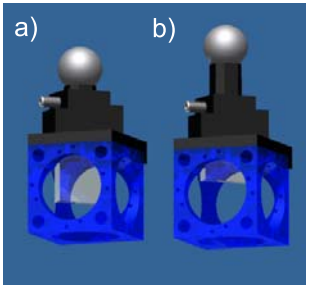

Figure 8.6.: Removable mirror with prismatic guide in a Linos Mikrobank cube: a) down position b) up position

Mikrobank system, cf. figure 8.6. This way the use of an additional beam splitter, which might disturb the polarization and causes considerable loss of laser intensity in the SPM mode, can be avoided.

8.10. Mechanical Supports & Positioning Unit

The SPM should be integrated in the set-up of the LTSLM described in section 3.2. In particular, it should be possible to use the already-existing magnets, namely a 5 Tesla (out-of-plane) superconducting magnet, a 500 mT in-plane and 150 mT out-of-plane electro-magnet, and a 150 mT rotatable magnet with in-plane field.
As a consequence the sample is mounted vertically. This has the disadvantage that it is impossible to put a magneto-optic-sensitive crystal on top of the sample without any holder, as is usually done for magneto-optical imaging by some research groups.
Confer to figure 8.4 to get an impression of the leverage that is exerted on the continuous-flow cryostat cold finger and on the transfer optic. Hence, in order to obtain a maximum resolution of 230 nm, well-designed mechanical supports and a good vibration isolation are absolutely necessary. The 5 Tesla superconducting magnet is supported by dampers for vibration isolation. Because the mechanical supports are part of the magnet cryostat, they cannot be improved easily in this case.
But the supports of the configuration with the electro magnets have been redesigned, cf. figure 8.7. They are assembled from custom-tailored aluminum sheets that can be easily machined by the workshop. The design was optimized using the FEM-based stress analysis module of Autodesk

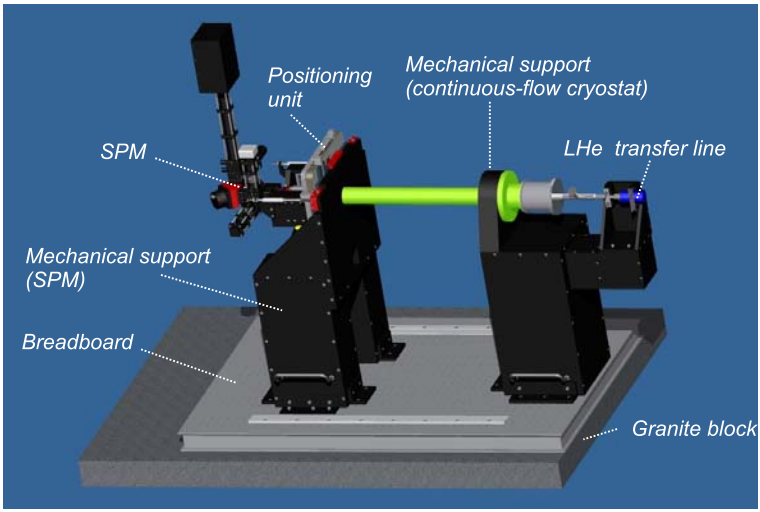

Figure 8.7.: Autodesk Inventor image of the SPM set-up

Inventor. The supports are connected to a usual optical breadboard, which is supported by damping cushions on a granite block. In order to prevent the transmission of any vibration from the LHe transfer line to the cold finger, it is firmly connected to the support of the continuous-flow cryostat.

For focusing and selecting the field of view, a positioning unit is needed, which allows for the translation of the SPM in all three spatial directions. The depth of focus is about 0.5 μm and the resolution of the focusing translation should be the same. A confocal microscope has a high depth discrimination, because the pin hole aperture in front of the detector blocks all the light that does not originate from the focal plane of the objective lens. This has the effect that if the sample is tilted by just a small angle, only a stripe in the middle of the sample can be imaged, because the other parts are out of focus. Therefore, in order to correct for any misalignment of the sample, it would be helpful if the positioning unit also could tilt the optical axis of the microscope, cf. [111] chap. 5. Although there are plenty of translation stages, goniometers, and positioning units on the market,

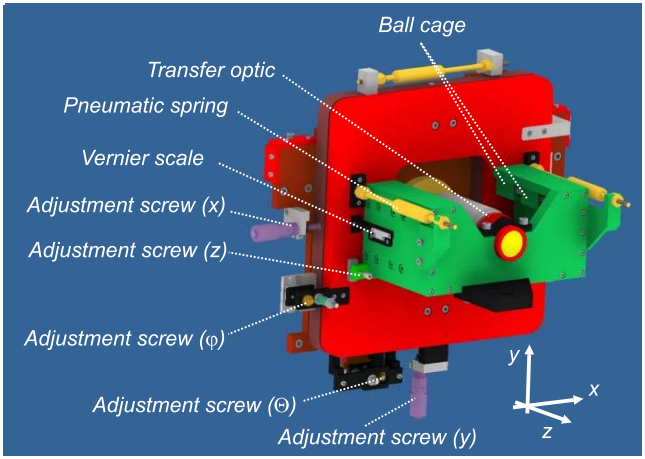

Figure 8.8.: Autodesk Inventor image of the positioning unit

it is very difficult to assemble a solution that allows for the adjustment of such a bulky object, with the additional problem that the bellows of the vacuum isolation is exerting a force of about 200 N in focusing direction.

The author decided to design a positioning unit that is assembled mainly of aluminum sheets and profiles, and that uses ball cage guiding on steel shafts for translation and rotation, cf. figure 8.8. The unit is driven manually via adjustment screws.

The translation stage for the focusing direction (z-direction) resembles a drawer that runs on four steel shafts, cf. figure 8.8 and 8.9. Both the transfer optic and the other part of the SPM are firmly connected to the drawer. Two pneumatic springs on both sides reduce the force that is exerted on the adjustment screw by the vacuum via the bellows. A vernier scale simplifies focusing.

The other four degrees of freedom are realized in one gimbal, cf. figure 8.9. A special ball cage guiding is used that allows for translation and rotation. The supporting points that restrict the angular degrees of freedom are guided by two small linear translation stages. Two disc spring assemblies push the adjustment screws for the angular degrees of freedom against these translation stages. The weight force of the SPM is

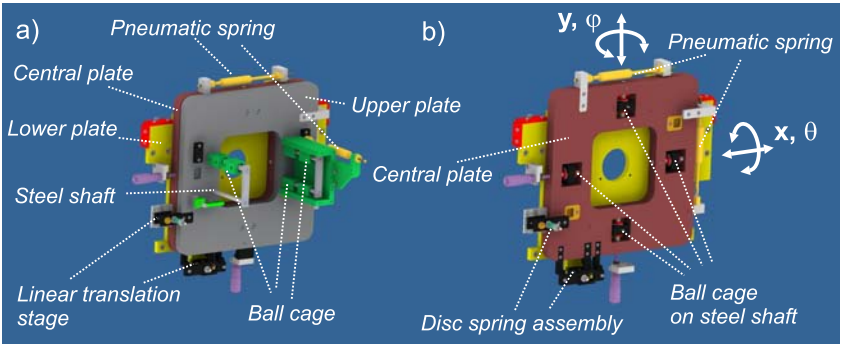

Figure 8.9.: Details of the positioning unit: a) Parts of the z-translation stage removed in order to provide a view on the ball cages and the steel shafts. b) Upper plate removed to reveal the view on the gimbal.

compensated by an additional pneumatic spring.

9. Tests & First Results

9.1. Kerr Magnetometer

In order to test the light-source and the components for the polarization optics, a Kerr magnetometer was realized. Additionally, first experience should be gained with the photo-current amplifier electronics. A configuration with perpendicular illumination that enables the detection of the polar Kerr effect was chosen. This way the e-magnet of a labcourse experiment could be used [100]. A CoPt-multilayer (that is also part of the same labcourse experiment) with an out-of-plane magnetization due to interface anisotropy was the test sample.
The magnetometer was build on a $60\,\mathrm{cm} \times 90\,\mathrm{cm}$ solid aluminum breadboard surrounded by an approximately 40 cm-high hardboard frame, which can be covered by a Perspex sheet to protect the optical components against dust, cf. figure 9.1. Confer also to figure 9.2, where the light-source module is depicted from a better perspective. The collimated beam emitted by the laser diode passes a Keplerian telescope with cylindrical lenses serving as beam shaper, which converts the elliptical beam profile into a more or less circular one. A fiber coupler and a single-mode fiber are used to transfer the light-intensity to the magnetometer. Even if the system is aligned carefully, only 18 % of the laser intensity (corresponds to 3.7 mW) can be detected at the other end of the fiber. A single achromatic lens is used as a beam expander. The laser beam is polarized via a Glan-Thomson prism, passes a beam splitter and is reflected by the CoPt-multilayer. With the $\lambda/4$ wave plate, the ellipticity is corrected and the plane of polarization is rotated by the $\lambda/2$ wave plate, so that at zero balance the same light-intensity reaches the two photo diodes after the beam was divided into two beamlets with perpendicular polarization via the Wollaston prism. Light from sources other than the laser diode is mostly blocked by the band-pass filters in front of the photo diodes. The photo-current amplifier was realized on an electronic test breadboard. This way

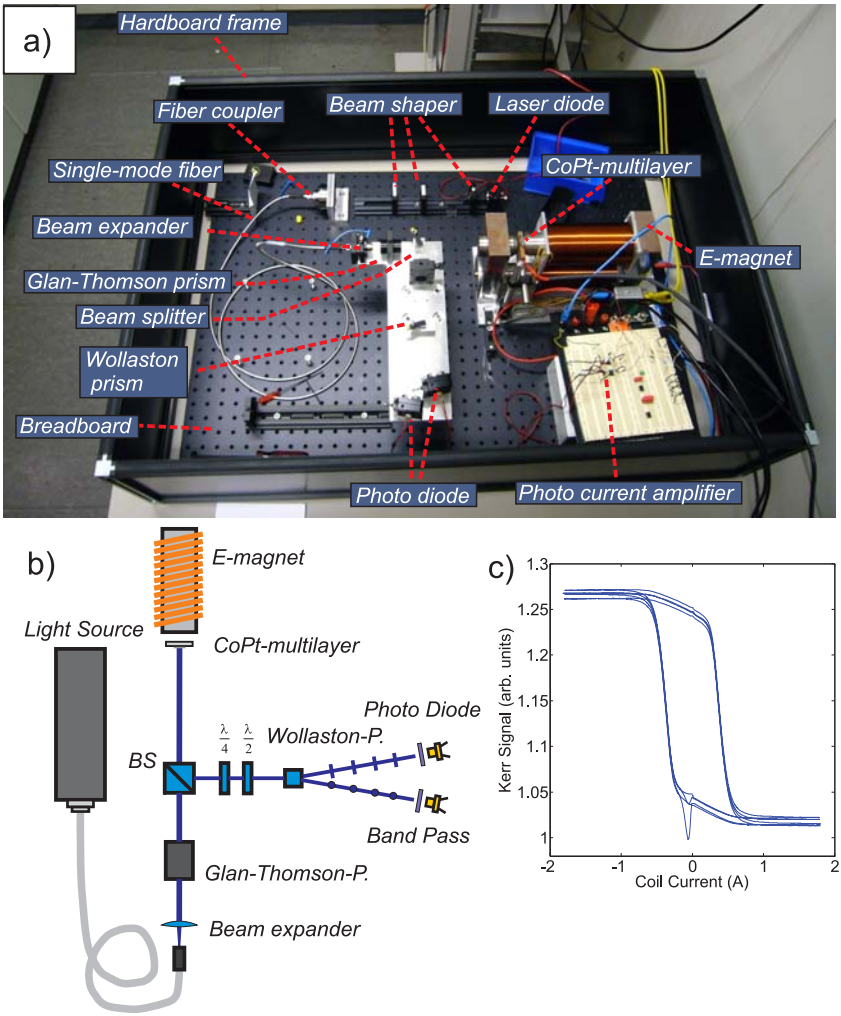

Figure 9.1.: Kerr magnetometer: a) photograph b) Scheme c) Kerr signal of a CoPt-multilayer.

the circuit could be modified easily, but it had the disadvantage that external noise was not shielded very well. In this magnetometer the Kerr signal is proportional to the difference of the photo currents I_1 and I_2. In order to compensate intensity fluctuations of the light-source, the signal is normalized by the sum.

$$K_s = \frac{I_1 - I_2}{I_1 + I_2} = \frac{\text{Diff}}{\text{Sum}} \tag{9.1}$$

A usual transimpedance amplifier is used to convert the photo currents into a voltage signal. From these voltage signals, the difference (Diff) and sum (Sum) signal was formed. The Diff and Sum signals were acquired by an AD converter and the Kerr signal was calculated via a PC. In figure 9.1 c, a typical magnetization curve of the CoPt-multilayer is depicted. Note that in this case two lock-in amplifiers had been used to reduce the influence of external noise.

9.2. Test set-up for room-temperature imaging (polar Kerr effect)

The second test set-up was a scanning polarizing microscope (SPM) with a detector configuration identical to the one described in the preceding section 9.1. The main objective of this set-up was to test the fast steering mirror and the conventional optical imaging. Also experience should be gained in the polar Kerr microscopy. The test set-up was already very similar to the final SPM except that it was designed for room-temperature imaging. Confer to figure 8.3 for a scheme of the microscope and to figure 9.2 for a photograph of the set-up. Note that the sample was mounted on a xyz-translation stage for focusing and selecting the field of view.
The signal processing was already described in the preceding section 9.1. In this case lock-in technique was not used and the data were acquired by an ADWinPro-system. The ADWinPro real-time computer was also controlling the fast steering mirror.
A thin film structure was the test sample for optical imaging. For comparison, a conventional microscope image is depicted in figure 9.3 a. Figure 9.3 b is an SPM image of another part of the sample. Note the improved contrast and the better signal-to-noise ratio. In order to determine the maximum resolution of the SPM via edge signals, a linescan had been

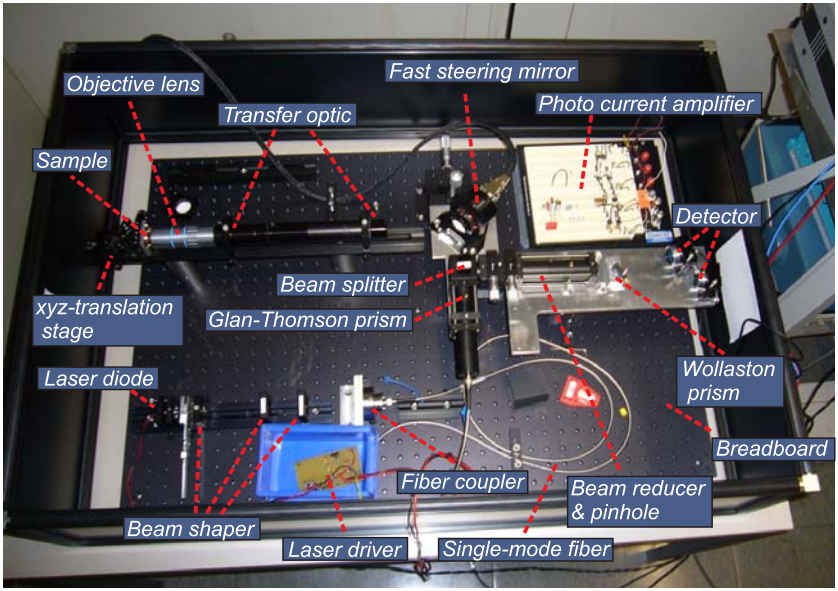

Figure 9.2.: Test set-up for room temperature imaging (polar Kerr effect).

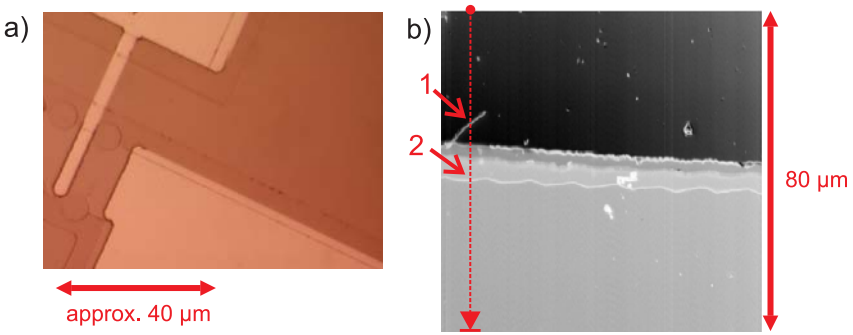

Figure 9.3.: a) conventional microscope image of a thin film structure: An objective lens with a numerical aperture of 0.7 was chosen. b) optical SPM image: The path of the linescan in figure 9.4 is indicated by a red dashed line. The red arrows mark the edges that were used to determine the resolution.

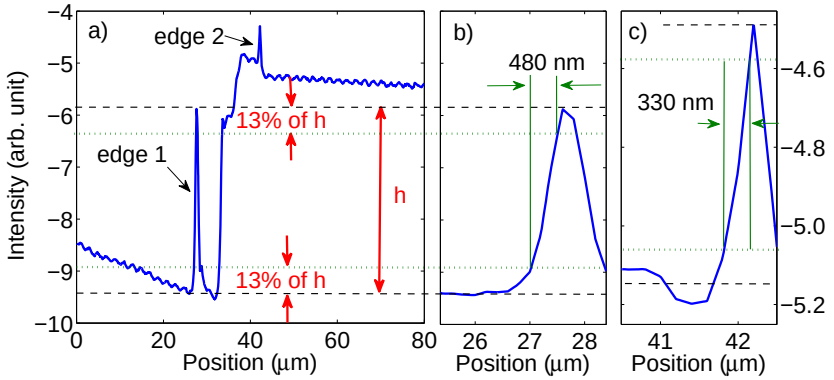

Figure 9.4.: a) Linescan extracted from the optical SPM image figure 9.3 b: The resolution of the microscope was determined by subtracting 13% of the edge signal height from the top and the bottom and by determining the difference in the abscissa values. b) Zoom on edge 1; c) Zoom on edge 2.

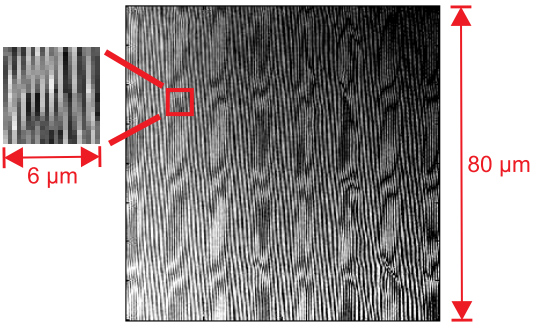

Figure 9.5.: SPM polar Kerr effect-image of a magneto-optical disc (MOD): The pixel size is 200 nm.

extracted. According to equation 8.1 and figure 9.4 the maximum resolution of 330 nm is near the theoretical value and consequently the optical components chosen work sufficiently.
The test sample for the polar Kerr effect imaging was a magnetooptical disk with a storage capacity of 1.3 GB. The bit size was roughly estimated to 1-3 μm^2 by dividing the active surface of the disc by the number of bits. Confer to figure 9.5 for an SPM image of the bit pattern.

9.3. The final version of the SPM

To test the final version of the SPM as it is described in section 8.2, a set-up for room-temperature imaging was realized again. This time the photo-current amplifier was fabricated by the electronic workshop and it was integrated in the analyzer unit described in section 8.7. For controlling and data acquisition a AD/DA converter was used, cf. section 8.8.
To test the Kerr microscopy, a special sample was prepared: A sheet of transformer steel was sanded using sandpapers with declining grain size and polished with "Mellerud Polierpaste, Edelstahl Chrom Aluminium" in order to obtain a mirror-like surface. The sample was marked with a black waterproof pen. This way, two areas with different optical properties were created, cf. figure 9.6.
During the testing following problems occurred: First, it was not possible to access the trimming resistor for balancing the monolithic differential amplifiers. Therefore, the Kerr signals could not be zero balanced simultaneously with the $\lambda/2$ wave plate. Second, because the pillar supporting the analyzer unit was mechanically unstable, it was impossible to use a pin hole in the beam reducer, and consequently, disturbing reflections could not be blanked out.
Nevertheless, it was possible to image domain structures in the transformer steel sheet, cf. figure 9.6.

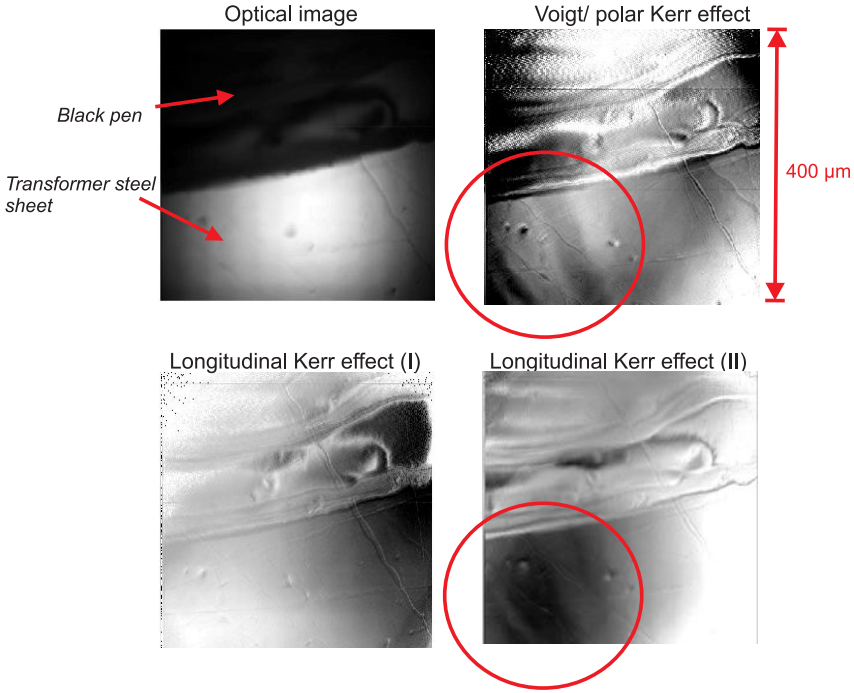

Figure 9.6.: SPM images of a transformer steel sheet. The pixel size was 1 μm. Magnetic domain structures can be seen in the lower left corner of the polar and longitudinal (II) Kerr images indicated by red circles.

10. Outlook

The cryogenic scanning polarizing microscope (CSPM) was not completed in the course of this thesis and further tests are necessary.
First, it should be investigated if the Kerr images can be improved using a pin hole in the beam reducer and if the resolution of the optical image can be increased by making the system confocal. It might be necessary to rework the analyzer pillar and the analyzer unit. In this connection, it makes sense to relocate the trimming resistor for balancing the differential amplifiers.
Second, the depolarizing effect of individual optical components like the objective lens or the fast steering mirror can be reduced significantly with a suitable aperture stop.
Third, in case it is not possible to acquire high-quality Kerr images, after the preceding measures have been taken, another objective lens that is optimized for polarization microscopy, should be tried. For the first tests, a cheap objective lens with a small numerical aperture and a small working distance would be sufficient.
Fourth, the influence of the scanning mirror on the Kerr signal should be investigated systematically. Note that a coated aluminum mirror is not ideal in terms of polarization microscopy, because of the significant difference in the s- and p-reflectivity. If the influence of the scanning mirror is too large, it might be necessary to replace the aluminum mirror in the fast steering mirror with a dielectric one. A suitable dielectric mirror has already been procured by the author.
After the tests have proven successful, an in-plane magnetized thin film sample should be investigated systematically. The response of the SPM to the longitudinal Kerr effect should be quantitatively compared to the Voigt effect. It might turn out that the Voigt effect is sufficient or even better for imaging the magnetic structure of an in-plane magnetized sample. This could simplify the set-up considerably.
The workshop has almost completed the mechanical supports and the positioning unit as of the completion of this thesis. Please note that in the

cryogenic set-up, it is absolutely necessary to protect the objective lens against mechanical stress by evacuating the continuous-flow cryostat very slowly.
Despite the teething problems, the author is confident that the CSPM will prove itself to be a powerful and versatile tool in cryogenic research.

A. Derivations & Calculations

A.1. Temporal change of the total energy of a long Josephson Junction

In [55] a Danish PhD thesis was cited for the following deviation. Because this citation could not be accessed, this step was calculated again by the author and is presented here for convenience:
A derivation for the temporal change of the total energy of a long Josephson Junction described by a perturbed sine-Godon equation is presented. The same notation as in [55] is used.
PSGE:

$$\phi_{\mathrm{xx}} - \phi_{\mathrm{tt}} - \sin\phi = \alpha\phi_t - \beta\phi_{\mathrm{xxt}} \tag{A.1}$$

boundary conditions:

$$\phi_x(0,t) + \beta\phi_{\mathrm{xt}}(0,t) = -\kappa + \eta \tag{A.2}$$

$$\phi_x(L,t) + \beta\phi_{\mathrm{xt}}(L,t) = \kappa + \eta \tag{A.3}$$

The full energy of the SG wave field is given by (cf. [4, p. 269]):

$$H = \int_{-\infty}^{\infty} dx \left[\frac{1}{2}\phi_t^2 + \frac{1}{2}\phi_x^2 + (1-\cos\phi)\right] \tag{A.4}$$

$$\Rightarrow \frac{dH}{dt} = \int_0^L dx \left[\phi_t\phi_{\mathrm{tt}} + \phi_x\phi_{\mathrm{xt}} + \sin\phi\,\phi_t\right] \tag{A.5}$$

Equation A.1 in A.5

$$\frac{dH}{dt} = \int_0^L dx \left[\phi_t\phi_{\mathrm{xx}} - \alpha\phi_t^2 + \beta\phi_t\phi_{\mathrm{xxt}} + \phi_x\phi_{\mathrm{xt}}\right] \tag{A.6}$$

and

$$\partial_x\left[\phi_t\phi_x\right] = \phi_t\phi_{\mathrm{xx}} + \phi_{xt}\phi_x \tag{A.7}$$

$$\Rightarrow \frac{dH}{dt} = \int_0^L dx \left[-\alpha\phi_t^2 + \beta\phi_t\phi_{\mathrm{xxt}}\right] \quad + \quad [\phi_t\phi_x]_0^L \tag{A.8}$$

$$\begin{aligned} &= \int_0^L dx \left[-\alpha\phi_t^2 + \beta\phi_t\phi_{\mathrm{xxt}}\right] \\ &\quad + \eta\left(\phi_t(L) - \phi_t(0)\right) + \kappa\left(\phi_t(L) + \phi_t(0)\right) - \beta\left[\phi_t\phi_{xt}\right]_0^L \end{aligned} \tag{A.9}$$

Integration by parts

$$\int dx\, \phi_{\mathrm{xt}}\phi_{\mathrm{xt}} = [\phi_t\phi_{\mathrm{xt}}] - \int dx\, \phi_t\phi_{\mathrm{xxt}} \tag{A.10}$$

$$\begin{aligned} \frac{dH}{dt} &= \int_0^L dx\, \left[-\alpha\phi_t^2 - \beta\phi_{\mathrm{xt}}^2\right] \\ &\quad + \eta\left(\phi_t(L) - \phi_t(0)\right) + \kappa\left(\phi_t(L) + \phi_t(0)\right) \end{aligned} \tag{A.11}$$

A.2. LTSLM voltage-response of an electro-thermal domain wall

In this section, the low-temperature scanning laser microscope (LTSLM) voltage response in a BSCCO mesa, with the laser probe position in the middle of an electro-thermal domain wall (ETDW), is estimated using a simple model. The mesa is divided into four areas, the two electro-thermal domains, the electro-thermal domain wall, and the area that is heated by the laser probe. Any area corresponds to an electric conductance and the response is calculated by considering a parallel circuit of these conductors. A quasi one-dimensional temperature distribution in the mesa is assumed. Two electro-thermal domains, one at a temperature of T_1 and the other at a temperature of T_2 (hot spot), are separated by a transition region (ETDW), cf. figure A.1 a). The conductivities σ_1 and σ_2 correspond to the temperatures T_1 and T_2, cf. figure A.1 b). w and l are the width and the length of the mesa. x and l_{dw} are the length of the hot spot and of the ETDW, respectively. For simplicity an effective mesa and an effective hot spot length are defined, $\tilde{l} \equiv l - l_{dw}$, $\tilde{x} \equiv \frac{x}{\tilde{l}}$. It is assumed that the laser beam creates a temperature rise ΔT in an area ΔA and consequently the conductivity increases from α_0 to α_1. The voltage response can be calculated by considering an equivalent parallel circuit consisting of a shunt resistor with a conductance of Σ_s (cf. figure 3.4), and additional

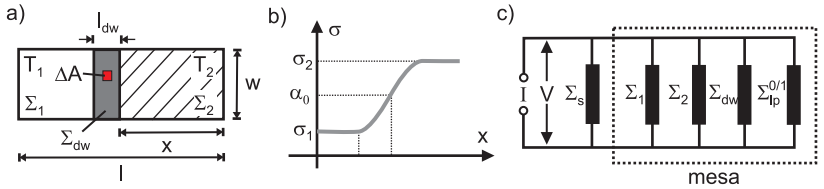

Figure A.1.: Voltage response of an electro-thermal domain wall (ETDW): a) Sketch of BSCCO mesa (top view) with quasi one-dimensional temperature distribution (l, length and w, width). The hot spot is at the right (hatched rectangle) and the dark rectangle in the middle denotes the ETDW. The red square corresponds to the laser probe with an area of ΔA. b) Conductivity distribution in the mesa along the x-direction: σ_1 and σ_2 denote the conductivity of the two electro-thermal domains. In the vicinity of the laser probe, a homogenous conductivity distribution is assumed of α_0 and α_1 for laser off and laser on, respectively. c) Equivalent circuit of the transport measurement in the LTSLM set-up. Confer to figure a) for the notation of the conductance. In addition, Σ_s and $\Sigma_{lp}^{0/1}$ denote the conductance of the shunt resistor and the laser probe.

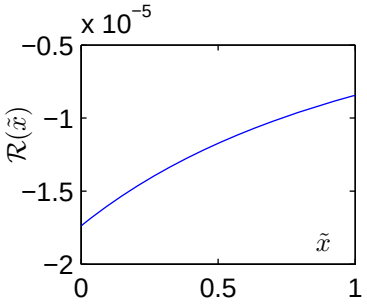

Figure A.2.: Response difference $\Delta\mathcal{R}$ vs. hot spot length $\tilde{x}$ with $\sigma_1 = 0.5$, $\sigma_2 = 1.0$, $\alpha_0 = 0.7$, $\alpha_1 = 0.75$, $\tilde{l}_{dw} = 0.2$, $\tilde{\Sigma}_S = 0.5$ and $\Delta a = 4.6e-4$.

resistors with the conductance $\Sigma_1(\tilde{x}), \Sigma_2(\tilde{x}), \Sigma_{dw}$ and $\Sigma_{lp}^{0/1}$ corresponding to the cold area, hot spot, ETDW and laser probe, respectively, cf. figure A.1.

It follows from the definition of the conductance and the geometry of the problem that

$$\Sigma_1 = \frac{\sigma_1(1-\tilde{x})\, w\tilde{l}}{d}, \quad \Sigma_2 = \frac{\sigma_2\, \tilde{x}\, w\tilde{l}}{d}, \quad \Sigma_{lp}^{0/1} = \alpha_{0/1}\frac{\Delta A}{d} \tag{A.12}$$

where d is the mesa thickness. Assuming a linear dependence of the conductivity vs. temperature in the interval $[T_1, T_2]$, the conductance of the ETDW can be estimated

$$\Sigma_{dw} = \frac{1}{2}\,(\sigma_1 + \sigma_2)\,\frac{\tilde{l}_{dw}\, w}{d}\,\tilde{l}, \quad \tilde{l}_{dw} \equiv \frac{l_{dw}}{\tilde{l}} \tag{A.13}$$

It is convenient to define the relative area of the laser probe and to express the conductance of the shunt resistor in geometric units of the mesa

$$\Delta a \equiv \frac{\Delta A}{w\,\tilde{l}}, \quad \widetilde{\Sigma}_S \equiv \frac{\Sigma_S\, d}{w\,\tilde{l}} \tag{A.14}$$

Applying Ohm's law and using the preceding equations, the response of the transport measurement for laser off and laser on in geometric units of the mesa is obtained

$$\mathcal{R}_{0/1} \equiv \frac{V_{0/1} w\tilde{l}}{I\, d} = \left[\mathcal{S}(\tilde{x}) + \alpha_{0/1}\Delta a\right]^{-1} \tag{A.15}$$

with

$$\mathcal{S}(\tilde{x}) \equiv (\sigma_2 - \sigma_1)\tilde{x} + \sigma_1 + \widetilde{\Sigma}_S + \frac{1}{2}(\sigma_1 + \sigma_2)\tilde{l}_{dw} \tag{A.16}$$

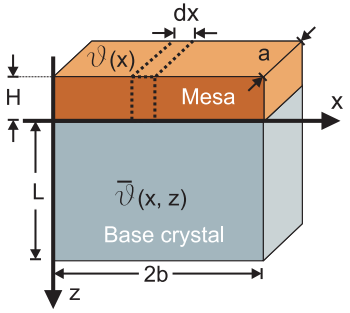

Figure A.3.: A narrow mesa on a base crystal with the same lateral dimensions: Apart from the bottom surface of the base crystal, which is in contact with a thermal bath, all surfaces are thermally isolating. A uniform temperature distribution along the width is assumed. Because the mesa is much thinner than the base crystal any temperature variation in the mesa along the z-axis shall be ignored.

and the response difference is

$$\Delta\mathcal{R} \equiv \mathcal{R}_1 - \mathcal{R}_0 \approx \frac{-(\alpha_1 - \alpha_0)\Delta a}{\mathcal{S}(\tilde{x})^2 + \mathcal{S}(\tilde{x})(\alpha_1 + \alpha_0)\Delta a} \tag{A.17}$$

According to the plot of $\Delta\mathcal{R}(\tilde{x})$, the LTSLM voltage response declines for increasing hot spot size, cf. figure A.2.

A.3. The branching temperature for a narrow mesa on a base crystal with the same lateral dimensions

The derivation in this section is analog to the one of Spenke in [89] for a disc shaped NTC. The heat transport equations in the mesa and the base crystal lead to a set of two coupled differential equations and the corresponding boundary conditions. In order to find the branching temperature, only small perturbations are considered and the temperature for which a non trivial (i.e. non constant) perturbation exists is calculated. But first the trivial solution with a homogeneous temperature distribution in the mesa is discussed: The temperature is T, and T_0 is the base temperature. If $\vartheta \equiv T - T_0$ is the excess temperature of the mesa then the excess temperature distribution in the base crystal is $\bar{\vartheta}(z) = \vartheta\frac{L-z}{L}$. Applying Ohm's law and Newton's law of cooling leads to $U^2 = A(\vartheta)R(\vartheta)$ with the heat flow coefficient $A(\vartheta) = \kappa_c\frac{2ba}{L}\vartheta$ and the resistance $R(\vartheta) = \frac{H}{2ba}\rho(\vartheta)$.

Hence,

$$U^2 = \kappa_c \frac{H}{L} \rho(\vartheta)\vartheta \tag{A.18}$$

By considering the Joule heating in and the heat flow into a infinitesimal small element of the mesa, the following differential equation for the excess temperature distribution can be derived, cf. figure A.3 and [89]:

$$\kappa_{ab}\, H\, \partial_x^2 \vartheta(x) + \kappa_c\, \partial_z \bar{\vartheta}(x,z)\big|_{z=0} + \frac{U^2}{\rho H} = 0 \tag{A.19}$$

The excess temperature in the base crystal is given by

$$\kappa_{ab}\partial_x^2 \bar{\vartheta}(x,z) + \kappa_c \partial_z^2 \bar{\vartheta}(x,z) = 0 \tag{A.20}$$

The boundary conditions are

$$\partial_x \vartheta|_{x=0} = \partial_x \vartheta|_{x=2b} = 0 \tag{A.21}$$

$$\partial_x \bar{\vartheta}\big|_{x=0} = \partial_x \bar{\vartheta}\big|_{x=2b} = 0 \quad \text{(no heat flow across the edges)} \tag{A.22}$$

$$\bar{\vartheta}\big|_{z=L} = 0 \quad \text{(cooling at the bottom)} \tag{A.23}$$

$$\vartheta(x) = \bar{\vartheta}(x,z)\big|_{z=0} \quad \text{(continuity at the interface)} \tag{A.24}$$

Only small perturbations are considered

$$\vartheta(x) = \vartheta_0 + \chi(X) \tag{A.25}$$

$$\bar{\vartheta}(x) = \vartheta_0 \frac{L-z}{L} + \bar{\chi}(x,z) \tag{A.26}$$

This results into a new set of coupled differential equations (using equation A.18)

$$\kappa_{ab} H \partial_x^2 \chi(x) + \kappa_c \partial_z \bar{\chi}(x,z)|_{z=0} - \frac{\partial_\vartheta \rho(\vartheta)|_{\vartheta=\vartheta_0}}{\rho(\vartheta_0)} \vartheta_0 \frac{\kappa_c}{L} \chi(x) = 0 \tag{A.27}$$

$$\kappa_{ab}\partial_x^2 \bar{\chi}(x,z) + \kappa_c \partial_z^2 \bar{\chi}(x,z) = 0 \tag{A.28}$$

and new boundary conditions

$$\partial_x \chi|_{x=0} = \partial_x \chi|_{x=2b} = 0 \tag{A.29}$$

$$\partial_x \bar{\chi}|_{x=0} = \partial_x \bar{\chi}|_{x=2b} = 0 \quad \text{(no heat flow across the edges)} \tag{A.30}$$

$$\bar{\chi}|_{z=L} = 0 \quad \text{(cooling at the bottom)} \tag{A.31}$$

$$\chi(x) = \bar{\chi}(x,z)|_{z=0} \quad \text{(continuity at the interface)} \tag{A.32}$$

It can be shown that the following "Ansatz" solves the differential equations and satisfies the corresponding boundary conditions:

$$\chi_n(x) = C\cos\left(\frac{\pi\, n}{b}x\right) \tag{A.33}$$

$$\bar{\chi}_n(x,z) = C\cos\left(\frac{\pi\, n}{b}x\right)\frac{\sinh\left(\frac{\pi\, n}{b}\sqrt{\frac{\kappa_{ab}}{\kappa_c}}(L-z)\right)}{\sinh\left(\frac{\pi\, n}{b}\sqrt{\frac{\kappa_{ab}}{\kappa_c}}L\right)} \tag{A.34}$$

To proceed further, it shall be assumed that the temperature dependence of the resistivity can be approximated by an exponential law $\exp(-\alpha\vartheta)$, where α is the inverse of the excess temperature $\widetilde{\vartheta}$ corresponding to the outermost point at the knee of the IV.
Inserting the solution into the equation A.28 implies

$$-\kappa_{ab}H\frac{n^2\pi^2}{b^2} - \kappa_c\frac{n\pi}{b}\sqrt{\frac{\kappa_{ab}}{\kappa_c}}\coth\left(n\pi\sqrt{\frac{\kappa_{ab}}{\kappa_c}}\,\frac{L}{b}\right) + \vartheta\frac{\alpha\kappa_c}{L} = 0 \tag{A.35}$$

The index $n = 1$ denotes the smallest "Eigenwert", which also defines the branching temperature:

$$\vartheta^* = \widetilde{\vartheta}\left[\frac{\kappa_{ab}}{\kappa_c}\frac{\pi^2 H\, L}{b^2} + \pi\sqrt{\frac{\kappa_{ab}}{\kappa_c}}\frac{L}{b}\coth\left(\pi\sqrt{\frac{\kappa_{ab}}{\kappa_c}}\,\frac{L}{b}\right)\right] \tag{A.36}$$

Bibliography

[1] C. Allgeier and J.S. Schilling. Correlation between the magnitude of the superconducting transition temperature and the normal-state magnetic susceptibility in $Bi_2Sr_2CaCu_2O_{8+y}$ and $Ti_2Ba_2CuO_{6+y}$ as a function of oxygen content. *Physica C: Superconductivity*, 168(5-6):499 – 505, 1990.

[2] R. Atkinson and P.H. Lissberger. Sign conventions in magneto-optical calculations and measurements. *Applied Optics*, 31:6076, 1992.

[3] A. Barone, W. J. Johnson, and R. Vaglio. Current flow in large Josephson junctions. *J. Appl. Phys.*, 46:3628, 1975.

[4] A. Barone and G. Paterno. *Physics and Applications of the Josephson Effect*. Wiley-VCH, 1982.

[5] I. E. Batov, X. Y. Jin, S. V. Shitov, Y. Koval, P. Müller, and A. V. Ustinov. Detection of 0.5 THz radiation from intrinsic $Bi_2Sr_2CaCu_2O_8$ Josephson junctions. *Appl. Phys. Lett.*, 88:262506, 2006.

[6] T. Beier. *Untersuchung zum magnetooptischen Kerr-Effekt (MOKE) an dünnen und ultradünnen epitaktischen Filmen*. PhD thesis, Universität zu Köln, 1989.

[7] Bergmann and Schaefer. *Lehrbuch der Experimentalphysik*, volume 3. de Gruyter, 1993.

[8] P. A. A. Booi and S. P. Benz. High power generation with distributed Josephson-junction arrays. *Appl. Phys. Lett.*, 68:3799, 1996.

[9] P. Bruno, Y. Suzuki, and C. Chappert. Magneto-optical Kerr effect in a paramagnetic overlayer on a ferromagnetic substrate: A spin-polarized quantum size effect. *Phys. Rev. B*, 53(14):9214–9220, 1996.

[10] M. Büttiger and R. Landauer. Transport and Fluctuations in Linear Arrays of Multistable Systems. In T. Riste, editor, *Nonlinear Phenomena at Phase Transitions and Instabilities*, page 111. Plenum, New York/London, 1982.

[11] W. Buckel and R. Kleiner. *Supraleitung.* Wiley-VCH, 2004.

[12] H. Busch. Über die Erwärmung von Drähten in verdünnten Gasen durch den elektrischen Strom. *Annalen der Physik*, 64:401, 1921.

[13] J.J. Chang. Calculation of the effects of a focused laser beam on the dynamic Josephson tunneling state. *Appl. Phys. Lett.*, 47:431, 1985.

[14] T. Clauss, T. Uchida, M. Mößle, D. Koelle, and R. Kleiner. Imaging of μm wavelength collective cavity resonances in $Bi_2Sr_2CaCu_2O_{8+x}$ intrinsic Josephson junction stacks under microwave irradiation. *Appl. Phys. Lett.*, 85:3166, 2004.

[15] W.W. Clegg, N.A.E. Heyes, E.W. Hill, and C.D. Wright. A highly versatile scanning laser microscope for magneto-optical observation fo micromagnetic structure. *Journal of Magnetism and Magnetic Materials*, 83:535, 1990.

[16] W.W. Clegg, N.A.E. Heyes, E.W. Hill, and C.D. Wright. Development of a scanning laser microscope for magneto-optic studies of thin magnetic films. *J. magn. magn. mat.*, 95:49, 1991.

[17] John R. Clem and R. P. Huebener. Application of low-temperature scanning electron microscopy to superconductors. *J. Appl. Phys*, 51:2764, 1980.

[18] M. F. Crommie and A. Zettl. Thermal-conductivity anisotropy of single-crystal $Bi_2Sr_2CaCu_2O_8$. *Phys. Rev. B*, 43(1):408–412, 1991.

[19] A. J. Dahm, A. Denenstein, D. N. Langenberg, W. H. Parker, D. Rogovin, and D. J. Scalapino. Linewidth of the radiation emitted by a josephson junction. *Phys. Rev. Lett.*, 22(26):1416–1420, 1969.

[20] D. Doenitz, R. Kleiner, D. Koelle, T. Scherer, and K. F. Schuster. Imaging of thermal domains in ultrathin NbN films for hot electron bolometers. *Appl. Phys. Lett.*, 90:252512, 2007.

[21] S. Egelkamp and L. Reimer. Imaging of magnetic domains by the Kerr effect using a scanning optical microscope. *Meas. Sci. Technol.*, 1:73, 1990.

[22] R. Eichele, L. Freytag, H. Seifert, R. P. Huebener, and John R. Clem. Two-dimensional imaging of hotspots in superconducting bridges by low-temperature scanning electron microscopy. *J. Low Temp. Phys.*, 52:449, 1983.

[23] R. Eichele, H. Seifert, and R. P. Huebener. Formation of hot spots in a superconductor observed by low-temperature scanning electron microscopy. *Appl. Phys. Lett.*, 38:383, 1981.

[24] H. Eisele, M. Naftaly, and J. R. Fletcher. A simple interferometer for the characterization of sources at terahertz frequencies. *Meas. Sci. Technol.*, 18:2623, 2007.

[25] S. N. Erné, A. Ferrigno, and R. D. Parmentier. Fluxon propagation and Fiske steps in long Josephson tunnel junctions. *Phys. Rev. B*, 27(9):5440, 1983.

[26] J. C. Fenton, P. J. Thomas, G. Yang, and C. E. Gough. System for fast time-resolved measurements of c-axis quasiparticle conductivity in intrinsic Josephson junctions of $Bi_2Sr_2CaCu_2O_8$. *Appl. Phys. Lett.*, 80:2535, 2002.

[27] M. C. Fischer. Aufbau und Erprobung eines Laser-Raster-Mikroskops. Master's thesis, Universität Tübingen, 1999.

[28] M. J. Freiser. A Survey of Magnetooptic Effects. *IEEE Trans. Magn.*, 4:151, 1968.

[29] J. Fritzsche, V. V. Moshchalkov, H. Eitel, D. Koelle, R. Kleiner, and R. Szymczak. Local Observation of Reverse-Domain Superconductivity in a Superconductor-Ferromagnet Hybrid. *Phys. Rev. Lett.*, 96:247003, 2006.

[30] T.A. Fulton and R.C. Dynes. Single Vortexpropagation in Josephson Tunnel Junctions . *Sol. State Comm.*, 12:57, 1973.

[31] P. E. Goa, H. Hauglin, Å. A. F. Olsen, M. Baziljevich, and T. H. Johansen. Magneto-optical imaging setup for single vortex observation. *Rev. Sci. Instrum.*, 74:141, 2003.

[32] D. Golubchik, E. Polturak, G. Koren, and S. G. Lipson. A high resolution magneto-optical system for imaging of individual magnetic flux quanta. *Optics Express*, 17:16160, 2009.

[33] P.R. Griffiths. *Chemical infrared Fourier transform spectroscopy.* Wiley-New York, 1975.

[34] M. Grünzweig. Orstaufgelöste Untersuchung der Stromverteilung in intrinsischen Josephson-Kontakten in BSCCO mittels Tieftemperatur-Raster-Laser-Mikroskopie. Master's thesis, Eberhard-Karls-Universität Tübingen, 2009.

[35] R. Gross and D. Koelle. Low temperature scanning electron microscopy of superconducting thin films and Josephson junctions. *Rep. Prog. Phys.*, 57:651, 1994.

[36] S. Guénon, M. Grünzweig, B. Gross, J. Yuan, Z. G. Jiang, Y. Y. Zhong, M. Y. Li, A. Iishi, P. H. Wu, T. Hatano, R. G. Mints, E. Goldobin, D. Koelle, H. B. Wang, and R. Kleiner. Interaction of hot spots and terahertz waves in $Bi_2Sr_2CaCu_2O_8$ intrinsic Josephson junction stacks of various geometry. *Phys. Rev. B*, 82(21):214506, 2010.

[37] S. Guénon. Ortsaufgelöste Untersuchung des Stromtransports in einer Dünnfilm-Brückenstruktur aus $Ga_{0.96}Mn_{0.04}As$ mit dem Tieftemperatur-Raster-Laser- Mikroskop. Master's thesis, Universität Tübingen, 2007.

[38] A. Vl. Gurevich and R. G. Mints. Self-heating in normal metals and superconductors. *Rev. Mod. Phys.*, 59(4):941–999, 1987.

[39] S. Heim. *Fluxonen und Quasiteilchen in mikroskopischen intrinsischen Josephson-Kontakten auf $Bi_2Sr_2CaCu_2O_{8+\delta}$-Einkristallen.* PhD thesis, Universität Tübingen, 2002.

[40] N.A.E. Heyes, C.D. Wright, and W.W. Clegg. Observation of magneto-optic phase contrast using a scanning laser microscope. *J. Appl. Phys.*, 89:5322, 1991.

[41] A. Honda and K. Shirae. Domain pattern measurements using CCD. *IEEE Trans. Magn.*, 17:3096, 1981.

[42] Xiao Hu and Shizeng Lin. Cavity phenomena in mesas of cuprate high-T_c superconductors under voltage bias. *Phys. Rev. B*, 80(6):064516, 2009.

[43] A. Hubert and R. Schaefer. *Magnetic Domains*. Springer, 1998.

[44] J.D. Jackson. *Classical Electrodynamics*. John Wiley & Sons, 1975.

[45] K. Kadowaki, M. Tsujimoto, K. Yamaki, T. Yamamoto, T. Kashiwagi, H. Minami, M. Tachiki, and R. A. Klemm. Evidence for a Dual-Source Mechanism of THz Radiation from Rectangular Mesas of Single Crystalline Bi2Sr2CaCu2O8 Intrinsic Josephson Junctions. *cond-mat.*, arXiv:0912.3063, 2009.

[46] P. Kasiraj, R. M. Shelby, J. S. Best, and D.E. Horne. Magnetic Domain Imaging with a Scanning Kerr effect Microscope. *IEEE Trans. Mang.*, 22:837, 1986.

[47] M. Keck, T. Doderer, R. Mueller, R. Pfeifer, A. Laub, R. P. Huebener, T. Traeuble, R. Dolata, T. Weinmann, and J. Niemeyer. Detailed investigation of two-dimensional Josephson junction array circuits. *IEEE Trans. Appl. Supercond.*, 7:3407, 1997.

[48] S. Kiryu, W. Zhang, S. Han, S. Deus, and J. E. Lukens. Off-chip detection of radiation from a linear array oscillator with a spiral antenna. *IEEE Trans. Appl. Supercond.*, 7:3107, 1997.

[49] R. Kleiner. Two-dimensional resonant modes in stacked Josephson junctions. *Phys. Rev. B*, 50:6919, 1994.

[50] R. Kleiner, T. Gaber, and G. Hechtfischer. Stacked long Josephson junctions in zero magnetic field: A numerical study of coupled one-dimensional sine-Gordon equations. *Phys. Rev. B*, 62(6):4086, 2000.

[51] R. Kleiner and P. Müller. Intrinsic Josephson effects in high-T_c-superconductors. *Phys. Rev. B*, 49:1327, 1994.

[52] R. Kleiner, P. Müller, H. Kohlstedt, N. F. Pedersen, and S. Sakai. Dynamic behavior of Josephson-coupled layered structures. *Phys. Rev. B*, 50(6):3942–3952, 1994.

[53] R. Kleiner, F. Steinmeyer, G. Kunkel, and P. Müller. Intrinsic Josephson effects in $Bi_2Sr_2CaCu_2O_8$ single crystals. *Phys. Rev. Lett.*, 68(15):2394–2397, 1992.

[54] A. E. Koshelev. Alternating dynamic state self-generated by internal resonance in stacks of intrinsic Josephson junctions. *Phys. Rev. B*, 78(17):174509, 2008.

[55] S. G. Lachenmann, T. Doderer, R. P. Huebener, D. Quenter, J. Niemeyer, and R. Pöpel. Spatially resolved study of the dynamics of josephson tunnel junctions. *Phys. Rev. B*, 48(5):3295, 1993.

[56] L.D. Landau and E.M. Lifshitz. Course of Theoretical Physics. In *Electrodynamics of Continuous Media*. Pergamon Press, 8.

[57] Yu. I. Latyshev, V. N. Pavlenko, S.-J. Kim, T. Yamashita, L. N. Bulaevskii, M. J. Graf amd A. V. Balatsky, N. Morozov, and M. P. Maley. Interlayer Tunneling of Quasiparticles and Cooper Pairs in Bi-2212 Single Crystal Whiskers. *Physica C*, 341-328:1499–1502, 2000.

[58] K.K. Likharev. *Dynamics of Josephson Junctions and Circuits*. Gordon and Breach Science Publisher, 1986.

[59] Shizeng Lin and Xiao Hu. Possible Dynamic States in Inductively Coupled Intrinsic Josephson Junctions of Layered High-T_c Superconductors. *Phys. Rev. Lett.*, 100(24):247006, 2008.

[60] H. Lueder and E. Spenke. Über den Einfluß der Wärmeableitung auf das elektrische Verhalten von temperaturabhängigen Widerständen. *Physikalische Zeitschrift*, 36:767, 1936.

[61] B. Mayer, T. Doderer, R.P. Huebener, and A.V. Ustinov. Imaging of one- and two-dimensional Fiske modes in Josephson tunnel junctions. *Phys. Rev. B*, 44:12463, 1991.

[62] J. McCord and A. Hubert. Domain Analysis in Epitaxial Iron-Aluminum and Iron-Gold Sandwiches with Oscillatory Exchange. *IEEE Trans. Magn. Mat.*, 29:2735, 1993.

[63] D. E. McCumber. Effect of ac Impedance on dc Voltage-Current Characteristics of Superconductor Weak-Link Junctions. *J. Appl. Phys*, 39:3113, 1968.

[64] P.K. Mühlschlegel. Ortsaufgelöste Thermospannungsmessung an YBaCuO-Dünnfilmen mit dem Laser-Rastermikroskop. Master's thesis, Universität Tübingen, 2001.

[65] T. Nachtrab. *c-Achsen-Transporteigenschaften des intrinsischen Supraleiter-Ferromagnet-Hybrids* $RuSr_2GdCu_2O_8$. PhD thesis, Universität Tübingen, 2004.

[66] M. Naftaly, P. Dean, R.E. Miles, J.R. Fletcher, and A. Malcoci. A Simple Interferometer for the Analysis of Terahertz Sources and Detectors. *IEEE J. Sel. Top. Quant. Electron.*, 14:443, 2008.

[67] M. J. Naughton, R. C. Yu, P. K. Davies, J. E. Fischer, R. V. Chamberlin, Z. Z. Wang, T. W. Jing, N. P. Ong, and P. M. Chaikin. Orientational anisotropy of the upper critical field in single-crystal $YBa_2Cu_3O_7$ and $Bi_{2.2}CaSr_{1.9}Cu_2O_{8+x}$. *Phys. Rev. B*, 38(13):9280–9283, 88.

[68] P. M. Oppeneer, T. Maurer, J. Sticht, and J. Kübler. Ab initio calculated magneto-optical Kerr effect of ferromagnetic metals: Fe and Ni. *Phys. Rev. B*, 45(19):10924–10933, 1992.

[69] L. Ozyuzer, A. E. Koshelev, C. Kurter, N. Gopalsami, Q. Li, M. Tachiki, K. Kadowaki, T. Yamamoto, H. Minami, H. Yamaguchi, T. Tachiki, K. E. Gray, W.-K. Kwok, and U. Welp. Emission of Coherent THz Radiation from Superconductors. *Science*, 318:1291, 2007.

[70] L Ozyuzer, Y Simsek, H Koseoglu, F Turkoglu, C Kurter, U Welp, A E Koshelev, K E Gray, W K Kwok, T Yamamoto, K Kadowaki, Y Koval, H B Wang, and P Müller. Terahertz wave emission from intrinsic josephson junctions in high- t c superconductors. *Superconductor Science and Technology*, 22(11):114009, 2009.

[71] S.S.P. Parkin, C. Kaiser, A. Panchula, P.M. Rice, B. Hughes, M. Samant, and S.H. Yang. Giant tunneling magnetoresistance at room temperature with MgO (100) tunnel barriers. *Nature Materials*, 3:862–867, 2004.

[72] R.D. Parmentier. Solitons and long Josephson junctions. In H. Weinstock and R.W. Raltson, editors, *The New Superconductin Electronics*. Kluwer Academic Publisher, 1993.

[73] N. F. Pedersen and A. V. Ustinov. Fluxons in Josephson transmission lines: new developments. *Supercond. Sci. Technol.*, 8:389, 1995.

[74] F. Pedrotti, L. Pedrotti, W. Bausch, and H.Schmidt. *Optik:Eine Einführung*. Prentice Hall, 1996.

[75] M. Peschka. *Entwicklung und Aufbau eines Tieftemperatur-Laser-Rastermikroskops für starke Magnetfelder*. PhD thesis, Universität Tübingen, 1999.

[76] A. Petraglia. *Fluxons in Coupled Josephson systems*. PhD thesis, Technical University of Denmark, 1996.

[77] G.I. Ping, C. W. See, and M.G. Somekh. A confocal fibre scanning microscope for magnetic domaing imaging. *Journal of Microscopy*, 184:149, 1996.

[78] G.L. Ping, C.W. See, M.G. Somekh, M. B. Suddendorf, J.H. Vincent, and P.K. Footner. A Fast-Scanning Optical Microscope for Imaging Magnetic Domain Structures. *Scanning*, 18:8, 1995.

[79] S. Sakai, P. Bodin, and N.F. Pedersen. Fluxons in thin-film superconductor-insulator superlattices. *J. Appl. Phys.*, 73:2411, 1993.

[80] J. J. Sakurai. *Modern Quatum Mechanics*. 1994.

[81] K. Sato. Measurement of Magneto-Optical Kerr Effect Using Piezo-Birefringent Modulator. *Japanese Journal of Applied Physics*, 20:2403, 1981.

[82] R. Schäfer and A. Hubert. A new magnetooptic effect related to non-uniform magnetization on the surface of a ferromagnet. *phys. stat. sol. (a)*, 118:271, 1990.

[83] F. Schmidt, W. Rave, and A. Hubert. Enhancement of magneto-optical domain observation by digital image processing. *IEEE Trans. Magn.*, 21:1596, 1985.

[84] T. Schwarz. Tieftemperatur-Laserrastermikroskopie in starken Magnetfeldern. Master's thesis, Universität Tübingen, 2002.

[85] A.C. Scott. Distributed device applications of the superconducting tunnel junction. *Solid-State Electronics*, 7:137, 1964.

[86] K. Shirae and K. Sugiyama. A CCD image sensor and a microcomputer make magnetic domain observation clear and convenient. *J. Appl. Phys*, 53:8380, 1982.

[87] W. J. Skocpol, M. R. Beasley, and M. Tinkham. Self-Heating Hotspots in Superconducting Thin-Film Microbridges. *J. Appl. Phys.*, 45:4054–4066, 1974.

[88] E. Spenke. Eine anschauliche Deutung der Abzweigtemperatur scheibenförmiger Heißleiter. *Electrical Engineering (Archiv für Elektrotechnik)*, 30(11):728–736, 1936.

[89] E. Spenke. Zur technischen Beherrschung des Wärmedurchschlages von Heißleitern. *Wissenschaftliche Veröffentlichungen aus den Siemens-Werken*, 15(1):92, 1936.

[90] J.L. Stewart. The Power Spectrum of a Carrier Frequency Modulated by Gaussian Noise. *Proceedings of the IRE*, 42:1539, 1954.

[91] W.C. Stewart. Current-Voltage Characteristics of Josephson Junctions . *Appl. Phys. Lett.*, 12:277, 1968.

[92] R.L. Stratonovich. *Topics in the Theory of Random Noise*, volume 1. Gordon and Breach, New York-London, 1967.

[93] J. Strong and G.A. Vanasse. Lamellar Grating Far-Infrared Interferometer. *J. Opt. Soc. Am.*, 50(2):113, 1960.

[94] D. L. Stuehm and C. W. Wilmsen. Diffraction patterns and vortex structure of asymmetrical and cross Josephson junction. *J. Appl. Phys.*, 45:429, 1974.

[95] J. C. Swihart. Field Solution for a Thin-Film Superconducting Strip Transmission Line. *J. Appl. Phys.*, 32:461, 1961.

[96] K. Takanaka. Zero field steps in Josephson junctions. *Solid State Communications*, 29(5):443 – 445, 1979.

[97] J. L. Tallon. Normal-state pseudogap in $Bi_2Sr_2CaCu_2O_8$ characterized by impurity scattering. *Phys. Rev. B*, 58(10):R5956–R5959, 1998.

[98] J. M. Tarascon, Y. Le Page, P. Barboux, B. G. Bagley, L. H. Greene, W. R. McKinnon, G. W. Hull, M. Giroud, and D. M. Hwang. Crystal substructure and physical properties of the superconducting phase $Bi_4(Sr,Ca)_6Cu_4O_{16+x}$. *Phys. Rev. B*, 37(16):9382–9389, 1988.

[99] M. Tonouchi. Cutting-edge terahertz technology. *Nature Photon.*, 1:97, 2007.

[100] T. Uhl. Magnetooptischer Kerr-Effekt: Aufbau eines Praktikumsversuches. Master's thesis, Eberhard-Karls-Universität Tübingen, 2007.

[101] A.F. Volkov and M.Kogan. Physical Phenomena in Semiconductors with Negative Differential Conductivity. *Sov. Phys. Usp.*, 11:881, 1969.

[102] R. Vollmer. Lineare und nichtlineare Magnetooptik an ultradünnen ferromagnetischen Schichten und Vielfachschichten. In *Vorlesungsmanuskripte des 30. IFF-Ferienkurses: Magnetische Schichtsysteme in Forschung und Anwendung*. Institut für Festkörperforschung des Forschungszentrums Jülich GmbH, 1999.

[103] M. Wagenknecht. Abbildung magnetischer Domänen im Laser-Raster-Mikroskop. Master's thesis, Universität Tübingen, 2004.

[104] O. Waldmann, F. Steinmeyer, P. Müller, J. J. Neumeier, F. X. Régi, H. Savary, and J. Schneck. Temperature and doping dependence of the penetration depth in $Bi_2Sr_2CaCu_2O_{8+\delta}$. *Phys. Rev. B*, 53(17):11825–11830, 1996.

[105] H. B. Wang, S. Guénon, B. Gross, J. Yuan, Z. G. Jiang, Y. Y. Zhong, M. Grünzweig, A. Iishi, P. H. Wu, T. Hatano, D. Koelle, and R. Kleiner. Coherent Terahertz Emission of Intrinsic Josephson Junction Stacks in the Hot Spot Regime. *Phys. Rev. Lett.*, 105(5):057002, 2010.

[106] H. B. Wang, S. Guénon, J. Yuan, A. Iishi, S. Arisawa, T. Hatano, T. Yamashita, D. Koelle, and R. Kleiner. Hot Spots and Waves in $Bi_2Sr_2CaCu_2O_8$ Intrinsic Josephson Junction Stacks: A Study by Low Temperature Scanning Laser Microscopy. *Phys. Rev. Lett.*, 102(1):017006, 2009.

[107] H. B. Wang, T. Hatano, T. Yamashita, P. H. Wu, and P. Müller. Direct observation of self-heating in intrinsic Josephson junction array with a nanoelectrode in the middle. *Appl. Phys. Lett.*, 86:023504, 2005.

[108] U. Welp, V. K. Vlasko-Vlasov, X. Liu, J. K. Furdyna, and T. Wojtowicz. Magnetic Domain Structure and Magnetic Anisotropy in $Ga_{1-x}Mn_xAs$. *Phys. Rev. Lett.*, 90:167206, 2003.

[109] R. Wener, M. Weiler, A.Y. Petrov, B.A. Davidson, R. Gross, R. Kleiner, S.T.B. Goennenwein, and D. Koelle. Local Tunneling Magnetoresistance probed by Low-Temperature Scanning Laser Microscopy. *(to be published).*

[110] R. Werner, A. Y. Aladyshkin, J. Fritzsche, S.Guénon, I.M. Nefedov, V.V. Moshchalkov, R. Kleiner, and D. Koelle. Domain-wall and reverse-domain superconducting states of a Pb thin-film bridge on a ferromagnetic $BaFe_{12}O_{19}$ single crystal. *arXiv:1105.6048.*

[111] T. Wilson and C. Sheppard. *Theory and Practice of Scanning Optical Microscopy.* Academic Press, 1984.

[112] J. Wrona, T. Stobiecki, R. Rak, M. Czapkiewicz, F. Stobiecki, L. Uba, Korecki, T. Slezak, J. Wilgocka-Slezak, and M. Rots. Kerr magnetometer based on a differential amplifier. *phys. stat. sol. (a)*, 196:161, 2003.

[113] W.Zinth and U. Zinth. *Optik.* Oldenbourg, 2 edition, 2009.

[114] L. X. You, P. H. Wu, J. Chen, W.W. Xu, K. Kajiki, S. Watauchi, and I. Tanaka. Suppression of the superconducting energy gap in intrinsic Josephson junctions of $Bi_2Sr_2CaCu_2O_8$ single crystals. *Supercond. Sci. Technol.*, 17:1160, 2004.

[115] A. Yurgens. Temperature distribution in large Bi2212 mesas. *arXiv:1005.2932*.

[116] A. Yurgens. Temperature distribution in a large $Bi_2Sr_2CaCu_2O_{8+\delta}$ mesa. *Phys. Rev. B*, 83(18):184501, 2011.

[117] A.K. Zvezdin and V.A. Kotov. *Modern Magnetooptics and Mangetooptical Materials*. Institute of Physics Publishing, 1997.